

MARKUS HIEKKAMÄKI

Quantum Interference in Transverse Spatial Modes of Photons

MARKUS HIEKKAMÄKI

Quantum Interference in Transverse
Spatial Modes of Photons

ACADEMIC DISSERTATION

To be presented, with the permission of
the Faculty of Engineering and Natural Sciences
of Tampere University,
for public discussion in the TB109 auditorium
of Tietotalo, Korkeakoulunkatu 1, Tampere,
on 1st of September 2023, at 12 o'clock.

ACADEMIC DISSERTATION

Tampere University, Faculty of Engineering and Natural Sciences
Finland

<i>Responsible supervisor and Custos</i>	Associate Professor Robert Fickler Tampere University Finland	
<i>Pre-examiners</i>	Professor Gabriel Molina-Terriza Materials Physics Center Spain	Assistant Professor Filippo Cardano University of Naples Federico II Italy
<i>Opponent</i>	Associate Professor Jonathan Leach Heriot-Watt University United Kingdom	

The originality of this thesis has been checked using the Turnitin OriginalityCheck service.

Copyright ©2023 author

Cover design: Roihu Inc.

ISBN 978-952-03-3012-5 (print)

ISBN 978-952-03-3013-2 (pdf)

ISSN 2489-9860 (print)

ISSN 2490-0028 (pdf)

<http://urn.fi/URN:ISBN:978-952-03-3013-2>



ClimateCalc CC-000025-FI
PunaMusta Printing

Carbon dioxide emissions from printing Tampere University dissertations have been compensated.

PunaMusta Oy – Yliopistopaino
Joensuu 2023

PREFACE

To start with, I want to thank my supervisor Robert Fickler and the Group of Experimental Quantum Optics at Tampere University. From the very inception of the group, Robert managed to create an open and welcoming environment, which allowed me to grow and learn much more than I could have fathomed. He also provided an exceptionally great example of how a supervisor can foster a positive and optimistic environment which feeds the drive and curiosity of the group members. I am also grateful for the time he had for the numerous discussions from which I learnt most of what I know about quantum optics.

Of course, I also want to acknowledge the other people who helped me with this thesis work in one way or another. This includes my valued co-authors Marco Ornigotti and Frédéric Bouchard, and some of the past and present members of the experimental quantum optics group; Lea Kopf, Shashi Prabhakar, Matias Eriksson, Stephen Plachta, and Oussama Korichi. From this group of people, I wanted to single out my friend and co-author Rafael F. Barros who was instrumental in shaping my approach to building experimental systems and understanding of many concepts of physics. I want to thank the rest of the past and present group members, in addition to the rest of the SK1 corridor for the interesting conversations and fun moments we shared. I especially enjoyed and learnt a lot from the interesting and never-ending conversations with Piotr Ryzkowski. While still talking about friends and colleagues, I want to thank my friends Timo Stolt, Tommi Mikkonen, and Jussi Isokuortti who helped me excel in my studies and made my nine years at Tampere University much more enjoyable.

I am also thankful to Joel Carpenter, and the people in his group in Brisbane, for the chance of joining them for a few months. My time in Brisbane taught me so much and gave me a whole new set of tools in my experimental toolbox.

Besides the help and support of colleagues, I would not have gotten this

far without the support of family and friends. I am extremely grateful to my parents Minna and Matti, who have been extremely supportive of me at every stage of my life, and my younger siblings Maria and Miska whose achievements and drive have inspired me to push forward in my own endeavours. My gratitude also extends to my cousins, aunts, uncles, grandparents, godparents, and great aunts whose influence has made me the person I am today. Last but not least, I want to thank my partner, Mona. I would not have gotten through this process without your love, patience, support, and great outlook on life.

Finally, I want to express my gratitude for the financial supporters of my thesis work which include the Tampere University Faculty of Engineering and Natural Sciences, Emil Aaltonen Foundation, Tamperelaisen Tutkimustyön Tukisäätiö, and the Magnus Ehrnrooth Foundation.

Tampere, April 2023

Markus Hiekkamäki

ABSTRACT

Since classical interference has become ubiquitous in our modern optical devices and experiments, it is reasonable to assume that its quantum counterparts could become as prevalent in the next wave of technologies. The first signs of this can already be seen in the plethora of potential quantum technological applications that heavily rely on non-classical multi-photon interference effects. One degree of freedom where multi-photon interference has not been extensively studied yet is the transverse-spatial degree of freedom. This lack of studies is surprising when considering the potential benefits this degree of freedom has demonstrated in many other technological applications. Hence, our work here aims to increase our understanding of quantum interference in transverse spatial modes. We do this by investigating two-photon interference effects in this degree of freedom and by exploring some of their applications in metrology.

In this thesis, we first define a theoretical framework with which one can calculate the quantum effects of structured paraxial light fields. We also describe in detail how one can use phase-only spatial light modulators to shape and measure the transverse structure of photons. This is done both for the case of a single mask transformation and so-called multi-plane light conversion schemes. The experimental work of this thesis builds upon these methods and the theoretical framework to manipulate and utilize the quantum states of paraxial photons.

In our first experiments, we observed two-photon interference in the transverse-spatial degree of freedom. Initially, this was done in a complex unitary device which performs a beamsplitter-like transformation solely in the transverse-spatial degree of freedom. Thus, this experiment performs the exact analogue of the famous Hong-Ou-Mandel experiment in the space of transverse spatial modes. The unitary device was a multi-plane light conversion system. Subsequently, we removed the unitary device and performed similar interference

effects in a simplified setup which was easier to operate. This setup allowed us to produce high-quality two-photon N00N states between transverse spatial modes, in a single beam of light.

After demonstrating our capability of producing high-quality N00N states, we explored their applicability in different quantum metrological tasks. This was done theoretically with the help of a quantity called quantum Fisher information, and experimentally using the simplified quantum interference system. We applied the N00N states to superresolution experiments in rotations and longitudinal translations.

Lastly, we were also able to investigate, using our N00N state experiments, the Gouy phase of a photon number state. As this phase has not been previously investigated in such a context, it provided us with some new insights into previously investigated phenomena. For instance, this experiment provides a simple example of why the so-called effective de Broglie wavelength of photons is not always a good description of photon number state evolution. It also allowed us to reaffirm the predictive power of a specific physical interpretation of the Gouy phase.

TIIVISTELMÄ

Valon interferenssiä esiintyy joka puolella nykyisessä tekniikassamme sekä optisissa kokeissa. Tämän takia voisi olettaa, että tämän interferenssin kvanttimekaanisesta vastineesta voisi tulla yhtä tärkeä ilmiö tulevaisuuden teknologioissa. Ensimmäiset merkit kvantti-interferenssin hyödyllisyydestä näkyvät useissa ehdotetuissa kvanttiteknologisissa ratkaisuissa, jotka hyödyntävät tällaisia interferenssejä. Vaikka valon kvantti-interferenssiä on tutkittu kattavasti, sitä ei ole juurikaan tutkittu sen poikittaisrakenteita hyödyntäen. Tämä olisi mielenkiintoinen konteksti kvantti-interferenssin tutkimiselle, strukturoitujen poikittaisrakenteiden hyödyllisten ominaisuuksien takia.

Tässä väitöskirjassa määritellään ensin teoreettinen pohja, jonka avulla paraksiaalisten valonsäteiden kvanttitiloja voidaan laskea ja mallintaa. Kirjassa käydään myös yksityiskohtaisesti läpi, kuinka vaihetta moduloivilla valon poikittaisrakenteen modulaattoreilla voi muovata ja mitata fotonien poikittaisrakenteita. Tämä sisältää metodeja, joissa käytetään vain yhtä poikittaisen vaiherakenteen modulointia sekä menetelmiä, jotka hyödyntävät montaa perättäistä vaihemodulointia. Kirjassa esiteltävissä kokeellisissa tutkimuksissa käytetään edellä mainittua teoriaa ja kokeellisia menetelmiä paraksiaalisen valon kvanttitilojen manipuloimiseen. Kvanttitiloja hyödynnetään tämän jälkeen eri applicaatioissa.

Kirjan ensimmäisessä kokeellisessa osiossa mitattiin kahden fotonin interferenssi valon poikittaisrakenteissa. Tämä tehtiin ensin laitteella, jolla voidaan rakentaa mielivaltaisia unitaarisia transformaatioita. Laitteella implementoitiin transformatio poikittaisrakenteissa, joka vastaa säteenjakajan tekemää transformatiota. Täten koe vastaa täysin kuuluisaa Hong-Ou-Mandel interferenssikoetta paitsi, että tällä kertaa interferenssi tapahtuu valon poikittaisrakenteissa eikä valon säteen kulkusuunnissa. Koe toistettiin seuraavaksi yksinkertaistetussa koejärjestelyssä. Tässä kokeessa näytettiin, että samanlainen in-

terferenssi saadaan aikaiseksi poistamalla unitaaritransformaatiolaite. Tällä helpommalla koejärjestelyllä kyettiin tuottamaan laadukkaita kahden fotonin $N00N$ tiloja yksittäisessä valonsäteessä.

Kirjan toisessa kokeessa hyödynnettiin näitä valon $N00N$ tiloja erinäisissä metrologisissa applikaatioissa. Ennen mittauksia, valon hyödyllisimmät kvanttilat identifioidiin Fisher-informaation avulla. $N00N$ tiloja käytettiin tämän jälkeen kvantti-ilmiöitä hyödyntävissä pyörähdyksen ja pitkittäissiirtymän mittaauksissa.

Kirjan viimeisessä osiossa mitattiin monen fotonin tilan Gouy-vaihetta näillä samoilla $N00N$ tiloilla. Koska valon Gouy-vaihetta ei ole ennen mitattu tällaisessa kontekstissa, mittaustulokset tuovat uutta näkökulmaa fotonien käyttäytymiseen. Nämä mittaukset esimerkiksi paljastivat, että aiemmissä tutkimuksissa hyödynnetty monen fotonin de Broglie aallonpituus ei kuvaa täysin monen fotonin tilojen ominaisuuksia. Tämän lisäksi tuloksista huomattiin, kuinka eräs tulkinta klassisen Gouy-vaiheen alkuperästä pystyy myös ennustamaan monen fotonin Gouy-vaiheen käyttäytymisen.

CONTENTS

1	Introduction	1
1.1	Aim of this work	4
1.2	Outline	4
2	Classical and Quantum Theory of Structured Light	7
2.1	Classical Linear Optics.	7
2.1.1	Paraxial Wave Equation.	7
2.1.2	Laguerre-Gaussian Modes	10
2.1.3	Angular Spectrum Representation	14
2.2	Quantized Light	16
2.2.1	Multimode Field Quantization	16
2.2.1.1	Fock States	20
2.2.1.2	Coherent States	23
2.2.2	Quantized Paraxial Beams	25
2.3	Measurements, Unitary Evolution, and Mutually Unbiased Bases	32
2.3.1	Measurements	32
2.3.2	Mutually Unbiased Bases	33
2.3.3	Unitary Evolution	35
2.3.4	N00N States	37
2.4	Nonlinear Optics	39
2.4.1	Classical Three-Wave Mixing	39
2.4.2	Quantum Description of Spontaneous Parametric Down- conversion.	42
3	Creation and Transverse spatial Manipulation of Photons	45
3.1	Photon Pair Source.	45
3.2	Photon Pair Detection	48

3.3	Liquid Crystal Spatial Light Modulators.	50
3.4	Single Mask Spatial Mode Manipulation.	55
3.4.1	Spatial Structuring.	55
3.4.2	Single Mask Measurements of Spatial Structure . . .	59
3.5	Multi-Plane Light Conversion	60
3.5.1	Wavefront Matching	62
3.5.2	Constraints and Parameters in Wavefront Matching .	66
4	Photon Bunching in Spatial Modes.	69
4.1	Two-Photon Interference.	69
4.2	Two-Photon Interference in Spatial Mode Unitaries.	75
4.3	Creating N00N States Through Two-Photon Interference . . .	81
5	Metrology with Transverse-Spatial N00N States	85
5.1	Fisher Information and Quantum Limits of Estimation.	85
5.1.1	Fisher Information	86
5.1.2	Quantum Fisher Information	87
5.1.3	Standard Quantum Limit and Heisenberg Limit . . .	88
5.2	Angular Superresolution with Orbital Angular Momentum N00N States.	89
5.3	Longitudinal Superresolution with Radial Mode N00N States .	93
6	Photon Number States and the Gouy Phase.	99
6.1	Propagation of N-photon Fock states.	99
6.2	Implications of the N-photon Gouy phase	101
7	Conclusion and Outlook	103
7.1	Outlook	105
	References	107
	Publication I.	131
	Publication II	141
	Publication III.	149

SYMBOLS AND ABBREVIATIONS

ASR	angular spectrum representation
BPF	band-pass filter
BS	beamsplitter
c.c.	complex conjugate
CC	coincidence counter
CRB	Cramér-Rao bound
e.g.	for example, from Latin <i>exempli gratia</i>
et al.	and others, from Latin <i>et alii</i>
FFT	fast Fourier transform
FI	Fisher information
H.c.	Hermitian conjugate
HG	Hermite-Gaussian
HL	Heisenberg limit
HOM	Hong-Ou-Mandel
HWP	half-wave plate
i.e.	that is, from Latin <i>id est</i>
LC	liquid crystal
LG	Laguerre-Gaussian
MPLC	multi-plane light conversion or multi-plane light converter
MUB	mutually unbiased basis
OAM	orbital angular momentum

POVM	positive operator-valued measure
ppKTP	periodically poled potassium titanyl phosphate
PWE	paraxial wave equation
QCRB	quantum Cramér-Rao bound
QFI	quantum Fisher information
QKD	quantum key distribution
QPM	quasi-phase-matching
QWP	quarter-wave plate
SAM	spin angular momentum
SLM	spatial light modulator
SMF	single mode fibre
SPAD	single-photon avalanche diode
SPDC	spontaneous parametric downconversion
SQL	standard quantum limit
WFM	wavefront matching
ZPE	zero point energy

A	magnetic vector potential
$\tilde{\mathbf{A}}$	temporally oscillating magnetic vector potential
\hat{A}	magnetic vector potential operator
\hat{a} and \hat{b}	annihilation operator
\hat{a}^\dagger and \hat{b}^\dagger	creation operator
α	coherent state eigenvalue
B	magnetic induction vector
$\tilde{\mathbf{B}}$	temporally oscillating magnetic induction vector
$\hat{\mathbf{B}}$	magnetic induction vector operator

c	speed of light
$\chi^{(i)}$	i^{th} order susceptibility
\hat{D}	displacement operator
d	dimension
δ_{ij}	Kronecker delta
$\delta^{(d)}(\boldsymbol{\xi} - \boldsymbol{\xi}')$	Dirac delta in d dimensions
\mathcal{E}	complex amplitude of electric field in momentum space
E	energy
\mathbf{E}	electric field vector
$\tilde{\mathbf{E}}$	temporally oscillating electric field vector
$\hat{\mathbf{E}}$	electric field vector operator
\mathbf{e}	polarization unit vector
ϵ_0	electric permittivity of free space
H	Hamiltonian
\hat{H}	Hamiltonian operator
\hbar	reduced Planck constant
\hat{I}	identity operator
i	imaginary unit
\mathbf{J}	total angular momentum vector
k_c	central wavenumber
k_x	spatial frequency in direction of Cartesian coordinate x
k_y	spatial frequency in direction of Cartesian coordinate y
k_z	wave vector component along the optical axis
k	wavenumber
\mathbf{k}_\perp	transverse wavevector
L	length
$L_p^{ \ell }(\xi)$	generalized Laguerre polynomial

\hat{L}_z	operator for the z-component of orbital angular momentum
\mathbf{L}	orbital angular momentum vector
ℓ	orbital angular momentum index of Laguerre-Gaussian modes
Λ	crystal poling period
λ	wavelength
M	mode order
μ_0	magnetic permeability of free space
N	photon number
\hat{n}	number operator
ω	angular frequency
\mathbf{P}	material polarization
$\tilde{\mathbf{P}}$	temporally oscillating material polarization
\hat{P}_z	operator for momentum in z direction
p	canonical momentum or radial index of Laguerre-Gaussian beams
\hat{p}	canonical momentum operator
Φ_G	Gouy phase
φ	azimuthal angle in the plane perpendicular to the optical axis
q	canonical position
\hat{q}	canonical position operator
R	rate of events
R_c	radius of curvature
\mathbf{r}	position vector
\mathbf{r}_\perp	two-dimensional position vector, perpendicular to the optical axis

ρ	axial distance from the optical axis
\mathbf{S}	spin angular momentum vector
\hat{S}_z	operator for the z-component of spin angular momentum
σ	index describing the direction of circular polarization
$\hat{\sigma}_i$	Pauli operator
t	time
τ	temporal delay
θ	phase
U	unitary matrix
\mathcal{U}	Fourier transform of normalized scalar field
\hat{U}	unitary operator
$\hat{\mathcal{U}}$	unitary operator in Fock space notation
u	normalized scalar field
V	volume
v	visibility
\mathcal{W}	entanglement witness value
w	beam radius
w_0	beam radius at beam waist
\hat{X}_i	dimensionless quadrature operator
x	Cartesian coordinate orthogonal to z and y
y	Cartesian coordinate orthogonal to z and x
z	Cartesian coordinate in the direction of the optical axis
z_R	Rayleigh range

ORIGINAL PUBLICATIONS

- Publication I Markus Hiekkamäki and Robert Fickler. “High-Dimensional Two-Photon Interference Effects in Spatial Modes”. In: *Physical Review Letters* 126 (2021), p. 123601.
- Publication II Markus Hiekkamäki, Frédéric Bouchard, and Robert Fickler. “Photonic Angular Superresolution Using Twisted N00N States”. In: *Physical Review Letters* 127 (2021), p. 263601.
- Publication III Markus Hiekkamäki, Rafael F. Barros, Marco Ornigotti, and Robert Fickler. “Observation of the quantum Gouy phase”. In: *Nature Photonics* 16 (2022), pp. 828–833.

Author's contribution

- Publication I The author jointly designed the experiment with R. Fickler, built the experimental system, collected and processed all of the experimental data, and wrote the first draft of the manuscript. The final manuscript was written together with R. Fickler.
- Publication II The author jointly designed the experiment with R. Fickler, built the experimental system, collected and processed all of the experimental data, derived the theoretical framework, and wrote the first draft of the manuscript. The final manuscript was written together with all the coauthors.
- Publication III The author jointly designed the experiment with R. Fickler, built the experimental system, collected and processed all of the experimental data, derived the theoretical framework together with R.F. Barros and M. Ornigotti, and wrote the first draft of the manuscript. The final manuscript was written together with all the coauthors.

1 INTRODUCTION

Ever since the first experiments demonstrating the wave nature of light in the early 1800s, interference of light has been a very important tool for uncovering different fundamental properties of light, and in building modern sensors and other devices. One of the first interference experiments was the famous Young's double slit experiment [1], which contributed to the acceptance of the wave theory of light. After Young's experiment, interference of light started to become a much more common tool in studying the nature of light, until it eventually reached its ubiquitous status.

A few decades after the wave properties of light had become commonly accepted, Maxwell showed that light could be described as an electromagnetic wave [2] and formulated the extremely powerful set of equations describing electromagnetic fields. While these equations have proven their worth and are being used to describe the behaviour of light in most of our modern devices, Albert Einstein's description of the photoelectric effect at the beginning of the 1900s brought doubt to whether they provided the complete picture [3]. After this revelation, the modern quantum mechanical description of light started to take form with the combined effort of many physicists. These new descriptions gave us photons or light quanta, but their implications for interference were not fully understood initially, as is evident from Dirac's famous statement: "*Each photon then interferes only with itself. Interference between two different photons never occurs.*" [4]. The experimental and theoretical efforts conducted from the 1960s through the 1980s forced researchers to re-evaluate Dirac's maxim [5]. During this time, the progress in light-based technologies and the quantum mechanical theory of light led to theoretical and experimental investigations into the interference of two photons. These investigations were performed both with independent lasers [6–9] and quantum states of light [10–13]. Other types of quantum interference that were also studied around

the same time were true single photons interfering with themselves [14] and, depending on one's definition of interference, the concurrent research on entanglement [15–18]. Eventually, all this quantum interference research led to arguably one of the most famous quantum interference experiments which was performed in 1987 by Hong, Ou, and Mandel [19]. In this experiment, the authors showed that, under certain conditions, when two photons arrive at a beamsplitter, they bunch to the same mode and always exit the beamsplitter together. Similar experiments were then published by other researchers soon afterwards [20, 21] and the effect has since become very important for subsequent research and technological innovation [22]. For a more detailed description of the history of research into quantum interference, see references [5, 22].

Even from this brief and incomplete description of the events leading up to the so-called the Hong-Ou-Mandel (HOM) experiment, we can see the incredible amount of work and novel concepts it has taken for us to be able to accurately describe and engineer complex multi-photon quantum effects. As classical interference of light is already an important part of the technology of our current world (e.g. in gravitational wave detection [23]), the work put into studies of the quantum interference of light could enable a new wave of light-based technologies. This could be, for example, in linear optical quantum computing [22, 24] or quantum repeaters for optical quantum communication [22, 25], where quantum interference is an important effect enabling these technologies.

Since quantum interference is a general interference phenomenon for light, it can occur in any of its degrees of freedom. This includes the photon paths where Hong, Ou, and Mandel started, but also polarization [26], spectrum [27], waveguide modes [28], and free-space transverse-spatial modes (Ch. 4). In this thesis, we will be looking into the last one of the listed degrees of freedom, focusing on so-called paraxial beams of light. Besides the experiments presented in this thesis, and the aforementioned waveguide modes, it should be noted that quantum interference in transverse field structures has also been explored in a few other contexts in earlier experiments, such as with q-plates [29] and in multi-mode fibres [30]. It has also become an important effect in recent proof-of-principle experiments [31, 32].

Out of the range of possible structures paraxial light fields can have, beams

with a helically twisted wavefront have been of special interest due to the orbital angular momentum (OAM) they carry [33, 34]. This OAM has a plethora of applications ranging from optical tweezers [35–40] to quantum simulations [41] and encoding quantum information [42, 43]. In addition to these applications, light beams with OAM, and structured light in general, seem to be especially suited for different imaging and sensing applications. This is evident from the different proof-of-principle experiments using generation and measurement techniques of transversely structured light, e.g., for distinguishing two incoherent point sources [44–47], sensing beam rotations [48–51], or sensing lateral displacements [52–54].

As alluded to before, besides these sensing applications, experiments investigating the suitability of such transverse spatial modes for quantum information tasks have also become more frequent. These experiments usually investigate their usefulness for encoding quantum information in communications [55–62] or information processing applications [63–69]. Photons encoded with such high-dimensional quantum information are often called qudits and they have been shown to have the potential to surpass qubit implementations. This potential stems from their increased data capacity [43, 70], their increased security in communications applications [71, 72], resilience to noise [73], and their potential in simplifying quantum algorithms [70, 74, 75]. While the set of transverse spatial modes is the high-dimensional set of discrete modes we are investigating here, other sets and degrees of freedom have also been used to encode high-dimensional information onto photons. These sets include time-bins [73], frequency-bins [76], temporal modes [77], macro-pixels [78, 79], and photon paths [80]. In addition to such discrete bases, the same degrees of freedom can be used for encoding so-called continuous-variable quantum information [81].

In general, the research fields of structured light and photonic quantum information are currently very active fields of research, which is evident from the amount of published research. This same trend is also seen in the number of related review and roadmap articles published since 2019 [82–88].

1.1 Aim of this work

Because of the increasing interest in new quantum technologies, the prominence of transverse-spatial modes, potential applications in sensing, and the central role of interference in the physics of light, a few interesting questions arise. How could the aforementioned technologies benefit from transverse spatial modes? And could quantum interference in the transverse-spatial degree of freedom be used to investigate fundamental aspects of photons? Furthermore, since quantum interference has such a central role in many of the photonic quantum technological applications, it would be interesting to know if we can achieve arbitrary control of multi-photon quantum interference solely in the transverse-spatial degree of freedom. Hence, the aim of this thesis is to investigate if it is possible to build, with current technologies, arbitrary spatial mode transformations where it is possible to control the quantum interference of multiple photons. Furthermore, we will investigate if this quantum interference could be immediately harnessed in creating quantum states for exploring the fundamental nature of photons, or in developing novel quantum technologies benefiting from the transverse-spatial degree of freedom.

1.2 Outline

The thesis is structured as follows. In chapter 2 we describe the theoretical background of the key concepts relevant to the experimental studies performed in this thesis work. We will start from the classical optics description of paraxial light beams in section 2.1, move to the quantum description of such beams in section 2.2, after which we will briefly go over some relevant concepts of nonlinear optics in section 2.4. After exploring the relevant theoretical background, in chapter 3 we will get a better understanding of the methods and devices needed to create, manipulate, and measure quantum states of light in the transverse-spatial degree of freedom. This includes a description of our photon pair source (section 3.1), details on structuring photons with a spatial light modulator (sections 3.3 and 3.4), and a description of a relatively new category of light shaping devices called multi-plane light converters (MPLC) in section 3.5. In section 3.5 we will also explore how we can use these devices

to build the arbitrary spatial mode unitaries we wanted to use in investigating the quantum interference of photons. Finally in chapter 4 we move on to the work reported on in **publications I** and **II**. This chapter shows how photon bunching (or two-photon quantum interference) occurs in free-space transverse-spatial field structures of photons, with and without the spatial mode unitaries described in section 3.5. In chapter 5, we investigate how the techniques of the previous chapter could be applied to engineer so-called two-photon N00N states for transverse-spatial fields. We will also explore how such states of light could be useful in sensing applications, as was reported in **publications II** and **III**. Before drawing our conclusions in chapter 7, in chapter 6 we look into how the quantum interference effects of chapter 4 can give us more insight into one fundamental property of light called the Gouy phase [89, 90].

2 CLASSICAL AND QUANTUM THEORY OF STRUCTURED LIGHT

Although transverse spatial modes and quantum optics are very vibrant sub-fields of modern optics, some of the theory used in describing them goes back more than a century. Hence, going through all of this background does not fit the scope of this thesis. In this chapter, we will explore the most relevant parts of the theoretical framework utilized in this thesis. For a more complete description, one should look for the many textbooks covering these topics (e.g. [91–95]).

In this chapter, we will first see how paraxial light beams come about from Maxwell's equations and derive some important mathematical tools which we will use later to study the propagation of light. We will then look into the so-called canonical quantization of light and see how we can describe these paraxial light fields in the context of quantized light fields. Finally, we will have a brief look at some relevant concepts of nonlinear optics, which will become important when describing the operation of our photon pair source in Chapter 3.

2.1 Classical Linear Optics

In this section, we will briefly derive the paraxial wave equation (PWE), introduce one set of solutions to it, and finally explore how we can describe the propagation of these transverse field structures, in theory and simulation, through the angular spectrum representation.

2.1.1 Paraxial Wave Equation

To describe the propagation of light in free space, or when describing light at all, the best starting point is Maxwell's equations. As we are only concerned

with light beams in free space, we do not need to consider any charge densities or current densities, and hence the equations can be stated in the form

$$\begin{aligned} \nabla \cdot \tilde{\mathbf{E}} = 0, \text{ (a)} \quad \quad \quad \nabla \times \tilde{\mathbf{E}} = -\frac{\partial \tilde{\mathbf{B}}}{\partial t}, \text{ (b)} \\ \nabla \cdot \tilde{\mathbf{B}} = 0, \text{ (c)} \quad \text{and} \quad \nabla \times \tilde{\mathbf{B}} = \epsilon_0 \mu_0 \frac{\partial \tilde{\mathbf{E}}}{\partial t}, \text{ (d)} \end{aligned} \quad (2.1)$$

where $\tilde{\mathbf{E}}(\mathbf{r}, t)$ is the electric field vector at position \mathbf{r} and time t , $\tilde{\mathbf{B}}(\mathbf{r}, t)$ is the magnetic induction, ϵ_0 is the free space electric permittivity, μ_0 is the free space magnetic permeability, and ∇ operates on \mathbf{r} . The tilde on top of the parameters denotes that the field can include the rapidly oscillating temporal part of the optical field, in accordance with the notation of Boyd [95]. In order to describe light or electromagnetic waves, these equations can be used to derive the electromagnetic wave equations

$$\nabla^2 \tilde{\mathbf{E}} - \frac{1}{c^2} \frac{\partial^2}{\partial t^2} \tilde{\mathbf{E}} = 0, \text{ and} \quad \nabla^2 \tilde{\mathbf{B}} - \frac{1}{c^2} \frac{\partial^2}{\partial t^2} \tilde{\mathbf{B}} = 0, \quad (2.2)$$

where $c = 1/\sqrt{\epsilon_0 \mu_0}$ is the speed of light in vacuum. To arrive at the well-known Helmholtz equations, we further need to limit ourselves to light with a single frequency with the ansatz

$$\tilde{\mathbf{E}}(\mathbf{r}, t) = \frac{\mathbf{E}(\mathbf{r})}{2} e^{-i\omega t} + c.c. = \text{Re} \{ \mathbf{E}(\mathbf{r}) e^{-i\omega t} \}, \quad (2.3)$$

where ω is the chosen angular frequency, *c.c.* denotes a complex conjugate, and the operator Re takes only the real part of the complex field term. This then gives us the Helmholtz equations

$$\nabla^2 \mathbf{E} + k^2 \mathbf{E} = 0, \text{ and} \quad \nabla^2 \mathbf{B} + k^2 \mathbf{B} = 0, \quad (2.4)$$

where $k = \omega/c$ is the corresponding wavenumber.

Before we can finally get to the PWE, we need to address a few details and make some further assumptions. Here, we will use the vector potential \mathbf{A} in the Lorentz gauge to derive the PWE. The Lorentz gauge is chosen for convenience [92] and the vector potential is used in this derivation since the divergence equation of the electric field (equation (2.1)(a)) is not fulfilled in the paraxial approximation (read more about this in references [92, 96, 97]).

Although this needs to be done to keep the results consistent with Maxwell's equations during this derivation, it has been shown that the results derived using the vector potential are equivalent to the electric field solution in the lowest order approximation [97].

To get to the PWE, we start with the Helmholtz equation for the vector potential \mathbf{A} , and assume the polarization of the field to be transverse to the propagation direction (or optical axis). We denote polarization with a unit length polarization vector \mathbf{e} , and if we further assume a uniform polarization structure, we can focus on the scalar field A using $\mathbf{A} = \mathbf{e}A$. As the definition of a paraxial beam confines our light field to mostly propagate along an optical axis, we can make another ansatz $A(\mathbf{r}) = \mathcal{A}u(\mathbf{r})e^{ikz}$, where z is the direction of the optical axis and \mathcal{A} is the corresponding amplitude containing the units of the field in question (more about units of $u(\mathbf{r})$ in section 2.1.2). Since now the wavevectors of the field point mostly in the direction of the optical axis, we can assume that the amplitude distribution $u(\mathbf{r})$ changes slowly upon propagation in the z -direction. More precisely, this means that we can assume the transverse variations of $u(\mathbf{r})$ to become dominant, i.e.,

$$\left| \frac{\partial^2 u}{\partial z^2} \right| \ll |\nabla_{\perp}^2 u|,$$

when ∇_{\perp}^2 is the Laplacian acting on the transverse coordinates (x, y) . The last assumption we need is that we have a field profile which varies slowly enough with z to have

$$\left| \frac{\partial^2 u}{\partial z^2} \right| \ll k \left| \frac{\partial u}{\partial z} \right|,$$

after which we have the PWE

$$\nabla_{\perp}^2 u(\mathbf{r}) + 2ik \frac{\partial}{\partial z} u(\mathbf{r}) = 0.$$

Although the approximations required for deriving the PWE are well known and well documented elsewhere, because all light fields do not fall into the scope of these approximations, it is still important to restate and remember them when designing and simulating optical systems. When it comes to determining whether a specific beam of light is paraxial, different metrics can be used but one useful tool for defining the paraxiality of complex transverse light fields is

the paraxiality estimator introduced by Vaveliuk et al. [98].

Since all the experiments presented in this thesis were performed in the paraxial regime, we will not explore the effects of tightly focused light fields here. However, many of the findings and effects explored in this thesis should also apply beyond the paraxial regime.

2.1.2 Laguerre-Gaussian Modes

Having defined the PWE which governs the structure of the light fields we will use in our experiments, it is important to explore the fields fulfilling this equation. When defining fields that are acceptable solutions to the PWE (or the Helmholtz equation), it is convenient to start from a complete set of solutions to the equation and express the field as a superposition of the members of this set. There are different complete sets of solutions to the PWE, with one of the most well-known ones being the Hermite-Gaussian (HG) family of solutions which have a roughly rectangular shape and are a natural set of solutions to the PWE in Cartesian coordinates. A few other examples of complete sets of solutions to the PWE are Ince-Gaussian modes which have an elliptical symmetry [99], and the Bessel modes which have a transverse profile extending to infinity and can also be formulated to fulfil the Helmholtz equation [92].

The set of modes we will be using in this thesis are the Laguerre-Gaussian (LG) modes which are a natural set of solutions to the PWE in cylindrical coordinates (ρ, φ, z) . We define ρ as the radial distance from the optical axis, φ as the azimuthal angle in the plane perpendicular to the optical axis, and z as the distance along the optical axis. The normalized form of the LG modes can be written compactly in the form given below and in reference [100]

$$\begin{aligned}
 u_{\ell p}(\rho, \varphi, z) = & \sqrt{\frac{2p!}{\pi(|\ell| + p)!}} \frac{1}{w(z)} \left(\frac{\sqrt{2}\rho}{w(z)} \right)^{|\ell|} \exp\left(-\frac{\rho^2}{w^2(z)}\right) L_p^{|\ell|} \left(\frac{2\rho^2}{w^2(z)} \right) \\
 & \exp\left(i \left[\frac{\rho^2 k}{2R_c(z)} - (2p + |\ell| + 1) \arctan\left(\frac{z - z_0}{z_R}\right) + \ell\varphi \right]\right),
 \end{aligned} \tag{2.5}$$

where $L_p^{|\ell|}(\xi)$ is the generalized Laguerre polynomial [101]

$$L_p^{|\ell|}(\xi) = \sum_{m=0}^p (-1)^m \frac{(|\ell| + p)!}{(p - m)! (|\ell| + m)! m!} \xi^m, \quad (2.6)$$

from which the modes get their name, $w(z) = w_0 \sqrt{1 + [(z - z_0)/z_R]^2}$ is the beam radius, $R_c(z) = z (1 + [z_R/(z - z_0)]^2)$ is the radius of curvature, w_0 is the beam radius at the beam waist, $z_R = \frac{kw_0^2}{2}$ is the Rayleigh length, and z_0 is the position of the waist on the optical axis. From the form of this equation, it can be seen that the overall shape of the modes stays approximately the same upon propagation. Only the size of the modes $w(z)$ increases away from the focus due to diffraction, which is accompanied by a changing quadratic phase $\rho^2 k / (2R_c(z))$ and the Gouy phase $\Phi_G(z) = (2p + |\ell| + 1) \arctan\left(\frac{z - z_0}{z_R}\right)$.

The LG modes given in equation (2.5) form an orthonormal set, meaning that an overlap integral of any pair of LG modes takes the form

$$\int_0^{2\pi} \int_0^\infty \rho u_{\ell_1 p_1}(\rho, \varphi, z) (u_{\ell_2 p_2}(\rho, \varphi, z))^* d\varphi d\rho = \delta_{\ell_1 \ell_2} \delta_{p_1 p_2}, \quad (2.7)$$

where δ_{mn} is a Kronecker delta and $(\cdot)^*$ denotes complex conjugation. The orthogonality of the LG modes stems from the properties of the Laguerre polynomials and the orthogonality of the azimuthal phase terms $\exp(i\ell\varphi)$. Also note that the normalized form of LG modes given in equation (2.5), and used throughout this thesis, has units of $1/m$. Hence, although they describe the shape of the real electric, magnetic induction, or vector potential field structures used in the experiments, the amplitude distributions $u(\mathbf{r})$ used here are of this normalized form.

To plot these transverse-field structures, we use a combination of plotting the phase of the field using a colour map and the amplitude using the brightness of the colours. An example set of the 45 lowest order LG modes is plotted in figure 2.1. In the figure, the modes have been sorted into separate mode groups which are subsets of modes with the same Gouy phase. Hence, it is useful to characterize each mode group by the integer number used in the Gouy phase, which is $M = |\ell| + 2p + 1$ for LG modes. It should be noted that in the publications attached to the end of this thesis, intensity is used instead of amplitude in similar plots. However, when using intensity, slight modifications

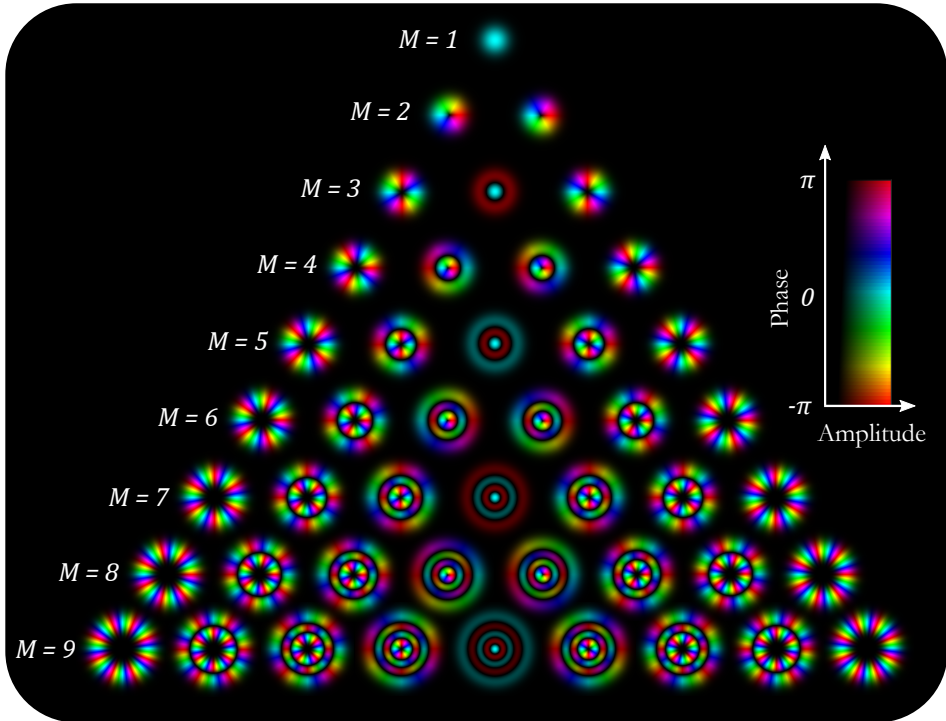


Figure 2.1 An example set of the first 45 lowest order LG modes. The plots are of the transverse structures of the beams at the beam waist. The modes are grouped in one mode order M per row which makes the structures of the higher order mode groups easy to intuit based on the emerging patterns. As mentioned in the text, the two-dimensional colour map shows the phase structure in colour and amplitude structure in the brightness of the colours at each point.

of the contrast and brightness of the image were used to make the wanted structures visible.

One of the reasons for the popularity of LG modes in research is the OAM they carry. This is distinct from the more well-known spin angular momentum (SAM) carried by the circular polarization of light which Poynting postulated already in 1909 [102] and which was measured in 1936 [103]. What the existence of these two seemingly separate angular momenta is hinting at, is that the total angular momentum of a localized finite light field, which can be defined as an integral over a volume V [92, 94, 104]

$$\mathbf{J} = \epsilon_0 \int_V \mathbf{r} \times (\mathbf{E} \times \mathbf{B}) dV, \quad (2.8)$$

can be divided into separate SAM and OAM terms. Sticking to the case where $\nabla \cdot \mathbf{E} = 0$ while using the vector potential $\mathbf{B} = \nabla \times \mathbf{A}$ and only looking at the divergenceless components of \mathbf{A}^\perp , these two separate momenta are [105]

$$\mathbf{S} = \epsilon_0 \int_V \mathbf{E} \times \mathbf{A}^\perp dV \quad \text{and} \quad \mathbf{L} = \epsilon_0 \sum_{i=1}^3 \int_V E_i (\mathbf{r} \times \nabla) A_i^\perp dV. \quad (2.9)$$

The connection between \mathbf{L} and OAM can be seen from its dependence on the choice of origin which leaves \mathbf{S} to be naturally associated with SAM due to its dependence on the polarization of the field and not the origin [94]. Although this separation will be useful later on, it should be noted that there are issues with defining these two separate parts as angular momenta and in performing the above separation of the total angular momentum for fields that are not divergenceless [92, 105, 106].

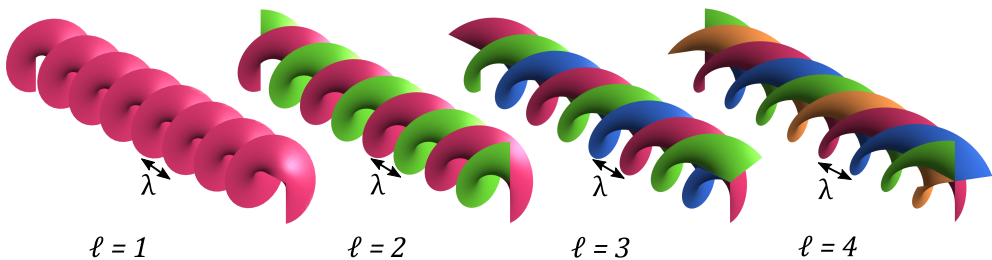


Figure 2.2 Examples of four different twisted wavefronts corresponding to OAM indices $\ell = \{1, 2, 3, 4\}$ of LG modes. The different colours are used to make the different arms of the helices more easily visible and λ denotes a single wavelength's worth of distance in the direction of the optical axis.

The OAM of light in LG modes was first pointed out in 1992 by Allen et al. [33], and was demonstrated to rotate particles in 1995 by He et al. [34, 107] (a more complete account of important first works on optical vortices and optical OAM can be found in [108]). The characteristic of OAM in LG modes is the azimuthal phase structure $e^{i\ell\varphi}$ which can also be seen in figure 2.1 as the rainbow-like structures around the azimuth of the modes. The index ℓ also characterizes the amount of OAM carried by a single photon in the given LG mode, since a photon occupying an LG mode with the phase structure $e^{i\ell\varphi}$ has $\ell\hbar$ OAM in the direction of the optical axis. Note that here \hbar refers to the reduced Planck constant. Physically, OAM is accompanied by a spiralling

wavefront (illustrated in figure 2.2) which also means that the electric field is not perfectly transverse to the optical axis.

In addition to the index ℓ which defines the OAM of an LG mode, the second index p defines the radial structure of the fields by giving us the number of dark rings the LG mode has. Although controlling this radial degree of freedom is equally important for many applications, there has not been as much interest in exploring the nature of this radial index. However, in the past ten years, a few studies exploring the nature of this radial index have been published [109, 110]. Furthermore, an article published by Plick and Krenn linked this index to a dilation of the field and named it the intrinsic hyperbolic momentum charge [111].

2.1.3 Angular Spectrum Representation

Having defined the set of paraxial modes we will use in the later chapters, we still need to know how we can conveniently calculate the propagation of any arbitrary transverse field. This method of calculating the propagation should also be easy to implement in simulations since that is crucial for our experimental methods. Fortunately, propagating through the angular spectrum representation (ASR) fulfils these requirements quite well.

To start deriving the ASR propagation formula in free space, we can initially assume that our light field is in an isotropic, homogeneous medium, without sources, and with a linear electromagnetic response. We can thus focus on a single frequency again and separate the fast-oscillating temporal part from our light field. This means that our light field satisfies the Helmholtz equations (2.4), and we can limit our investigation to the spatially dependent part of the electric field $\mathbf{E}(\mathbf{r})$ (see equation. (2.3)).

To describe the propagation of our field of light, we choose a propagation direction z and start with the electric field on a plane (x, y) perpendicular to this propagation direction. This selection of the propagation direction can be arbitrary, but for the paraxial beams, we always choose the optical axis as the axis along which our field propagates. We can then get the angular spectrum of this two-dimensional field structure, at an arbitrary position z_1 , by performing

a Fourier transform

$$\mathcal{E}(k_x, k_y; z_1) = \frac{1}{2\pi} \int_{-\infty}^{\infty} \int_{-\infty}^{\infty} \mathbf{E}(x, y, z_1) e^{-i(k_x x + k_y y)} dx dy, \quad (2.10)$$

where (k_x, k_y) are the transverse spatial-frequency coordinates in units of radians per meter. Since at any arbitrary point (k_x, k_y) , $\mathcal{E}(k_x, k_y; z_1)$ describes the amplitude of a plane wave travelling in a certain direction, it is sometimes also called the plane-wave spectrum. By taking a single plane-wave component of this angular spectrum and inserting it into the Helmholtz equation, we find that its evolution, upon a translation along the z -axis, can be stated as

$$\mathcal{E}(k_x, k_y; z_1) = \mathcal{E}(k_x, k_y; 0) e^{\pm i k_z(k_x, k_y) z_1}, \quad (2.11)$$

where $k_z(k_x, k_y) = \sqrt{k^2 - (k_x^2 + k_y^2)}$ is the wavevector in the direction of the optical axis. The factor $e^{\pm i k_z z_1}$ is often called a propagator and the sign of this phase term defines the propagation direction of the field. The positive sign refers here to the field propagating in the positive z -direction and the negative sign, conversely, to the negative z -direction. Using this translation of a plane wave, we can construct an equation for expressing the field at a position $z = z_1$, through a subsequent inverse Fourier transform, when we know the transverse field structure on a plane at $z = 0$

$$\mathbf{E}(x, y, z_1) = \frac{1}{2\pi} \int \int \mathcal{E}(k_x, k_y; 0) e^{i(k_x x + k_y y)} e^{\pm i k_z z_1} dk_x dk_y. \quad (2.12)$$

In the above equation, we have omitted the integration limits and will subsequently do so if our integration is over the whole space \mathbb{R}^n . The inverse Fourier transform effectively superimposes all of the possible plane-wave components with complex amplitude vectors $\mathcal{E}(k_x, k_y; 0)$ and plane-wave phases $e^{i(k_x x + k_y y \pm k_z z_1)}$, resulting in the total field structure at (x, y, z_1) . Note that the normalization factor $1/2\pi$ is placed in both the equation (2.10) and equation (2.12), to ensure that both operations conserve the normalization of the field being transformed (see equation (2.7) for the relevant LG mode normalization).

It should also be noted that since (k_x, k_y) are spatial frequencies, it is technically possible to have an imaginary k_z using its definition. Such a case, where

$k^2 < k_x^2 + k_y^2$ in free space, results in evanescent waves which corresponds to the propagator becoming $e^{-|k_z||z|}$. Since these evanescent waves only exist for higher spatial frequencies, some of the fine details of the initial field disappear once we reach the far-field, if such high frequencies are present in the initial field. Hence, propagation into the far field can be interpreted as a low-pass filtering of the initial transverse structure. However, since we will only be concerned with paraxial light fields in this thesis (i.e. $|k_\perp|/|k_z| \ll 1$), we won't be dealing with evanescent fields when using ASR propagation.

Most importantly for us, we see that calculating the propagation of monochromatic transverse fields only requires Fourier transforms and the multiplication of multiple complex numbers. Thus, performing these calculations on a computer can be done efficiently with the fast Fourier transform (FFT) algorithm.

2.2 Quantized Light

In the previous section, we introduced important equations governing the classical evolution of the electromagnetic fields that we will be using in this thesis. Although these equations are sufficient for describing some properties of all states of light, even single photons, the central theme of this thesis, i.e. quantum interference, requires a deeper look into the quantization of the light fields described in the previous section. Thus, in this section, we will be first working through the quantization of light using the so-called canonical quantization. We will then look at two types of quantum states of light and describe how we can include paraxial light beams in this framework. In the last part of this section, we will go through some details of how we can theoretically describe measurements and transformations of quantum states of light. This section is mostly based on Gerry's and Knight's book [93], Calvo et al.'s article [105], Audretsch's book [112], Grynberg et al.'s book [94], and the review article of Fabre and Treps [113].

2.2.1 Multimode Field Quantization

The canonical quantization of the electromagnetic field is crucial for describing theoretically the experiments of modern quantum optics. However, since large parts of entire chapters are dedicated to the canonical quantization in many

textbooks, e.g. [93, 94], here we will only have a brief overview.

We again start with the assumption of being in free space, without radiation sources or charges, meaning that Maxwell's equations still match equation (2.1). We will again be using the vector potential $\tilde{\mathbf{A}}(\mathbf{r}, t)$, but this time in the Coulomb gauge $\nabla \cdot \tilde{\mathbf{A}} = 0$, meaning that the electric and magnetic fields can be calculated from the vector potential using the equations

$$\tilde{\mathbf{B}} = \nabla \times \tilde{\mathbf{A}} \quad \text{and} \quad \tilde{\mathbf{E}} = -\frac{\partial \tilde{\mathbf{A}}}{\partial t}. \quad (2.13)$$

With our free space conditions, the vector potential also satisfies the wave equation

$$\nabla^2 \tilde{\mathbf{A}} - \frac{1}{c^2} \frac{\partial^2}{\partial t^2} \tilde{\mathbf{A}} = 0, \quad (2.14)$$

which is identical to the ones fulfilled by the electric and magnetic fields (see equation (2.2)).

We then model free space as a cubic cavity with a side length L . The walls of this cavity have to be perfectly reflecting and it should be arbitrarily large, allowing us to take $L \rightarrow \infty$ at any point. This cavity allows us to enforce periodic boundary conditions for the cube faces, i.e., $e^{ik_x x} = e^{ik_x(x+L)}$, limiting the set of allowed wavevectors to be

$$\mathbf{k} = \frac{2\pi}{L} [m_x, m_y, m_z]^T, \quad (2.15)$$

where $[x, y, z]$ is a three-dimensional horizontal vector, $[\cdot \cdot \cdot]^T$ denotes a transpose, and $\{m_i\}$ is a set of three integers.

As we saw in section 2.1.3, we can decompose a light field into a set of plane-wave components. Although in section 2.1.3 we only did this for two-dimensional field structures, this same process can also be done for a three-dimensional field and it produces a sum of plane waves in our finite cavity

$$\tilde{\mathbf{A}}(\mathbf{r}, t) = \sum_{\mathbf{k}, s} \mathbf{e}_{\mathbf{k}, s} \left[\tilde{A}_{\mathbf{k}, s}(t) e^{i\mathbf{k} \cdot \mathbf{r}} + \tilde{A}_{\mathbf{k}, s}^*(t) e^{-i\mathbf{k} \cdot \mathbf{r}} \right]. \quad (2.16)$$

In the above equation, the sum is performed over the wavevectors allowed by the cavity (see equation (2.15)) and the two orthonormal polarizations (s) connected to the polarization vector $\mathbf{e}_{\mathbf{k}, s}$. The time-dependent complex amplitudes

$\tilde{A}_{\mathbf{k},s}(t)$ are reminiscent of the plane-wave amplitudes used in equation (2.12) but this time for a discrete set of wavevectors and with an included time dependence. The polarization vectors are assumed to be real, for simplicity, and with the Coulomb gauge, the vector potential can be shown to be transverse ($\mathbf{k} \cdot \mathbf{e}_{\mathbf{k},s} = 0$). In the rest of this section the summing over \mathbf{k} and s is replaced by a single index j . Note that we can replace the sum in equation (2.16) by an integral when taking the size of our cavity to be infinitely large in free space. When performing this switch, one needs to take into account the density of plane-wave modes in our box (see references [93, 114] for more details).

Using the wave equation (equation (2.14)) and the Coulomb gauge, we find a familiar-looking set of solutions for the complex amplitudes of equation (2.16)

$$\tilde{A}_j(t) = A_j e^{-i\omega_j t}, \text{ with } \tilde{A}_j(0) = A_j. \quad (2.17)$$

Placing now equation (2.16) into Eqs. (2.13), we can write the electric and magnetic fields as

$$\begin{aligned} \tilde{\mathbf{E}}(\mathbf{r}, t) &= i \sum_j \omega_j \mathbf{e}_j \left[A_j e^{i(\mathbf{k}_j \cdot \mathbf{r} - \omega_j t)} - A_j^* e^{-i(\mathbf{k}_j \cdot \mathbf{r} - \omega_j t)} \right], \\ \tilde{\mathbf{B}}(\mathbf{r}, t) &= \frac{i}{c} \sum_j \omega_j (\boldsymbol{\kappa}_j \times \mathbf{e}_j) \left[A_j e^{i(\mathbf{k}_j \cdot \mathbf{r} - \omega_j t)} - A_j^* e^{-i(\mathbf{k}_j \cdot \mathbf{r} - \omega_j t)} \right], \end{aligned} \quad (2.18)$$

where $\mathbf{k}_j = |\mathbf{k}_j| \boldsymbol{\kappa}_j$. If we then insert these equations into the formula for the energy carried by the field, we obtain a solution for the field energy of the form

$$H = \frac{1}{2} \int_V \epsilon_0 \tilde{\mathbf{E}} \cdot \tilde{\mathbf{E}} + \frac{1}{\mu_0} \tilde{\mathbf{B}} \cdot \tilde{\mathbf{B}} \, dV = 2\epsilon_0 V \sum_j \omega_j^2 A_j^* A_j, \quad (2.19)$$

where $V = L^3$. Before we can perform the canonical quantization of this field, we still need to define canonical conjugate variables (q_j, p_j) for each mode. One convenient way to define them is as

$$A_j = \frac{1}{2\omega_j \sqrt{\epsilon_0 V}} [\omega_j q_j + i p_j], \quad (2.20)$$

which changes the field energy to

$$H = \frac{1}{2} \sum_j (p_j^2 + \omega_j^2 q_j^2), \quad (2.21)$$

which is identical to a sum of the energies of different harmonic oscillators with a mass $m = 1$. From this comparison, we infer that p_j and q_j fulfil the role of canonically conjugate variables in the classical Hamilton equations of the system. For a more rigorous demonstration of their fulfilment of these roles, see reference [94] where the authors use the same assumptions and starting point used here, with a slightly different definition for p_j and q_j .

As we have finally identified the two conjugate canonical variables, we can perform the quantization step. This step simply involves associating the above defined p_j and q_j with Hermitian operators \hat{p}_j and \hat{q}_j with the canonical commutation relations

$$\begin{aligned} [\hat{q}_j, \hat{q}_{j'}] &= 0 = [\hat{p}_j, \hat{p}_{j'}] \\ [\hat{q}_j, \hat{p}_{j'}] &= i\hbar\delta_{jj'} = \delta_{\mathbf{k}\mathbf{k}'}\delta_{ss'}. \end{aligned} \quad (2.22)$$

The caret is used to distinguish operators from other mathematical objects. For convenience, we further define the non-Hermitian annihilation and creation operators for each mode of the field as

$$\hat{a}_j = \frac{1}{\sqrt{2\hbar\omega_j}} [\omega_j\hat{q}_j + i\hat{p}_j] \quad \text{and} \quad (2.23)$$

$$\hat{a}_j^\dagger = \frac{1}{\sqrt{2\hbar\omega_j}} [\omega_j\hat{q}_j - i\hat{p}_j], \quad (2.24)$$

respectively. Note that here $(\cdot)^\dagger$ denotes a Hermitian conjugate. Based on the commutation relation of the conjugate canonical variables, we can calculate the commutation relation of the creation and annihilation operators

$$\begin{aligned} [\hat{a}_j, \hat{a}_{j'}] &= 0 = [\hat{a}_j^\dagger, \hat{a}_{j'}^\dagger] \\ [\hat{a}_j, \hat{a}_{j'}^\dagger] &= \delta_{jj'} = \delta_{\mathbf{k}\mathbf{k}'}\delta_{ss'}, \end{aligned} \quad (2.25)$$

which are the same for any bosonic system, up to a chosen normalization constant.

With the quantization of the multi-mode field, the total field energy, electric

field component, and magnetic field component get an operator form as well

$$\hat{H} = \sum_j \hbar\omega_j \left(\hat{a}_j^\dagger \hat{a}_j + \frac{1}{2} \right), \quad (2.26)$$

$$\hat{\mathbf{E}}(\mathbf{r}, t) = i \sum_j \left(\frac{\hbar\omega_j}{2\epsilon_0 V} \right)^{\frac{1}{2}} \mathbf{e}_j \left[\hat{a}_j e^{i(\mathbf{k}_j \cdot \mathbf{r} - \omega_j t)} - \hat{a}_j^\dagger e^{-i(\mathbf{k}_j \cdot \mathbf{r} - \omega_j t)} \right], \quad (2.27)$$

$$\hat{\mathbf{B}}(\mathbf{r}, t) = i \sum_j \left(\frac{\hbar\omega_j}{2\epsilon_0 V} \right)^{\frac{1}{2}} \frac{(\mathbf{k}_j \times \mathbf{e}_j)}{\omega_j} \left[\hat{a}_j e^{i(\mathbf{k}_j \cdot \mathbf{r} - \omega_j t)} - \hat{a}_j^\dagger e^{-i(\mathbf{k}_j \cdot \mathbf{r} - \omega_j t)} \right]. \quad (2.28)$$

Note that the annihilation and creation operators in the above equations should be interpreted as operators in the Heisenberg picture at $t = 0$, i.e., $\hat{a}_j(t) = \hat{a}_j(0)e^{-i\omega t} = \hat{a}_j e^{-i\omega t}$. Since the equations (2.26)-(2.28) describe observables, the operators need to be Hermitian. There is also an additional physical meaning of the combined operator $\hat{n}_j = \hat{a}_j^\dagger \hat{a}_j$ which is often dubbed the number operator since it gives us the number of photons in the mode. This interpretation becomes clearer if we compare the Hamiltonian to the energy of a quantum harmonic oscillator $E_n = \hbar\omega (n + 1/2)$ [115]. Hence, equation (2.26) also gives us the amount of energy each photon, or excitation of the field, adds to the total energy of the field. Additionally, from Eqs. (2.27) and (2.28) we get the electric and magnetic field amplitudes per photon which are $(\hbar\omega_j/(\epsilon_0 V))^{1/2}$ and $(\hbar\omega_j/(\epsilon_0 V c^2))^{1/2}$, respectively.

Now that we know how to quantize a field of light starting from Maxwell's equations, we can use this formalism to describe the states of light we have in our experimental system. Here we will split this discussion into two parts. First, we will look into a few different photon number distributions that we will be using for our plane-wave modes and afterwards, we will see how we can take these same states and extend them to the paraxial beams of light.

2.2.1.1 Fock States

With the ladder operators defined in Eqs. (2.23) and (2.24), we are now able to describe different states of light using this formalism. Here we will focus on two types of states, Fock states and coherent states. The first one of these two, Fock states or photon number states, are eigenstates of the Hamiltonian

we introduced in equation (2.26)

$$\hat{H} |n\rangle_j = (n\hbar\omega_j + E_{ZPE}) |n\rangle_j = E |n\rangle_j. \quad (2.29)$$

Since they are an eigenstate of the Hamiltonian, Fock states have a well-defined energy. This also means that these states are eigenstates of the number operator \hat{n}_j , i.e., they have a well-defined number of photons occupying each mode. This is also the reason why they are called “photon number states”. Equation (2.29) also interestingly points out a few other curious consequences of the quantization of the electromagnetic field. Namely, the zero point energy (ZPE) $E_{ZPE} = \sum_j \hbar\omega_j/2$, which tends to infinity due to the infinite amount of radiation modes in our universe. This energy is accompanied by vacuum fluctuations which can be seen when calculating the expectation value and variance of the electric field operator equation (2.27) for the vacuum state. Such a calculation gives us a zero average field, as expected, but a non-zero value for its fluctuations. Although the infinite energy and vacuum fluctuations cause issues such as the aforementioned infinite energies, both of them also play a role in measurable effects, e.g., vacuum fluctuations in spontaneous emission and ZPE in the Casimir effect.

Note that in equation (2.29), and throughout the thesis, we use the Dirac notation to denote a quantum state. In equation (2.29), we have a state where n photons occupy the mode j while all of the other modes just contain vacuum $|0\rangle_i$. Hence, the Fock state $|n\rangle_j$ could also be stated in a more complete form in a few different ways:

$$\begin{aligned} |n\rangle_j &= |0\rangle_1 \otimes |0\rangle_2 \otimes |0\rangle_3 \otimes \cdots \otimes |n\rangle_j \otimes \cdots \\ &= |0\rangle_1 |0\rangle_2 |0\rangle_3 \cdots |n\rangle_j \cdots \\ &= |0, 0, 0, \dots, n, \dots\rangle. \end{aligned} \quad (2.30)$$

In this thesis, we will usually omit all of the vacuum modes in our states and will adopt the notation of reference [93] for a state where all of the modes are in vacuum $|\{0\}\rangle$.

Besides being eigenstates of the Hamiltonian, the Fock states have some other useful properties. Firstly, the effects of the annihilation and creation operators on the Fock states are quite intuitive. The annihilation operator

removes a quantum of energy, or a photon, from a photon number state

$$\hat{a}_j |n\rangle_j = \sqrt{n} |n-1\rangle_j, \quad \hat{a}_j |0\rangle_j = 0 \quad (2.31)$$

and the creation operator conversely adds a quantum of energy

$$\hat{a}_j^\dagger |n\rangle_j = \sqrt{n+1} |n+1\rangle_j. \quad (2.32)$$

The Fock states are also orthogonal to each other, meaning that when modes corresponding to indices i and j are part of an orthonormal set of modes, we have

$${}_j\langle m|n\rangle_i = \delta_{nm}\delta_{ji}. \quad (2.33)$$

With these definitions, we can verify that the photon number operator actually gives us the number of photons in a number state ${}_j\langle n|\hat{a}_j^\dagger\hat{a}_j|n\rangle_j = n$. We can also derive a general expression for constructing of photon number state from vacuum

$$|n\rangle_j = \frac{(\hat{a}_j^\dagger)^n}{\sqrt{n!}} |\{0\}\rangle. \quad (2.34)$$

A few other interesting features of the Fock states are that, as eluded to before, the fluctuation in the photon number of such a state is zero ${}_j\langle n|(\Delta\hat{n}_j)^2|n\rangle_j = \langle\hat{n}_j^2\rangle - \langle\hat{n}_j\rangle^2 = 0$. Also, in contrast to a classical description of a light field, Fock states of light do not have a well-defined phase in which the electric field would oscillate. This latter detail is accompanied by an electric field that is zero on average ${}_j\langle n|\hat{\mathbf{E}}(\mathbf{r}, t)|n\rangle_j = 0$. There are of course other interesting features that these number states have but we will explore those in chapters 4–6 as these states will be the main workhorse in our investigations.

At this point, it is also useful to note that the space of states we have constructed above is sometimes called the total Fock space. Mathematically, it can be constructed as a direct sum of Hilbert spaces with a fixed number of identical particles, while taking into account the permutation symmetries of the particles in question [116, 117].

2.2.1.2 Coherent States

Fock states are a class of states of light that are quite rare in laboratories and nature. Conversely, thermal light states, which will not be described in this thesis, are quite prevalent in all aspects of our daily lives. Such states are prevalent because they describe the light emitted in black-body radiation. In between these two cases are coherent states of light which most closely correspond to the usual picture of a classical light field. Coherent states also describe well the properties of laser light.

Coherent states, often denoted as $|\alpha\rangle_j$ for a single mode j , are defined as eigenstates of the annihilation operator

$$\hat{a}_j |\alpha\rangle_j = \alpha |\alpha\rangle_j. \quad (2.35)$$

These states can be constructed as a coherent superposition of Fock states according to

$$|\alpha\rangle_j = e^{-\frac{1}{2}|\alpha|^2} \sum_{n=0}^{\infty} \frac{\alpha^n}{\sqrt{n!}} |n\rangle_j, \quad (2.36)$$

where we can see that they have an intrinsic uncertainty in the number of photons with a Gaussian-like shape for this photon number distribution averaged around $\langle \hat{n}_j \rangle_\alpha = |\alpha|^2$. More precisely, the distribution in the photon number of a coherent state is in fact Poissonian, meaning that the photon number uncertainty is $\langle \Delta \hat{n}_j \rangle_\alpha = |\alpha|$, giving us the intrinsic photon number uncertainty of coherent states which is also linked to the shot-noise limit [118]. Coherent states are not an orthogonal set since the overlap between two coherent states occupying the same mode is

$${}_j\langle \beta | \alpha \rangle_j = e^{-\frac{1}{2}(|\beta|^2 + |\alpha|^2 - 2\beta^* \alpha)}. \quad (2.37)$$

The reason why coherent states are perceived as classical is that the expectation value of the electric field behaves comparably to a classical wave (here we assume a plane-wave mode j polarized in the x-direction)

$${}_j\langle \alpha | \hat{E}_{x,j} | \alpha \rangle_j = 2|\alpha| \left(\frac{\hbar \omega_j}{2\epsilon_0 V} \right)^{\frac{1}{2}} \sin(\omega_j t - \mathbf{k}_j \cdot \mathbf{r} - \theta), \quad (2.38)$$

when $\alpha = |\alpha|e^{i\theta}$. Contrary to a classical field, however, coherent states have an uncertainty in the number of photons which is also accompanied by an uncertainty in the phase and amplitude of the electric field. One instructive

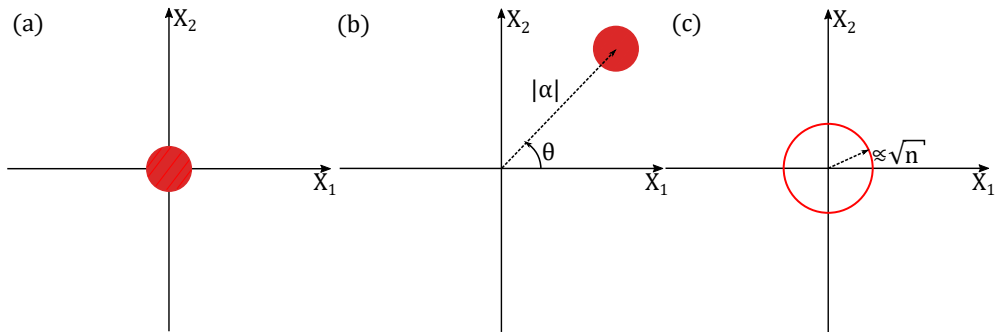


Figure 2.3 A phase-space representation of (a) a vacuum state, (b) a coherent state, and (c) a Fock state. The solid circles represent the uncertainty in defining the vacuum and coherent states in phase space. In these pictures, the distance from the origin is related to the photon number and the angular displacement from the X_1 -axis is linked to the phase of the field associated with the state. Hence, the coherent state has a reasonably well-defined phase and photon number (with some uncertainty) and the Fock state has a well-defined photon number but a completely undefined phase. In (c) these properties of the Fock state are represented by the thinness of the ring, giving the well-defined photon number, and the occupation of every angular position showing the undefined phase. The figure is based on a figure in reference [93] and is made as a qualitative representation of these states since an accurate picture of the phase space cannot be drawn due to the uncertainty. Characteristic functions such as the Wigner function provide a more complete visual representation of these states (see, e.g., reference [93] for a description of characteristic functions).

way of visualising both of these uncertainties is through a phase-space picture. The phase-space can be defined through the quadrature operators, which are dimensionless versions of the canonical position and momentum operators

$$\hat{X}_{1,j} = \frac{1}{2}(\hat{a}_j + \hat{a}_j^\dagger), \quad (2.39)$$

$$\hat{X}_{2,j} = \frac{1}{2i}(\hat{a}_j - \hat{a}_j^\dagger). \quad (2.40)$$

Phase-space pictures of a single-mode vacuum state and coherent state can be found in Figure 2.3, along with a phase-space picture of a Fock-state constructed in an analogous way. Note that although we call these phase-space pictures, these images are only qualitative and differ from the classical phase-space picture through the intrinsic uncertainty in the pictured states. In these images,

we see that the vacuum and coherent states have a similar spread through the phase space denoting the identical uncertainty these states possess. This is why coherent states are also categorized as displaced vacuum states with an average photon number $|\alpha|^2$ and phase $\theta = \arg(\alpha)$, where \arg is an operator giving us the phase or argument of a complex number. Thus, coherent states can also be defined through a displacement operator $\hat{D}_j(\alpha) = \exp(\alpha\hat{a}_j^\dagger - \alpha^*\hat{a}_j)$ as

$$|\alpha\rangle_j = \hat{D}_j(\alpha) | \{0\} \rangle. \quad (2.41)$$

Both the vacuum state and coherent states also minimize the corresponding Heisenberg-type uncertainty product between the two quadratures.

The phase-space picture presented here is mostly added as an instructive image to highlight the difference between the properties of coherent states and Fock states. However, such phase space representations are much more instructive when describing the behaviour of other useful quantum states such as squeezed states [93], which are not in the scope of this thesis.

2.2.2 Quantized Paraxial Beams

To describe the states of light which we use in the experimental section, we still need to go from the quantized plane-wave modes of the previous sections to quantized versions of the paraxial modes described in section 2.1. To start, we should remember that, for any set of solutions to the wave equation, their superposition also forms an acceptable solution due to the linearity of the wave equation

$$\tilde{\mathbf{E}}(\mathbf{r}, t) = \sum_j \mathcal{E}_j \tilde{\mathbf{f}}_j(\mathbf{r}, t) + c.c.. \quad (2.42)$$

Here we have chosen an arbitrary electric field $\tilde{\mathbf{E}}(\mathbf{r}, t)$ that was represented as a superposition of orthonormal vector modes $\tilde{\mathbf{f}}_j(\mathbf{r}, t)$ with the corresponding complex amplitudes \mathcal{E}_j . Also, in comparison to section 2.1.2, here the normalized field structures are more general and include the field polarization and temporal structure as well. The sum in equation (2.42) is sufficient for describing any arbitrary electric field in free space if we restrict ourselves to a volume V as in

section 2.2.1, where we can have a set of orthonormal modes

$$\frac{1}{V} \int_V \tilde{\mathbf{f}}_j^*(\mathbf{r}, t) \cdot \tilde{\mathbf{f}}_{j'}(\mathbf{r}, t) d^3\mathbf{r} = \delta_{jj'}, \quad (2.43)$$

which can be used to decompose any electromagnetic wave within the volume. Similarly to section 2.2.1, the volume is an arbitrary choice which can be extended to infinity.

When we have a finite and complete basis of orthonormal plane-wave modes $\{\tilde{\mathbf{f}}_j\}$, we can construct any other set of basis modes as a superposition of these modes. Limiting ourselves to a finite number of modes d can be often justified by the experimental system only accommodating a fixed number of modes. The new basis can be calculated as

$$\tilde{\mathbf{g}}_m(\mathbf{r}, \mathbf{t}) = \sum_{j=1}^d U_m^j \tilde{\mathbf{f}}_j(\mathbf{r}, \mathbf{t}), \quad (2.44)$$

where U_m^j are the complex components of a unitary transformation U , e.g. mapping a finite set of plane-wave modes to the new set of orthonormal field structures $\{\tilde{\mathbf{g}}_m\}$. The unitarity of the transformation ensures that the new set of basis modes is also orthonormal.

Taking these same arguments to quantized electromagnetic fields, we can express any mode of a quantized electromagnetic field as a superposition of another finite set of modes. To perform this change in basis modes, we can again use a unitary transformation U , but this time operating on the field creation and annihilation operators

$$\hat{b}_m^\dagger = \sum_j U_m^j \hat{a}_j^\dagger, \quad (2.45)$$

$$\hat{a}_j = \sum_m U_m^j \hat{b}_m. \quad (2.46)$$

Here the unitarity of the matrix U ensures that the commutation relation of these new operators \hat{b}_m and \hat{b}_m^\dagger are still of the same form expressed in equation (2.25). Hence, we can simply change the basis of the quantized plane-wave modes used in section 2.2.1, and construct the wanted set of modes as a superposition of them. Thus, if we would associate the modes \hat{a}_j with the plane-wave

modes of the previous section, the electric field operator in this new basis takes the form

$$\hat{\mathbf{E}}(\mathbf{r}, t) = \sum_m \left(\mathcal{F}_m^{(1)} \tilde{\mathbf{g}}_m(\mathbf{r}, t) \hat{b}_m + H.c. \right), \quad (2.47)$$

where $H.c.$ denotes a Hermitian conjugate. The term giving us the electric field per photon $\mathcal{F}_m^{(1)}$ in the above equation can be calculated from the normalization procedure of the modes $\tilde{\mathbf{g}}_m$, and is of the form

$$\left(\mathcal{F}_m^{(1)} \right)^2 = \sum_j \left(\frac{\hbar \omega_j}{2\epsilon_0 V} \right) |U_m^j|^2. \quad (2.48)$$

Note that in this general case, the new normalized field structures $\tilde{\mathbf{g}}_m$ are of the form

$$\tilde{\mathbf{g}}_m(\mathbf{r}, \mathbf{t}) = \frac{1}{\mathcal{F}_m^{(1)}} \sum_j \left(\frac{\hbar \omega_j}{2\epsilon_0 V} \right)^{\frac{1}{2}} U_m^j \tilde{\mathbf{f}}_j(\mathbf{r}, \mathbf{t}), \quad (2.49)$$

where the frequency-dependent scaling factor in the sum over the frequencies might cause the new basis modes $\{\tilde{\mathbf{g}}_m\}$ to be nonorthogonal [113]. However, in the case of only a narrow band of frequencies around ω_0 being considered (i.e. assuming a single frequency), equation (2.49) takes the same form as equation (2.44) and the orthonormality of the modes is guaranteed again [113]. In this narrow-band approximation we also have $\mathcal{F}_j^{(1)} = ((\hbar \omega_0)/(2\epsilon_0 V))^{1/2}$.

If our narrow-band set of modes $\{\tilde{\mathbf{g}}_m\}$ is additionally limited to being paraxial to the z -axis (with a mean wavevector \mathbf{k}_0), we can simplify equation (2.47) by assuming the approximate form

$$\hat{\mathbf{E}}(\mathbf{r}, t) \approx \left(\frac{\hbar \omega_0}{2\epsilon_0 V} \right)^{1/2} \left[\sum_j \left(e^{i(k_0 z - \omega_0 t)} \mathbf{g}_j(\mathbf{r}, t) \hat{a}_j \right) + H.c. \right], \quad (2.50)$$

where we have envelope structures $\mathbf{g}_j(\mathbf{r}, t)$ that vary slowly compared to the scale of the oscillation period and the wavelength. Hence, it would seem that we can simply switch from the already quantized plane-wave basis to the LG mode basis using a unitary mapping and have our quantized LG beams of light.

Of course, there are some details to keep in mind before making this step. First of all, as we already discussed in section 2.1.1, one should keep in mind the assumptions made in the paraxial approximation. One of the constraints for

choosing an orthonormal basis $\tilde{\mathbf{f}}_j(\mathbf{r}, t)$ for expressing our classical or quantized light field is that it needs to satisfy Maxwell's equations. Hence, the same caveats given in the classical paraxial approximation extend to the quantized version of the fields. However, we do know from experiments that the paraxial approximation does hold quite well for quantized fields as well. Finally, as we are working in free space, we should take our sum of plane-wave modes into the continuous regime.

We can start working closer towards the quantized LG modes by staying in the Coulomb gauge, as defined in section 2.2.1, and first writing our vector potential operator in a continuous plane-wave basis. We write the operator using so-called operator densities $\hat{a}(\mathbf{k})$ and $\hat{a}^\dagger(\mathbf{k})$ [119], defined in such a way that we have [105]

$$\hat{A}(\mathbf{r}, t) = \sum_{\sigma} \int d^3\mathbf{k} \sqrt{\frac{\hbar}{16\pi^3\epsilon_0\omega(\mathbf{k})}} \left[\mathbf{e}_{\sigma}(\mathbf{k}) \hat{a}_{\sigma}(\mathbf{k}) e^{i(\mathbf{k}\cdot\mathbf{r} - \omega(\mathbf{k})t)} + H.c. \right]. \quad (2.51)$$

The operator densities follow the commutation relations

$$\left[\hat{a}_{\sigma}(\mathbf{k}), \hat{a}_{\sigma'}^{\dagger}(\mathbf{k}') \right] = \delta_{\sigma\sigma'} \delta^{(3)}(\mathbf{k} - \mathbf{k}') \quad (2.52)$$

$$\left[\hat{a}_{\sigma}^{\dagger}(\mathbf{k}), \hat{a}_{\sigma'}^{\dagger}(\mathbf{k}') \right] = 0 = \left[\hat{a}_{\sigma}(\mathbf{k}), \hat{a}_{\sigma'}(\mathbf{k}') \right], \quad (2.53)$$

where $\delta^{(N)}(\boldsymbol{\xi} - \boldsymbol{\xi}')$ denotes a d -dimensional Dirac delta function. In equation (2.51), we have also now switched our polarization labels to σ , denoting that the polarization unit vectors $\mathbf{e}_{\sigma}(\mathbf{k})$ are complex and either right-handed circular ($\sigma = +1$) or left-handed circular ($\sigma = -1$).

From this general form of the vector potential operator we can get to the form of a quantized LG mode by following the steps¹ in reference [105], which gives us

$$\begin{aligned} \hat{A}(\mathbf{r}, t) \approx \sum_{\sigma, \ell, p} \int_0^{\infty} dk_0 \sqrt{\frac{\hbar}{4\pi\epsilon_0 ck_0}} & \left[\mathbf{e}_{\sigma} \hat{a}_{\sigma, \ell, p}(k_0) e^{ik_0(z-ct)} u_{\ell p}(\mathbf{r}_{\perp}, z; k_0) \right. \\ & \left. + H.c. \right], \end{aligned} \quad (2.54)$$

¹Note that in this derivation, and in some other derivations performed in this thesis, we need to exchange the order of sums and integrations. Although we assume this to hold in all our derivations here, we should remember that such equivalences do not hold in general.

where the field is taken to be paraxial to the z -axis. The field is also assumed to propagate in the positive z -direction ($k_0 > 0$), without a loss of generality. The restriction to the positive half-space is done to avoid issues in the paraxial approximation $k_z = k_0 \left(1 - \frac{|\mathbf{k}_\perp|^2}{2k_0^2}\right)$, where $\mathbf{k} = \mathbf{k}_\perp + k_z \mathbf{u}_z$, \mathbf{u}_z is a unit vector in the positive z -direction, and \mathbf{k}_\perp is the wavevector transverse to the optical axis. In equation (2.54), $u_{\ell p}$ is the same field structure that was given in equation (2.5), \mathbf{r}_\perp is a two-dimensional position vector perpendicular to the optical axis, and the annihilation and creation operator are defined similarly to Eqs. (2.45) and (2.46). However, this time the sum is changed to a double integral

$$\hat{a}_{\sigma,\ell,p}(k_0) = \int d^2\mathbf{k}_\perp \mathcal{U}_{\ell p}^*(\mathbf{k}_\perp) \hat{a}_\sigma(\mathbf{k}_\perp, k_0), \quad (2.55)$$

where $\mathcal{U}_{\ell p}^*(\mathbf{k}_\perp)$ is a Fourier transformed profile of an LG mode at $z = 0$ and the $\hat{a}_\sigma(\mathbf{k}_\perp, k_0)$ operator follows a familiar commutation relation

$$\left[\hat{a}_\sigma(\mathbf{k}_\perp, k_0), \hat{a}_{\sigma'}^\dagger(\mathbf{k}'_\perp, k'_0) \right] = \delta_{\sigma\sigma'} \delta^{(2)}(\mathbf{k}_\perp - \mathbf{k}'_\perp) \delta(k_0 - k'_0). \quad (2.56)$$

Through the above definitions, and the orthonormality of the LG modes, we can derive the expected commutation relations for the operators in equation (2.54)

$$\left[\hat{a}_{\sigma,\ell,p}(k_0), \hat{a}_{\sigma',\ell',p'}^\dagger(k'_0) \right] = \delta_{\sigma\sigma'} \delta_{\ell\ell'} \delta_{pp'} \delta(k_0 - k'_0). \quad (2.57)$$

To complete our look into the angular momentum of light, we can now give a quantized form of the angular momentum operators using the quantized LG modes. We will not go into the details of the derivation here, but more information can be found by following the description of the derivation in reference [105]. According to this reference, the z -components of the spin and orbital angular momentum operators take the form

$$\hat{L}_z = \hbar \sum_{\sigma,\ell,p} \ell \int_0^\infty dk_0 \hat{a}_{\sigma,\ell,p}^\dagger(k_0) \hat{a}_{\sigma,\ell,p}(k_0) \quad (2.58)$$

$$\hat{S}_z = \hbar \sum_{\sigma,\ell,p} \sigma \int_0^\infty dk_0 \hat{a}_{\sigma,\ell,p}^\dagger(k_0) \hat{a}_{\sigma,\ell,p}(k_0), \quad (2.59)$$

The above equations tell us that each photon occupying an LG mode with index ℓ carries $\hbar\ell$ amount of OAM in the propagation direction of the paraxial field, as

was also mentioned in section 2.1.2, and the SAM depends on the polarization of the field. It also shows that LG-mode Fock states are eigenstates of both of these observables which commute with each other. We should note that although we can define these two commuting operators in the above-defined paraxial approximation, the general three-dimensional OAM and SAM operators of light fields are not true angular momentum operators since they do not follow the usual commutation relations of angular momentum operators [105].

Since we have now defined the creation and annihilation operators for LG modes in free space, we can write any paraxial quantum state of light in the LG basis. For example, a single-photon state would take the form

$$|\Psi\rangle = \sum_{\sigma,\ell,p} \int_0^\infty dk_0 C_{\sigma,\ell,p}(k_0) \hat{a}_{\sigma,\ell,p}^\dagger(k_0) |\{0\}\rangle, \quad (2.60)$$

where the coefficients $C_{\sigma,\ell,p}$ have to be normalized such that

$$\sum_{\sigma,\ell,p} \int_0^\infty |C_{\sigma,\ell,p}(k_0)|^2 dk_0 = 1.$$

One more useful modification we can make to this expression is converting it to real space by defining one more set of creation and annihilation operators

$$\hat{a}_\sigma(\mathbf{r}_\perp, k_0) = \frac{1}{2\pi} \int d^2\mathbf{k}_\perp e^{i(\mathbf{k}_\perp \cdot \mathbf{r}_\perp)} \hat{a}_\sigma(\mathbf{k}_\perp, k_0). \quad (2.61)$$

The commutation relations of the above operator can be derived from equation (2.56) and they are $[\hat{a}_\sigma(\mathbf{r}_\perp, k_0), \hat{a}_{\sigma'}^\dagger(\mathbf{r}'_\perp, k_0)] = \delta_{\sigma\sigma'} \delta^{(2)}(\mathbf{r}_\perp - \mathbf{r}'_\perp) \delta(k_0 - k'_0)$. This allows us to rewrite the state in equation (2.60), using equation (2.55) and the inverse transform of the one in equation (2.61)

$$\hat{a}_\sigma(\mathbf{k}_\perp, k_0) = \frac{1}{2\pi} \int d^2\mathbf{r}_\perp e^{-i(\mathbf{k}_\perp \cdot \mathbf{r}_\perp)} \hat{a}_\sigma(\mathbf{r}_\perp, k_0), \quad (2.62)$$

which gives us

$$\begin{aligned} |\Psi\rangle &= \sum_{\sigma,\ell,p} \int_0^\infty dk_0 C_{\sigma,\ell,p}(k_0) \int d^2\mathbf{r}_\perp \hat{a}_\sigma^\dagger(\mathbf{r}_\perp, k_0) \\ &\times \left(\frac{1}{2\pi} \int d^2\mathbf{k}_\perp \mathcal{U}_{\ell p}(\mathbf{k}_\perp) e^{i(\mathbf{k}_\perp \cdot \mathbf{r}_\perp)} \right) |\{0\}\rangle. \end{aligned} \quad (2.63)$$

In the above equation, we can clearly identify a two-dimensional Fourier transform operating on the k-space distribution of the LG modes, when comparing to the ASR transform at $z = 0$ in equation (2.12). Hence, we can write the quantum state in the form

$$|\Psi\rangle = \sum_{\sigma,\ell,p} \int_0^\infty dk_0 \int d^2\mathbf{r}_\perp f_{\sigma,\ell,p}(\mathbf{r}_\perp, k_0) \hat{a}_\sigma^\dagger(\mathbf{r}_\perp, k_0) |\{0\}\rangle, \quad (2.64)$$

where $f_{\sigma,\ell,p}(\mathbf{r}_\perp) = C_{\sigma,\ell,p}(k_0) \times u_{\ell p}(\mathbf{r}_\perp, z = 0)$ gives us one component of a type of two-dimensional wave function for our state ($u_{\ell p}$ is given in equation (2.5)).

The concepts presented above also have some general implications which highlight the direct connection between the modes of light in classical optics and the Fock space operators [113]. The first one is the commutation of the creation/annihilation operators of two arbitrary modes [119]

$$[\hat{b}_f, \hat{b}_g^\dagger] = \int \mathbf{f}(\mathbf{k}) \cdot \mathbf{g}^*(\mathbf{k}) d^3\mathbf{k}, \quad (2.65)$$

where \hat{b}_f is an annihilation operator for the mode with a normalized angular spectrum $\mathbf{f}(\mathbf{k})$ and \hat{b}_g^\dagger is a creation operator for a mode with the normalized angular spectrum $\mathbf{g}(\mathbf{k})$. The normalization means that the modes produce an overlap of one when integrated over the whole k-space

$$\int \mathbf{f}(\mathbf{k}) \cdot \mathbf{f}^*(\mathbf{k}) d^3\mathbf{k} = 1$$

The second example of this connection is seen in the inner product of single-photon Fock states. This inner product can be calculated from the commutation relation in equation (2.65)

$${}_f\langle 1|1\rangle_g = \langle\{0\}|\hat{b}_f\hat{b}_g^\dagger|\{0\}\rangle = \int \mathbf{f}(\mathbf{k}) \cdot \mathbf{g}^*(\mathbf{k}) d^3\mathbf{k}. \quad (2.66)$$

Thus far we have defined modes of the electromagnetic field both classically and quantum-mechanically. We also explored what sort of quantum states we could theoretically construct (both spatially and through their photon distribution). What is left then, before moving into describing experiments, is exploring some properties and use-cases of such quantum states of light and what physical

process can create such states of light.

2.3 Measurements, Unitary Evolution, and Mutually Unbiased Bases

In the previous sections, we have seen that paraxial light beams have a plethora of orthogonal modes which photons can occupy and learnt how to mathematically describe them. However, for the purposes of our experimental investigations, we should still know how the measurements and evolution of such quantum states are theoretically calculated. Hence, in this section, we will explore how we can theoretically describe these processes in addition to discussing the concept of mutually unbiased bases (MUBs) which is important when inducing quantum interference. Additionally, MUBs are an important concept in some technological applications. Lastly, we will briefly go over how these concepts come together in describing N00N states which we will be utilizing in the experimental section of this thesis. This section is mostly based on Audretsch's book [112] and Gerry's and Knight's book [93].

2.3.1 Measurements

When it comes to measurements, in quantum mechanics there are more general methods of theoretically describing measurements, such as a positive-operator-valued measure (POVM) [112]. For most of our purposes, however, Born's rule for pure quantum states is sufficient. Born's rule states that for some Hermitian operator \hat{Q} with eigenvalues λ_i , the probability of a normalized pure state $|\psi\rangle$ being in a specific eigenstate $|\lambda_i\rangle$ is

$$p(\lambda_i) = \langle\psi| P_i |\psi\rangle = \langle\psi| \lambda_i\rangle \langle\lambda_i| \psi\rangle = |\langle\lambda_i| \psi\rangle|^2, \quad (2.67)$$

where $P_i = |\lambda_i\rangle \langle\lambda_i|$ is a projection operator onto the state $|\lambda_i\rangle$. In other words, Born's rule gives us the projection of the quantum state in question onto a chosen quantum state.

Besides projecting onto specific states, it is sometimes instructive to model a measurement as probing the expected number of photons in the state $\langle\hat{n}\rangle$. For calculating the probability of two coinciding photodetections in detectors that measure counts in modes 1 and 2, an observable of the form $\langle\hat{a}_1^\dagger \hat{a}_2^\dagger \hat{a}_2 \hat{a}_1\rangle$

is often used [19, 120].

2.3.2 Mutually Unbiased Bases

A basis B is mutually unbiased in regard to another basis B' if for any basis state in basis B the projection onto a mode from basis B' is $|\langle\psi_b|\psi_{b'}\rangle|^2 = 1/d$ [121]. Here d is the dimension of the Hilbert space in question. Or phrased differently, measuring a basis state of B in the B' basis gives out a random result.

To give an example, we first limit ourselves to a two-dimensional Hilbert space, by focusing on a single photon and two modes. For photons, the modes that are usually chosen for two-level systems have orthogonal polarizations but are otherwise identical. Thus, we can denote our basis of two modes occupied by one photon as $\{|1\rangle_H, |1\rangle_V\}$. These two states can be used as polarization qubits, and they form the building blocks of different potential quantum technologies. One fitting example of such a technology is quantum key distribution (QKD) where single-photon qubits can be used to produce an unconditionally secure encryption key, at least theoretically [122]. The example is fitting since MUBs are often important in QKD, due to the objective randomness they add [123].

For any two-dimensional state space, such as the two polarization modes, there is always a set of 3 MUBs when including the chosen initial basis. For the basis $\{|1\rangle_H, |1\rangle_V\}$ these are the diagonal/anti-diagonal basis $\{|1\rangle_D, |1\rangle_A\}$ and left/right circular basis $\{|1\rangle_L, |1\rangle_R\}$. Identically to classical optics, these states can be given as superpositions in another basis

$$|1\rangle_D = \frac{1}{\sqrt{2}}(|1\rangle_H + |1\rangle_V), \quad |1\rangle_A = \frac{1}{\sqrt{2}}(|1\rangle_H - |1\rangle_V) \quad (2.68)$$

$$|1\rangle_L = \frac{1}{\sqrt{2}}(|1\rangle_H + i|1\rangle_V), \quad |1\rangle_R = \frac{1}{\sqrt{2}}(|1\rangle_H - i|1\rangle_V). \quad (2.69)$$

It is simple to see that these states form MUBs for $\{|1\rangle_H, |1\rangle_V\}$, producing $|\langle_b|1\rangle_{b'}|^2 = 1/2$ for any pair of bases. One visual way of representing these polarization MUBs is using the Poincaré sphere (figure 2.4a) or the more general version of it called the Bloch sphere, which can be used to represent any pure two-dimensional quantum state (see a spatial mode Bloch sphere in figure 2.4b). Mixed states can also be drawn in the same Bloch sphere picture, but they are

represented by so-called Bloch vectors which do not reach the surface of the sphere [112].

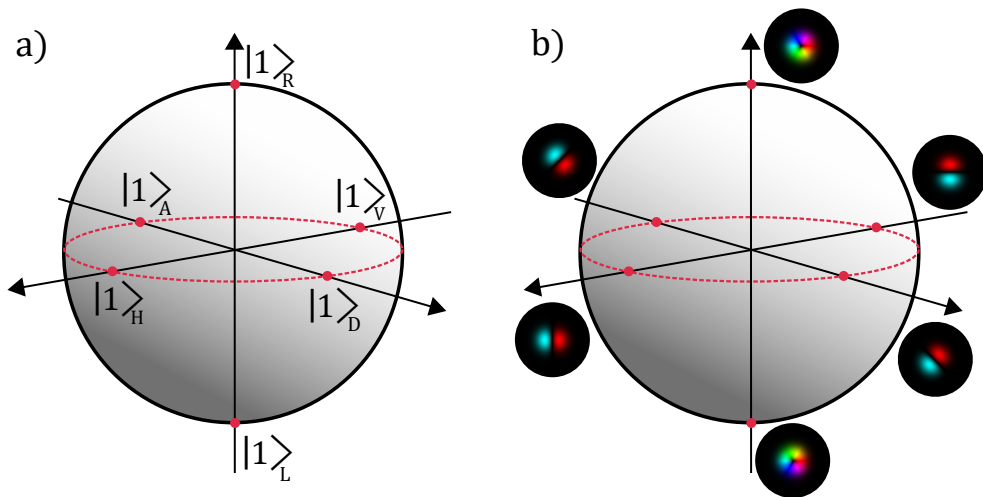


Figure 2.4 Drawings of, a) a Poincaré sphere and b) a Bloch sphere for a two-dimensional subset of LG modes with $p = 0$ and $\ell = \pm 1$. Each basis is composed of the two points on the unit sphere's surface, on opposite sides of the sphere. In both a) and b), a new MUB can be defined for one selected basis by rotating an axis with these basis states 90° in any direction. An arbitrary fully polarized state (a) or a pure quantum state (b) in this two-dimensional space can be stated using an azimuthal angle $\varphi = [0, 2\pi]$ and an elevation angle $\theta = [0, \pi]$ as $|\psi\rangle = \exp(-i\varphi/2) \cos(\theta/2) |1\rangle_i + \exp(i\varphi/2) \sin(\theta/2) |1\rangle_j$, where $\{|1\rangle_j, |1\rangle_i\}$ is a pair of orthogonal basis states chosen for the corresponding angles [112]. The Bloch sphere can also be used to visualize other effects such as measurements and unitary dynamics, more details of which can be found in reference [112].

For arbitrary Hilbert space dimensions, it has been shown that if the dimensionality of the space can be stated as a power of a prime number $d = \Pi^m$, $m \in \mathbb{N}$, we can construct the maximal number of $d + 1$ MUBs for this space [121]. However, although some MUBs can be constructed for other dimensions (e.g. $d = 6$) it is not known if a maximal set of MUBs can even be constructed for these dimensions. The construction of such bases is discussed in detail in reference [121] and, e.g., in the case where d is an odd prime we have the convenient formula for the k^{th} eigenstate of the j^{th} MUB

$$\left| \phi_k^{(j)} \right\rangle = \frac{1}{\sqrt{d}} \sum_{m=0}^{d-1} \omega_d^{-km} \omega_d^{jm(m-1)/2} |m\rangle. \quad (2.70)$$

In equation (2.70), $|m\rangle$ are the eigenstates in the computational basis forming the first MUB in the set, $\omega_d = \exp(i2\pi/d)$, and all of the indices count from 0 to $d - 1$.

2.3.3 Unitary Evolution

The final concept on our list, unitary operators, is a set of linear operators for our chosen Hilbert space. Unitary operators are also categorized as special normal operators [112]. Their defining feature is that their Hermitian conjugate corresponds to the inverse of the operator, i.e.,

$$\hat{U}\hat{U}^\dagger = \hat{U}^\dagger\hat{U} = \hat{I}, \quad (2.71)$$

when \hat{I} is the identity operator in the chosen Hilbert space. These operators are important for our experiments since any lossless linear optical system can be modelled as a unitary transformation acting on the finite set of modes we are working with, in our system [124, 125]. One especially important property of unitary operations is that they conserve the inner product

$$\langle\psi|\phi\rangle = \langle\psi|\hat{U}^\dagger\hat{U}|\phi\rangle = \langle\psi_U|\phi_U\rangle,$$

when $|\psi_U\rangle = \hat{U}|\psi\rangle$ and $|\phi_U\rangle = \hat{U}|\phi\rangle$. This means that photon-number-preserving linear optical systems preserve the orthogonality of states of light.

In the two-dimensional single-particle Hilbert space we worked in above, unitary operators can be stated in two equivalent forms. They can be written using the Dirac notation or equivalently, since Hilbert spaces are vector spaces, as a matrix. One example of such unitaries is a so-called beamsplitter unitary which sets either of two arbitrary modes 1 and 2 into a balanced superposition of the same pair of modes. One version of such a unitary can be written in the Dirac notation as

$$\hat{U}_{BS} = \frac{1}{\sqrt{2}}|1\rangle_{11}\langle 1| - \frac{i}{\sqrt{2}}|1\rangle_{12}\langle 1| - \frac{i}{\sqrt{2}}|1\rangle_{21}\langle 1| + \frac{1}{\sqrt{2}}|1\rangle_{22}\langle 1|. \quad (2.72)$$

When stating this transformation as a unitary matrix, the diagonal elements correspond to the coefficients of the $|1\rangle_i\langle 1|$ terms and off-diagonal elements

are the coefficients of the $|1\rangle_i \langle 1|_j$ terms

$$U_{BS} = \frac{1}{\sqrt{2}} \begin{bmatrix} 1 & -i \\ -i & 1 \end{bmatrix}. \quad (2.73)$$

Besides describing the operation of a beamsplitter, this unitary operator also gives us a MUB transformation. Hence, if we set $H = 1$ and $V = 2$, we can state $|1\rangle_R = \hat{U}_{BS} |1\rangle_H$ and $-i|1\rangle_L = \hat{U}_{BS} |1\rangle_V$. This leads us to a more general point; for any finite dimension, we can define a unitary matrix for each MUB of the computational basis [121].

Moving to transformations with multiple photons, we have to jump from a simple two-dimensional Hilbert space to the total Fock space. Although the states of the total Fock space can be described in a Hilbert space formalism [117], for our use cases, working with the Fock space is more convenient. As it turns out, for the purposes of this thesis, all of our transformations of the modes of light can be conveniently calculated by transforming the creation and annihilation operators. Meaning that, for a unitary evolution operator \hat{U} , we can calculate the resulting state by evolving the creation operators of all the relevant modes as

$$\hat{U}^\dagger \hat{a}_i^\dagger \hat{U}. \quad (2.74)$$

Furthermore, in finite-dimensional photon-number-preserving linear systems, the resulting transformation can be stated as a sum of orthogonal modes \hat{a}_j^\dagger , summed together using the unitary matrices we introduced for single-photon transformations [126]

$$\hat{a}_i^\dagger = \sum_j U_i^j \hat{a}_j^\dagger. \quad (2.75)$$

To use the two-mode beamsplitter as an example again, if we define

$$\hat{U}_{BS} = e^{i\frac{\pi}{4}(\hat{a}_1^\dagger \hat{a}_2 + \hat{a}_1 \hat{a}_2^\dagger)}$$

the evolution of the creation operators for modes 1 and 2 become

$$\hat{U}_{BS}^\dagger \hat{a}_1^\dagger \hat{U}_{BS} = \frac{1}{\sqrt{2}} (\hat{a}_1^\dagger - i \hat{a}_2^\dagger), \quad \hat{U}_{BS}^\dagger \hat{a}_2^\dagger \hat{U}_{BS} = \frac{1}{\sqrt{2}} (-i \hat{a}_1^\dagger + \hat{a}_2^\dagger), \quad (2.76)$$

which can be calculated with the Baker-Hausdorff lemma [115]

$$\begin{aligned}
e^{i\hat{G}\lambda}\hat{A}e^{-i\hat{G}\lambda} &= \hat{A} + i\lambda [\hat{G}, \hat{A}] + \frac{(i\lambda)^2}{2!} [\hat{G}, [\hat{G}, \hat{A}]] + \dots \\
&\dots + \frac{(i\lambda)^n}{n!} [\hat{G}, [\hat{G}, [\hat{G}, \dots [\hat{G}, \hat{A}] \dots]]] + \dots.
\end{aligned} \tag{2.77}$$

By comparing the forms of Eqs. (2.73) and (2.76), we can clearly see the link between the single-photon Hilbert space unitary matrix U_{BS} and the evolution of the corresponding creation operators.

2.3.4 N00N States

N00N states provide a relevant example where a combination of the concepts presented in this section is needed to theoretically describe them. N00N states are commonly used in the field of metrology where quantum features can improve the precision with which we can estimate a set of parameters when the number of photons is fixed. More about the details and advancements in the field of photonic quantum metrology can be found in references [118, 127–129].

The specific quantum-enhanced measurement technique we are interested in here utilizes the increased phase sensitivity of photon number states. This is an effect we will be utilizing in the experimental section of the thesis as well. Generally, in the context of N00N states, this phase sensitivity is useful in interferometric applications. N00N states get their name from the form of the state written in the Fock basis

$$|\Psi\rangle = \frac{1}{\sqrt{2}} (|N\rangle_1 |0\rangle_2 + |0\rangle_1 |N\rangle_2) \tag{2.78}$$

where our set of N photons are in a superposition of two orthogonal modes.

The increased phase sensitivity of Fock states is simple to derive using the relation we gave in equation (2.75). We just need a unitary evolution of the two modes where they acquire different phases. The most common example is a seemingly normal interferometer where the two modes correspond to two Gaussian beams travelling along different paths, as displayed in figure 2.5. we can then, for example, assume that the phase difference is acquired through a slightly different path length in the interferometer, allowing us to construct a

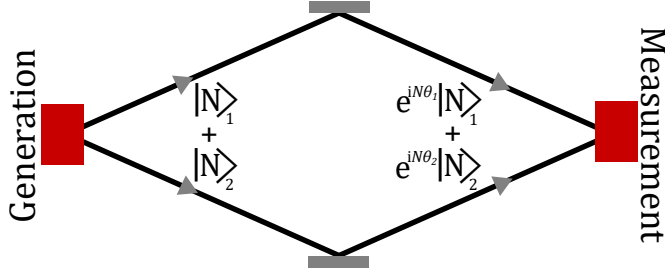


Figure 2.5 Conceptual drawing showing a N00N state between two photon paths. The drawing shows the phase accrued by the two states during propagation between generation and measurement.

unitary matrix

$$U_p = \begin{bmatrix} e^{i\theta_1} & 0 \\ 0 & e^{i\theta_2} \end{bmatrix}. \quad (2.79)$$

which describes the situation² with any arbitrary pair of phases θ_1 and θ_2 . As in equation (2.75), we can now construct a new pair of creation operators after the propagation $\hat{a}_1^\dagger \rightarrow e^{i\theta_1}\hat{a}_1^\dagger$ and $\hat{a}_2^\dagger \rightarrow e^{i\theta_2}\hat{a}_2^\dagger$.

With the evolution of the creation operator, we can write the N00N state after propagation as

$$\begin{aligned} & \frac{1}{\sqrt{2}} \left(\frac{1}{\sqrt{N!}} (\hat{a}_1^\dagger)^N + \frac{1}{\sqrt{N!}} (\hat{a}_2^\dagger)^N \right) |\{0\}\rangle \\ \rightarrow & \frac{1}{\sqrt{2}} \left(\frac{1}{\sqrt{N!}} (e^{i\theta_1}\hat{a}_1^\dagger)^N + \frac{1}{\sqrt{N!}} (e^{i\theta_2}\hat{a}_2^\dagger)^N \right) |\{0\}\rangle \\ = & \frac{1}{\sqrt{2}} e^{iN\theta_1} \left(|N\rangle_1 |0\rangle_2 + e^{iN(\theta_2-\theta_1)} |0\rangle_1 |N\rangle_2 \right), \end{aligned} \quad (2.80)$$

where we now have a photon-number-dependent phase shift. One optimal measurement for getting the most amount of information about the phase difference $\Delta\theta = \theta_2 - \theta_1$, is by using the observable $\hat{A} = |0\rangle_1 |N\rangle_2 \langle N|_2 \langle 0|_1 + |N\rangle_1 |0\rangle_2 \langle 0|_2 \langle N|_1$. The expectation value of this observable gives us

$$\langle \hat{A} \rangle = \cos(N\Delta\theta) \quad (2.81)$$

²We should keep in mind that although translating along the optical axis of a paraxial mode is a unitary process, it is not solely a constant phase shift, as will be discussed in detail in chapter 6. For the purposes of this example however, this approximation is sufficient.

where we clearly see that the signal has N times the fringes in comparison to a regular interferometer using classical light, where the signal is proportional to $\cos(\Delta\theta)$.

Although this derivation tells us about the basic principle behind quantum-enhanced N00N state interferometers, it is still missing a few key details such as, how to justify the usefulness of N00N states and how one determines if a measurement is optimal. These justifications will be explored in chapter 5 where we will combine the properties of N00N states with transverse spatial modes.

2.4 Nonlinear Optics

The final piece of theoretical background we are currently missing is a brief look into nonlinear optical phenomena. This is required since the source of photons used in this thesis work is based on a nonlinear optical effect called spontaneous parametric downconversion (SPDC). However, although this source of photons plays an important part in our experiments, the operation of similar sources has been described in a myriad of different publications and a lot of research has been done on optimizing different types of downconversion sources (see e.g. references [130–139]). Therefore, we will only briefly introduce some of the most important basic concepts relevant to building a photon pair source. For a more in-depth description of nonlinear optics, one should look into books such as Boyd’s [95].

2.4.1 Classical Three-Wave Mixing

Nonlinear optics is a sub-field of optics that studies light interacting with media that have a nonlinear response to applied optical fields. Classically the effects of nonlinear optics can be again calculated from Maxwell’s equations but, as we are no longer in free space, one needs to take into account the material polarization $\tilde{\mathbf{P}}$ which we ignored in the earlier sections. This is usually done while still assuming no free currents or charges in a nonmagnetic medium, and switching to the macroscopic Maxwell’s equations with the electric displacement field $\tilde{\mathbf{D}} = \epsilon_0\tilde{\mathbf{E}} + \tilde{\mathbf{P}}$ [95, 140]. The usual equation written to describe the nonlinear response in the material polarization (or dipole moment per unit volume) is

[95, 133, 140]

$$\tilde{P}_i(t) = \epsilon_0 \left[\sum_j \chi_{ij}^{(1)} \tilde{E}_j(t) + \sum_{j,k} \chi_{ijk}^{(2)} \tilde{E}_j(t) \tilde{E}_k(t) + \sum_{j,k,l} \chi_{ijkl}^{(3)} \tilde{E}_j(t) \tilde{E}_k(t) \tilde{E}_l(t) + \dots \right] \quad (2.82)$$

where $\chi^{(1)}$ is the linear susceptibility of the material, $\chi^{(n)}$, ($n > 1$) are its non-linear susceptibilities which are $(n + 1)$ -rank tensors, and $\{i, j, k\}$ denote the Cartesian components of the fields. In this form of the equation, the response of the medium is assumed to be instantaneous. These assumptions imply that the medium is assumed lossless and dispersionless [95], which is not true in general. Here we will only be utilizing the second term of this equation, which can be written in a more general form by first following the definitions of Boyd [95]; $\tilde{\mathbf{P}}(\mathbf{r}, t) = \sum_n \mathbf{P}(\mathbf{r}; \omega_n) \exp(-i\omega_n t)$ and $\tilde{\mathbf{E}}(\mathbf{r}, t) = \sum_n \mathbf{E}(\mathbf{r}; \omega_n) \exp(-i\omega_n t)$, where the summation extends over a discrete set of all possible frequencies, including negative frequency components as well to accommodate for the complex conjugate terms. Due to the negative frequency components, we define $\mathbf{E}(\mathbf{r}; -\omega_n) = \mathbf{E}^*(\mathbf{r}; \omega_n)$. With these definitions, we can write the more general form of the second-order nonlinearities as

$$P_i^{(2)}(\omega_n + \omega_m) = \epsilon_0 \sum_{j,k} \sum_{(nm)} \chi_{i,j,k}^{(2)}(\omega_n + \omega_m; \omega_n, \omega_m) E_j(\omega_n) E_k(\omega_m), \quad (2.83)$$

where $\chi_{i,j,k}^{(2)}(\omega_n + \omega_m, \omega_n, \omega_m)$ are the relevant components of the second order susceptibility tensor and the summation $\sum_{(nm)}$ is performed so that the sum $\omega_n + \omega_m$ is held fixed. The above equation describes a set of interactions categorized as second-order nonlinear interactions or, alternatively, three-wave mixing. The name “three-wave mixing” is given to the process due to the fact that, in contrast to the linear material polarization, the nonlinear response of material polarization can act as a source emitting light in a mode where the initial light fields were not oscillating in, adding a third light wave to the interaction.

The reason why the observed material response to light is usually linear is

due to how small the nonlinear susceptibilities are in comparison to the linear ones. Hence, laser light is usually used when inducing nonlinear responses. Additionally, the second-order nonlinear processes only occur in noncentrosymmetric crystals, i.e., crystals that do not exhibit inversion symmetry.

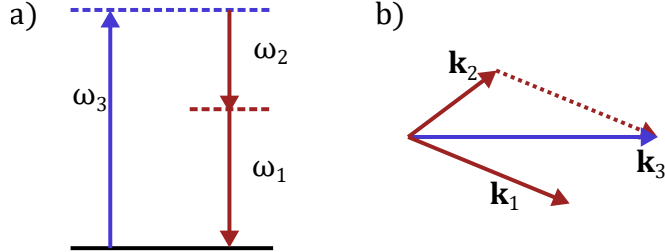


Figure 2.6 Figure denoting a) the energy-level diagram of the SPDC process with dashed lines corresponding to virtual energy levels and b) the phase-matching condition for efficient down-conversion. The red arrows correspond to the pair of downconverted photons (1 and 2) with a smaller energy compared to the pump photon (3).

The process we are interested in – SPDC – is a three-wave mixing process since it involves one intense pump field with frequency ω_3 creating two fields with lower energy ω_1 and ω_2 . Since the process is parametric (the crystal’s quantum mechanical state is left unaltered after the process) the photon energy needs to be conserved. The energy level diagram in figure 2.6 a) is often used to describe the process. The diagram uses virtual energy levels, and the energy conservation follows the equation

$$\hbar\omega_3 = \hbar\omega_1 + \hbar\omega_2. \quad (2.84)$$

The process is also most efficient for the case of perfect phase matching [133, 140] (see figure 2.6b)

$$\Delta\mathbf{k} \equiv \mathbf{k}_3 - \mathbf{k}_2 - \mathbf{k}_1 = \mathbf{0}, \quad (2.85)$$

where $\mathbf{0}$ is a zero vector. This condition can be interpreted as momentum conservation or as a condition for the energy from one optical field to couple efficiently to another optical field by keeping both fields in phase as they travel through the crystal. Commonly for birefringent crystals, this is achieved by selecting a combination of polarization directions in the crystal so that the phase-matching condition is fulfilled [95]. However, it is also possible to achieve phase matching, in the wanted propagation directions, through a process called

quasi-phase-matching (QPM) [95, 141] which we will be utilizing in this thesis.

The details of quasi-phase-matching can be read in publications such as reference [141], but in short, QPM reduces the effects of imperfect phase matching by periodically inverting the orientation of one of the crystalline axes [95]. This is done to induce periodical flips in the sign of the nonlinear coupling coefficient between the driving field(s) and the material polarization. If the periodicity of the inversion is equal to the propagation distance after which the energy would begin to flow out of the generated field(s), the inversion effectively corrects for the phase mismatch and allows more of the field energy to flow into the wanted mode(s). Effectively, we can state this as an additional component in the phase-matching equation [95, 137, 141]

$$\Delta k_Q = k_3 - k_2 - k_1 - \frac{2\pi}{\Lambda}, \quad (2.86)$$

where $\Lambda/2$ corresponds to the domain length after which the crystalline axis is inverted, and we have restricted ourselves to the case of collinear phase matching for simplicity. Although QPM can produce good efficiencies in nonlinear processes, it should still be noted that if perfect phase matching is possible, it would produce a stronger nonlinear effect, provided that all the other variables are kept the same [95, 141].

2.4.2 Quantum Description of Spontaneous Parametric Downconversion

Although most effects in nonlinear optics are sufficiently well described by a classical treatment, a full description of SPDC light needs a quantum formalism. The SPDC process can be described by its effective interaction Hamiltonian, which is of the form [93, 140]

$$\hat{H}_I \sim \chi^{(2)} \hat{a}_3 \hat{a}_1^\dagger \hat{a}_2^\dagger + H.c., \quad (2.87)$$

where $\chi^{(2)}$ is the relevant nonlinear susceptibility and the indices 1 and 2 correspond to the modes of the downconverted photons while 3 denotes the pump field. It can be seen from the operators shown in the equation how the SPDC process corresponds to one pump photon being subtracted to create two photons in modes 1 and 2.

Using a more complete form of the interaction Hamiltonian, the quantum state resulting from SPDC can be calculated under many different conditions and approximations. For our purposes, the state reported by Lerch et al. [137] is close to the scenario utilized in our experimental setup. In reference [137], the authors calculate the output for a QPM type-0 configuration, which means that the polarization of the pump and the two downconverted photons are the same. Hence, QPM is needed in the process since the birefringence of the material cannot be used to achieve phase matching. Furthermore, the authors assume a non-depleting monochromatic pump with a transverse field distribution $\mathcal{E}_3^+(\mathbf{k}_\perp)$ propagating along the z -direction. The frequencies of the downconverted photons follow the energy conservation in equation (2.84) and the nonlinear crystal has a temperature-dependent length $L(T)$. The approximate unnormalized state for the modes 1 and 2 was then calculated, using perturbation theory [133], to be of the form [137]

$$|\Psi\rangle = |\{0\}\rangle + \int d\mathbf{k}_{\perp,1} \int d\mathbf{k}_{\perp,2} \int d\omega_2 s(\mathbf{k}_{\perp,1}, \omega_3 - \omega_2, \mathbf{k}_{\perp,2}, \omega_2) \quad (2.88)$$

$$\times \hat{a}_1^\dagger(\mathbf{k}_{\perp,1}, \omega_3 - \omega_2) \hat{a}_2^\dagger(\mathbf{k}_{\perp,2}, \omega_2) |\{0\}\rangle, \quad (2.89)$$

where

$$s(\mathbf{k}_{\perp,1}, \omega_1, \mathbf{k}_{\perp,2}, \omega_2) = -\frac{2i\epsilon_0\chi_{eff}^{(2)}L(T)e(\omega_1)e(\omega_2)}{3\hbar(2\pi)^5n(\omega_1, T)n(\omega_2, T)} \quad (2.90)$$

$$\times \mathcal{E}_3^+(\mathbf{k}_{\perp,1} + \mathbf{k}_{\perp,2}) \text{sinc} \left[\frac{\left(\Delta k_z + \frac{2\pi}{\Lambda(T)} \right) L(T)}{2} \right]. \quad (2.91)$$

In the above equations, $n(\omega_j, T)$ denote the material refractive indices, $\Lambda(T)$ is the poling period of the crystal, $e(\omega_j) = i\sqrt{\frac{\hbar\omega_j}{2(2\pi)^3\epsilon_0c}}$ is a normalization function, and the phase mismatch term

$$\Delta k_z = \sqrt{\left(\frac{\omega_1}{c}n(\omega_1, T)\right)^2 - \mathbf{k}_{\perp,1}^2} + \sqrt{\left(\frac{\omega_2}{c}n(\omega_2, T)\right)^2 - \mathbf{k}_{\perp,2}^2} \quad (2.92)$$

$$- \sqrt{\left(\frac{\omega_3}{c}n(\omega_3, T)\right)^2 - (\mathbf{k}_{\perp,1} + \mathbf{k}_{\perp,2})^2}. \quad (2.93)$$

One key thing to note about equation (2.88) is that although the equation

only has a vacuum term and a two-photon term, the perturbation theory solution ignores higher-order terms such as $C_2 |2\rangle_1 |2\rangle_2$ which generally have a much smaller amplitude. Despite being an approximation, the equation does give us some intuition on how to maximize the probability of photon pair generation. Of course, this maximization should be done while keeping in mind that with a very large downconversion efficiency, the higher-order terms start to become non-negligible. From $s(\mathbf{k}_{\perp,1}, \omega_1, \mathbf{k}_{\perp,2}, \omega_2)$, it is quite clear that the main contributors to the amplitude of the two-photon state are the amplitude of the pump field, the length of the crystal, the magnitude of the nonlinear susceptibility, and the phase matching term $\Delta k_z + \frac{2\pi}{\Lambda(T)}$. In a not-so-direct way, the shape of the pump also affects the shape of the downconverted state which then affects the number of collected photon pairs. This is caused by the spatiotemporal filtering that almost always occurs when the two photons are collected in an experimental system [131, 138].

3 CREATION AND TRANSVERSE SPATIAL MANIPULATION OF PHOTONS

With the theoretical background presented in the previous chapter, we are well-equipped to start describing the experimental methods and devices that are utilized in this thesis work. We can roughly separate our experimental setups into four distinct stages, photon pair generation, transverse structuring of photons, measuring photon transverse structures, and finally photon pair detection. As it is crucial to have a source of photons to study two-photon interference effects, we will start by utilizing the SPDC described in section 2.4 to construct a photon pair source. We will then go through some of the devices and post-processing required to measure such two-photon states of light. The rest of this chapter will be spent detailing the devices and methods utilized in shaping and measuring the transverse structures of these photons.

3.1 Photon Pair Source

In order to reliably study the quantum interference of multiple photons, we need to have a source of photon number states, i.e., the Fock states described in 2.2.1.1. Since, as we shall see in the following chapters, the quantum interference effects we aim to observe require a source capable of producing photon number states. Although attenuating laser light produces a beam of light which transmits one photon at a time on average, such states of light are more accurately described by the coherent state (see section 2.2.1.2). Fortunately, in section 2.4 we saw how the second-order nonlinear process of SPDC is capable of producing photon number states.

SPDC has been used as a source in many quantum interference experiments including the seminal experimental work of Hong, Ou, and Mandel [19]. The process is also very versatile since it can be used in many different scenarios.

For example, the photon pair generated in this process can be used as a source of single photons by heralding the existence of one photon by detecting its partner [142]. In section 2.4 we listed a plethora of articles looking into the optimization and theory of SPDC sources in different tasks. Although we will describe in detail the photon pair source used in the experiments presented within this thesis, readers aiming to build an optimal photon pair source can get a better overview of optimal parameters from such publications (e.g. [130–139]).

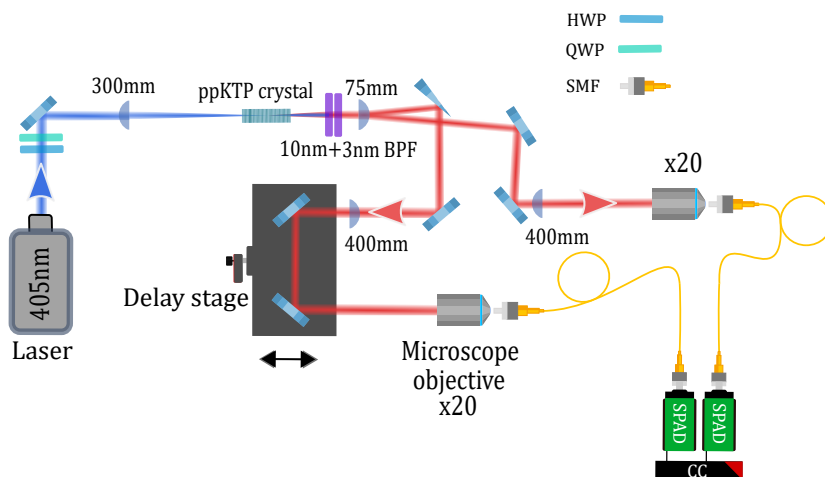


Figure 3.1 Drawing of the SPDC source used in the experiments described in this thesis. The drawing shows the focal lengths of the lenses used and displays the general structure of the source. For a detailed description of the construction of the source, see the main text. In all the experiments presented here, the photons are detected using single-photon avalanche diodes (SPADs) and coincidence counters (CC), as is shown in the bottom right corner and explained in detail in section 3.2. The figure is adapted from the supplementary of **publication III** [143].

A diagram detailing the construction of our photon pair source is shown in figure 3.1. The source uses a continuous-wave pump laser centred around 405 nm (spectral line width <0.06 nm and free-space output power of roughly 135 mW), the output of which is focused into a 12 mm long quasi-phase-matched potassium titanyl phosphate crystal. Due to the QPM, such a nonlinear crystal is often called a periodically poled potassium titanyl phosphate (ppKTP) crystal. The crystal is coated by the manufacturer to increase transmittance at the pump wavelength and the downconverted wavelength (810 nm). The poling period of the crystal, as stated by the manufacturer, is $3.425 \mu\text{m}$. As hinted at

in section 2.4, the crystal is phase matched for type-0 phase matching. Hence, a half-wave plate (HWP) and a quarter-wave plate (QWP) are placed before the crystal to orient the polarization of the pump in the correct direction.

It should be noted that although the same source is used in all three of the experiments presented in the thesis, some details vary between experiments. Most significantly, the first experiment (**publication I**) used a fibre-coupled version of the same pump laser, with the pump power varying between 40 mW and 70 mW due to degradation over time. The latter two experiments used the free-space laser described previously. When using the free-space laser, the pump field was focused into the crystal with a 300 mm focal length lens. This gives the pump beam a slightly astigmatic focus with a waist radius of 67 μm , measured at the crystal position in free space.

The phase matching is controlled through the temperature of the crystal using an oven that actively controls the temperature of the crystal. The crystal temperature is tuned to maximize the rate of collected photon pairs, giving both photons of each pair a spectrum centred at 810 nm. As studied in detail in reference [137], the temperature dependence of our SPDC source is caused by the thermal dependence of the refractive index and thermal expansion of the crystal which changes the crystal length and poling period. Out of these three effects, they attribute most of the change in phase matching to the temperature dependence of the refractive index. After the crystal, the pump laser is filtered out with band-pass filter(s) (BPFs) which also narrow down the bandwidth of the downconverted photons. The narrowest filter had a 10 nm bandwidth in the first experiment (**publication I**) and a 3 nm bandwidth in the two later experiments (**publications II** and **III**).

After the pump is filtered from the downconverted pair of photons, we still needed to separate the pair of photons and collect them. Since the downconverted photons have the same polarization in type-0 downconversion, we cannot use polarization-dependent effects to separate them. Instead, we use the intrinsic momentum anticorrelations of the photons which exist in phase matched SPDC (see section 2.4). To do this, we first place a lens one focal length away from the crystal to gain access to the Fourier plane of the downconverted field through an optical Fourier transform (see e.g. reference [91] for information on optical Fourier transform). In the Fourier plane of the crystal, the momen-

tum anti-correlations of the photons have turned into a spatial separation of the photons. We can then split the two photons by placing a D-shaped mirror in the middle of the downconverted field, reflecting only one photon of the generated pair into a separate path. It is important to keep in mind that as the photons do have a non-negligible transverse extent, it is possible to split a single photon into a superposition of the two paths using the D-shaped mirror. In such a scenario, one can observe single-photon interference if the separated fields are brought together again. To avoid this, we found it best to have the degenerate downconversion be slightly non-collinear, which gives the filtered downconverted field a doughnut-like shape at the D-shaped mirror. We then collected two furthestmost regions of the doughnut, which successfully removed the single-photon interference from our signal.

To collect each photon, we use a lens and a 20x magnification microscope objective in each collection arm to couple the photons into separate single-mode fibres (SMF). The SMFs are placed on coupling stages that can be used to control the position of the fibre along three axes. Additionally, a computer-controlled delay stage is placed in one of the arms to allow control over the difference between the arrival times of the two photons in the experiments. The delay stage was controlled by the Thorlabs ZST225B actuator.

3.2 Photon Pair Detection

To detect photon pairs there are different types of devices one can use. Besides the capability of detecting a single photon, photon pair detection usually also require the ability to discern the detection time with sufficient accuracy or a short enough gating for the detection window of the photon. Nowadays there are many devices able to do this, such as superconducting nanowire detectors [144] or intensified charge-coupled devices [145], to name a few. The detectors we used in our experiments were SPADs, specifically the COUNT-T modules manufactured by laser components. These detectors have good timing precision (characterized by a timing jitter that the manufacturer states is around 500 ps at 670 nm and 100 000 counts per second), a low dark count rate (~ 20 counts per second), quantum efficiency of $\sim 74\%$ at 810 nm and a dead time of ~ 42 ns, according to the test data from the manufacturer.

Since our experiments always involved looking at coinciding detections in two of the aforementioned SPADs, we also needed a device for distinguishing when the two detectors registered a photon at the same time. To do this, we used a coincidence counter made by IDQuantique (ID900). Using 13 ps wide time-bins, this counter is able to discern the time difference between the detection events in our two detectors. Hence, with this device, we were able to calculate the total count rates of both of our detectors, while also counting how many times the two detectors registered a detection event at the same time.

In addition to choosing a suitable pair of detectors and a coincidence counting device, we still need to consider a few details about coincidence counting before we are able to move on to performing the experiments. Namely, we should consider the coincidence window, the rate of accidental coincident detections, and the nonlinearity of the detectors. The first of these – the coincidence window – is the window of time within which we consider the two detections to be simultaneous. This is important due to the spread in the timing of the detection events caused by properties such as the timing jitter of the detectors. Thus, we would like to make the coincidence window wide enough to include most of these coinciding detections. In all of our experiments, the coincidence window was set to 1 ns in the coincidence counter.

In some cases, however, the second point on our list – accidental coincident detections – might limit the width of our coincidence window. Accidental coincidences appear when uncorrelated detection events randomly coincide. Hence, for most quantum optical experiments, such events are inevitable due to detector dark counts and uncorrelated photons arriving at the detectors. Fortunately, we can remove accidental coincidences from our signal by calculating the expected number of such erroneous detections. In this thesis work, the accidental rates were calculated with the commonly used accidental rate calculation [146–148]

$$R_{acc} = R_1 R_2 \tau_c, \quad (3.1)$$

where R_i is the rate of single events in detector i per second and τ_c is the used coincidence window, giving us the rate of accidental coincidences per second. This equation also shows us that the rate of accidental detections can be minimized by shortening the coincidence window or by reducing the rate of uncorrelated detection events. Although this formula for accidental coincidences

is often sufficient, it is still an approximation and might not be reliable in all situations [149].

The final consideration on our list – detector nonlinearity – is caused by the dead time of the detectors. The dead time is the length of time after a detection event, during which the detector is unable to detect a photon. Thus, the dead time causes detector nonlinearity since a larger portion of photons go undetected when the rate of photons arriving at the detector is increased. This is due to a larger number of photons arriving at the detector during this dead time. In our measurements, the nonlinearity only affected our results when we wanted to estimate the rate of single photons and photon pairs our source was producing. In this case, the true photon rate arriving at our SPADs (when ignoring detector efficiencies) can be calculated from the rate of registered events R_{meas} using the equation [150, 151]

$$R_{\text{actual}} = \frac{R_{\text{meas}}}{1 - R_{\text{meas}}T_{\text{D}}}, \quad (3.2)$$

where T_{D} is the detector dead time.

3.3 Liquid Crystal Spatial Light Modulators

The last set of methods we require for our experiments involve the spatial structuring of light. The methods for performing spatial structuring utilize planes where the transverse field of the photons is manipulated. Hence, before we can move on to describing such methods in sections 3.4 and 3.5, we first need a device capable of modulating the transverse structure of a light field.

Computer-controlled devices capable of shaping the amplitude and/or phase of a light field at a specific plane are generally called spatial light modulators (SLMs). The modulation can happen either in transmission through the device or upon reflection from the device. The term SLM includes devices such as deformable mirrors, digital micromirror devices, and liquid-crystal (LC) screens [152]. In this thesis, we will be working with a specific type of LC SLM that can only modulate the transverse phase structure of a light field. We will briefly mention the operating principles of LC SLMs and go over the relevant details we needed to consider when using such SLMs. A more in-depth description of

the inner workings, and more details about the usage of such devices, can be found in references [147, 153, 154].

All of the SLMs used in the published works discussed in this thesis, were Holoeye Pluto-2 LC on silicon SLMs. These SLMs work in reflection and can only imprint a two-dimensional phase pattern onto the reflected light field. In a simplified picture, these SLMs consist of a layer of LCs which introduce the wanted phase delay onto a horizontally polarized light field through their intrinsic birefringence. To enable spatial control of this phase delay, the LC layer is sandwiched between pairs of electrodes. This arrangement enables a controllable rotation of the LCs at individual pixels which are only a few micrometres in size. The rotation of the LCs changes the phase delay applied at that pixel [153], effectively creating a phase difference between parts of the light field propagating through the LC layer at different positions of the device. Due to their birefringent nature, such SLMs are designed to operate only for one linear polarization. The Pluto-2 SLMs have a pixel pitch of $8\ \mu\text{m}$, a fill factor around 93 %, 1920 by 1080 pixels, and an active area of 15.36 mm by 8.64 mm.

In addition to the discrete size of the phase-modulating pixels, the phase-modulation levels of the SLM are also discretized. They are controlled by giving each pixel an 8-bit grey value, and hence at each pixel, we can induce one of 256 different phase delays. Although some SLMs can induce phase differences between pixels that are larger than 2π , we use the 8-bit values from 0 to 255 to impart phase differences between 0 and 2π . We chose the 2π difference because this gives us the maximum amount of phase delay levels for creating ramping phase structures between 0 and 2π . One such structure can be seen in figure 3.2 b) which shows a phase mask implementing a blazed grating on an SLM.

When using an SLM, there are many details and settings that can affect the end result. Chief among these is the possibility that the SLM imposes incorrect phase delays onto the light field or that these phase delays are inconsistent throughout the screen. Thus, we first verify that the different phases imprinted by the 8-bit values from 0 to 255 increase the phase of the field linearly from 0 to 2π . This verification can be done through a variety of different methods where usually one-half of a coherent light field is delayed by each of the 256

values and this phase difference is then recorded. The process can be done, for example, through off-axis digital holography [155–157], by coupling the field to an SMF, or focusing the field down to a camera as is shown in the setup in figure 3.2 c). Here we utilized the last one of these methods, the details of which are given in reference [147], and briefly mentioned in figure 3.2.

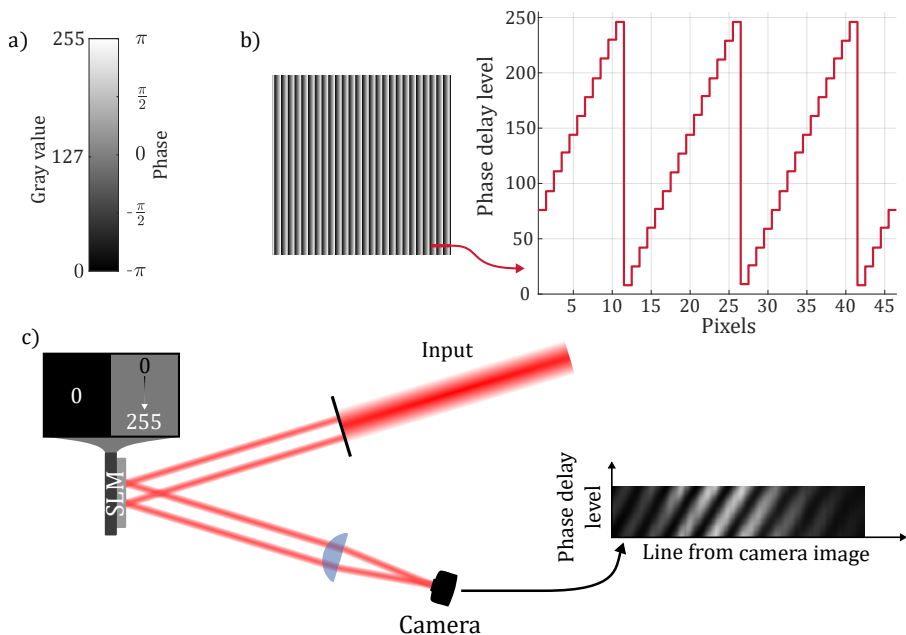


Figure 3.2 Figures related to SLM phase levels. a) is a colour map showing how the 0 to 255 grey levels correspond to the phase values from $-\pi$ to π . This colour map is also used in all images of phase masks in this thesis. b) contains an image of a blazed grating phase mask with each ramp of the structure having 15 pixels, a plot of the corresponding discrete phase levels is also shown. c) contains a drawing of the calibration setup used to calibrate the SLMs in this thesis work. The setup involves a laser beam that is divided into two beams that are directed onto two sections of the SLM. One of the beams is then successively delayed by different phase delay values, in respect to the other beam. The beams are then brought to interfere on a camera using a lens. A line from the interference pattern is then recorded on the camera for each delay value, which can be repeated multiple times to average out phase flicker effects. The images are subsequently used to calibrate the device according to the method in [147] until the stack of line images produces a linear phase delay for the applied delay values on a range of $[0, 2\pi]$. One example of this final stack of line images is shown on the right side of c).

One important thing to note is that, with any phase calibration method, the applied phase shifts vary for different incidence angles. Hence, calibration of the phase response of the SLM is ideally done when it has already been placed

into the experimental system.

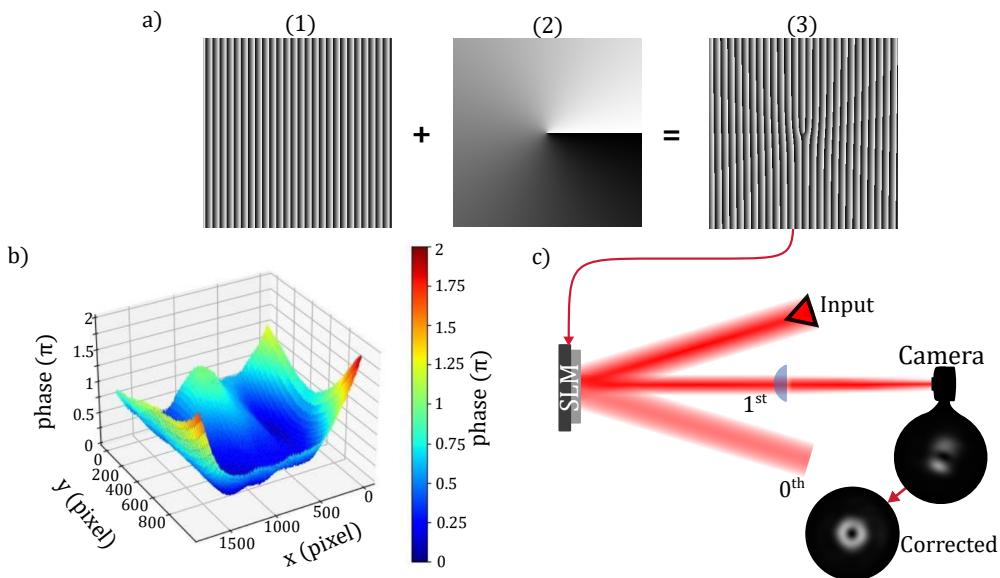


Figure 3.3 In a) we see a picturesque way of showing how one can calculate a phase mask imprinting OAM=+1 on the 1st diffraction order using (1) a blazed grating and (2) an azimuthal phase ramp (such masks are explained in more detail in section 3.4. b) shows an example of a phase aberration imprinted on a light field due to, e.g., the backplane of an SLM not being flat [154]. The plot in b) is adapted from reference [154], and it shows the flatness of a Pluto 2.1 SLM which has a particularly bad wavefront distortion, according to the manufacturer. c) shows a setup one can use to correct for the flatness of an SLM using an input beam hitting the mask shown in a) and optically Fourier transforming it onto a camera [158]. Next to the setup are example camera images we measured of an uncorrected and a corrected Fourier transform of an OAM=+1 structure. Note that the separation of the 0th and 1st diffraction orders is exaggerated here for clarity and the picturesque calculation of the phase mask is a simplification of the procedure.

Even with a phase calibrated SLM however, the phase delays at different areas of the SLM might not behave identically. Such behaviour could be caused by the backplane of the device not being flat due to the fabrication process [154]. Hence, even when the screen is supposed to set the same phase delay at each pixel, it might actually imprint a spatially varying phase structure. One example of an uncorrected wavefront reflected from a Pluto-2 SLM is shown in figure 3.3 b). To compensate for these phase variations, one can again use different methods (see for example [154, 158, 159]). For the first experiment presented here (**publication I**), we did not compensate for the unevenness of the SLM phases. In **publications II** and **III** however, we used

the method introduced in reference [158] to flatten the phase response of all SLMs. The basic idea behind this correction method involves imprinting OAM onto a beam of light using the SLM, with a phase mask similar to the one shown in figure 3.3 a). The beam is then optically Fourier-transformed and recorded with a camera. Figure 3.3 c) displays a diagram of this correction setup. The Gerchberg-Saxton algorithm [160] is adapted to reconstruct the corrective phase structure from the recorded images. After several iterations, the process leaves us with a phase-correction mask for a specific area of the SLM.

Besides the aforementioned details, there are other factors that might affect the operation of the SLM, such as the phase stability of the screen [147, 153, 154]. In addition to the effects listed in these references, we observed other effects that seemed to influence the behaviour of the SLMs. However, we did not investigate these effects in detail due to a limited time frame. First among these effects is a seemingly thermal effect affecting the alignment of optical setups with multiple reflections off of SLMs. When working with a setup with 5 reflections off of Holoeye Pluto-2 SLMs, we observed a slow decoupling of the system when switching from an alignment laser to a photon pair source. This decoupling was less severe when only using two reflections off the SLMs, and reducing the power of the alignment laser seemed to reduce this effect. The second effect was a polarization rotation we observed when using specific incidence angles and phase delay values on the SLM. This effect was observed when reflecting multiple times off of an LC SLM, manufactured by Meadowlark Optics, at a relatively small incidence angle. In this system, by only adding a uniform phase delay value on the SLM, the intensity of the beam after a polarizer was reduced significantly. One possible explanation of this effect could be that the birefringence of the LC produces a rotated polarization state instead of matching the output polarization to the polarization of the input field, at this specific incidence direction. One final effect we observed, in the same multi-reflection system with a Meadowlark SLM, was a slight lateral shift in the light beam when a spatially uniform phase shift was applied to the whole beam at one plane. This effect could cause small errors when complex manipulations of the spatial structure are performed. As for the cause of this effect, we do not currently have a satisfactory hypothesis.

3.4 Single Mask Spatial Mode Manipulation

Now that we have a device for structuring light, we can explore methods for using the phase-only SLMs to structure and measure the transverse field of our photons. We group these methods into ones utilizing a single phase mask, outlined in this section, and methods using multiple phase masks, also called multi-plane light conversion (MPLC) methods, which we will outline in section 3.5.

3.4.1 Spatial Structuring

With phase-only SLMs, the simplest form of spatial structuring is imprinting a phase structure on the beam. Such a method is straightforward but can cause the amplitude structure to evolve in a complex manner if proper imaging is not implemented. In the case of LG modes, this method is often used when dealing with pure OAM modes (i.e. modes where we do not care about the radial structure of the field). Due to the imperfect modulation efficiency of SLMs, caused by properties such as the non-unit fill factor and crosstalk between adjacent pixels, a blazed grating is often added onto these phase masks. This allows one to separate the light with the wanted phase modulation into the first diffraction order of the mask. The modulated light can then be separated from the rest of the field through filtering in the Fourier plane or far field of the phase mask. In all experiments presented in this thesis, such a grating was added to the hologram displayed on the SLM. However, not all applications and devices require this added grating term.

Phase mask patterns with a phase structure and an added grating were already used for creating OAM light fields already in the 1990s [161–164], and in single-photon experiments around the turn of the current century [165]. Computationally, one can create such a mask by simply summing up the phase profile one wants to imprint onto the beam with the phase profile of the blazed grating, as is also shown in figure 3.3 a). After summing up the phases, we still need to bring the resulting phase structure to a 2π range for the SLM with a modulo operation. Figure 3.4 displays a simplified rendered image of an incoming Gaussian beam on which an OAM is imprinted in the first diffraction

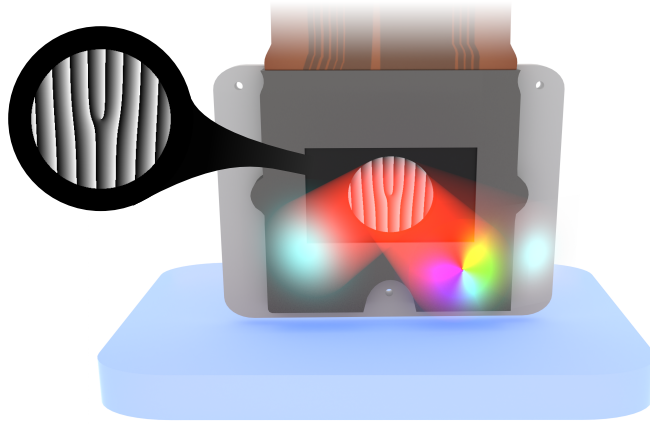


Figure 3.4 A render of an SLM imprinting +1 OAM onto a Gaussian beam. The input beam comes from the left and the wanted phase structure is imprinted onto the first diffraction order, shown on the right side of the input beam. An approximate structure of the zeroth diffraction order is shown on the right to emphasize the non-perfect diffraction efficiency of the phase mask shown on the SLM. The colours of the cross sections correspond to spatially varying phases, as introduced in the colourmap of figure 2.1. Note that the radial amplitude structure of the beam changes in propagation since simply imprinting a phase structure on a Gaussian beam creates a complex superposition of modes of differing mode order, where different components of the superposition might have different Gouy phase terms.

order.

Since such simple structuring cannot perform arbitrary amplitude modulations, a different technique needs to be used for modulating the phase and amplitude of a light field with a single reflection off of a phase-only SLM. Fortunately, such methods do exist and the operation principle behind them often relies on scattering or diffracting the unwanted parts of the light field into a different direction [166–169]. Besides the referenced methods, one can also create such phase masks through a modified Gerchberg-Saxton algorithm [170, 171]. In our experiments, we used the method detailed in reference [169], where the diffraction efficiency of a blazed grating term is scaled depending on how much amplitude we want to send into the first diffraction order at each transverse position. For convenience, we will be referring to this method as mode carving. The diffraction efficiency is reduced by allowing the grating to only use a fraction of the 2π range. Note that the relation between the wanted field amplitude and grating phase range is not linear [166, 169]. Figure 3.5 shows an example

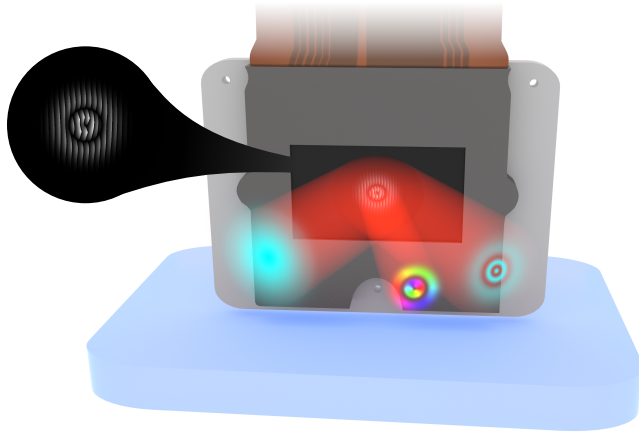


Figure 3.5 A rendered image showing a phase mask performing amplitude and phase modulation on the first diffraction order of the mask. The input field is a Gaussian field and an estimation of the field shape in the zeroth diffraction order is shown on the right. The output field is also shown as an ideal mode here, without considering possible sources of error.

of such a mask carving an LG mode with radial index $p = 1$ and OAM index $\ell = 1$.

In the final experiment (**publication III**), we also performed an additional correction to the mode carving method. Specifically, with this correction we took into account the Gaussian shape of the input field. The original carving method uses a large input beam that can be approximated as a plane wave but, in some cases, the results can be significantly improved by taking the shape of the input beam into account. The correction was done by calculating the carving phase mask for a transverse field

$$\Psi(\mathbf{r}_{px}) = \frac{A(\mathbf{r}_{px})}{A_G(\mathbf{r}_{px})} e^{i\Phi(\mathbf{r}_{px})}, \quad (3.3)$$

where $A(\mathbf{r}_{px})e^{i\Phi(\mathbf{r}_{px})}$ is the field structure we want to generate and $A_G(\mathbf{r}_{px})$ is the real amplitude structure of the initial Gaussian light field the mask is applied to. Here, \mathbf{r}_{px} are the two-dimensional coordinates identifying the centres of each pixel in the device and $A(\mathbf{r}_{px})$ is a real amplitude function. Although this added envelope can correct for some of the unwanted effects caused by the input beam shape, the incident Gaussian beam should still be kept larger than the wanted transverse structure to minimize the losses accrued in the

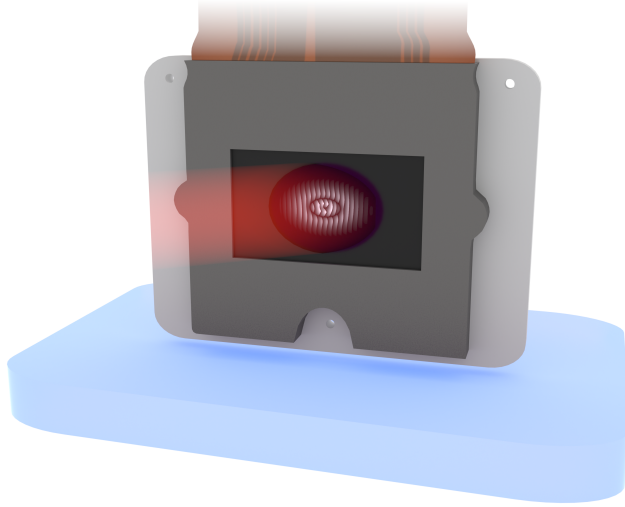


Figure 3.6 An exaggerated image highlighting that for a beam at an extremely large input angle, the illuminated area on an SLM is elliptical. An example of a phase mask taking into account the elliptical shape of the input beam is also shown.

carving process. Additionally, if one wants to implement further corrections to equation (3.3), the amplitude structure $A_G(\mathbf{r}_{px})$ can be changed to a complex field that includes details such as a possible quadratic phase structure, in case the incident beam is not exactly at the waist position. More details on this amplitude correction can be found in the supplementary of reference [172].

One more additional correction we can include in any phase mask type is taking into account the angle of incidence of our incident beam. Such a correction is not often necessary but increases in importance if larger incidence angles are used on the SLM. Since we have to use the SLM at an incidence angle larger than zero to have a sufficient spatial separation between the input and output beams, the SLM plane is not perfectly perpendicular to the propagation direction of the beam. Hence, the area that a circular beam (such as a Gaussian beam) illuminates on the SLM is slightly elliptical. This ellipticity produces some unwanted effects on the modulated field which can be reduced by calculating the phase mask in elliptical coordinates, where the longer axis of the corresponding ellipse is within the plane of incidence. This effect and correction are visualized in figure 3.6. This correction was used in the second experiment (**publication II**) of this thesis to improve the results.

3.4.2 Single Mask Measurements of Spatial Structure

To measure the transverse field structure of a classical field, one can employ methods utilizing interferograms such as off-axis digital holography [157]. However, such methods do not work as well for determining the structure of a single photon since they require many copies of the photon to be prepared and interfered with a coherent reference beam. Because of this, projective methods are commonly used to measure the spatial structure of a single photon. Such methods often involve types of filters which ensure that only photons with a non-zero spatial overlap to a given field structure can end up at a certain detector. Ideally, we would have efficient sorting schemes [173–183] where a set of N different orthogonal spatial field structures are separated into N paths that lead to N different detectors. Although certain sorting procedures are also possible with a single phase transformation [184, 185], we limit ourselves to filtering for a single transverse field at a time, using a single phase mask. Such single-mode filtering measurements reduce the number of required single-photon detectors, offer decent efficiency, and are flexible when filtering for arbitrary transverse field structures.

Methods that filter for transverse field structures usually rely on using a phase mask on an SLM and a subsequent SMF. The SMF, as the name suggests, allows only a single transverse spatial mode to couple into the fibre efficiently. For standard SMFs, this mode is approximately a Gaussian mode. Since propagating a field from an SLM and focusing it down to an SMF is a unitary transformation (ignoring small losses)[125], this ensures that the overlap is conserved between a pair of transverse fields after the propagation. Hence, we can calculate the probability of a single photon coupling into an SMF, after a phase transformation at an SLM, by calculating the overlap of the photon spatial structure and the mode of the SMF, at the SLM plane. If we limit ourselves to a paraxial beam with a single polarization and wavelength, while defining $\psi_{in}(\mathbf{r}_\perp)$ as the photons normalized spatial structure, $M(\mathbf{r}_\perp)$ as the phase mask structure, and $\psi_G(\mathbf{r}_\perp)$ as the approximately Gaussian field structure of the SMF, back-propagated to the SLM plane, the probability of coupling is given by

$$\left| \int d^2\mathbf{r}_\perp M(\mathbf{r}_\perp)\psi_{in}(\mathbf{r}_\perp)\psi_G^*(\mathbf{r}_\perp) \right|^2. \quad (3.4)$$

Note that the above equation can be derived from the Born rule (Eq. (2.67)) and an overlap relation for paraxial beams, similar to the one shown in equation (2.66).

Since such a filtering measurement process is the reverse of the process performed when generating transverse spatial modes with a single phase mask, the same masks and corrections can be applied for measurements as for the shaping of Gaussian beams. For example, if we are only interested in measuring the OAM of the photon, we can employ the same phase-only masks described in the previous section, and couple the first diffraction order of this mask into the SMF. Hence, the combination of the phase mask and SMF acts as an OAM filter for the photons. The type of mask used for measuring depends on whether we need to also measure the amplitude structure, and if we can afford the losses of the mode carving masks. With the mode carving masks, the same corrections seen in section 3.4.1 can be introduced when taking into account the shape of the back-propagated SMF mode. This means that a correction similar to the one in equation (3.3) can be added, or the size of the back-propagated Gaussian can be increased to approximate a plane wave [186]. Note that the mask filtering for a specific spatial structure should be calculated by using the complex conjugate of the field being measured, as can be seen from equation (3.4).

3.5 Multi-Plane Light Conversion

In the previous sections, we discussed how a single phase modulation plane on an SLM can be used to shape and measure the transverse field structure of light. As we noticed, however, the more complex the shaping gets, the more losses such methods intrinsically have. Thus, to maintain high efficiency when increasing the complexity of a transformation, we can distribute the shaping of the transverse field structure over multiple planes. Methods that perform such light shaping with multiple linear optical elements separated by free-space propagation are categorized as MPLC schemes [125, 187]. Although this definition is quite general and could be interpreted to include any linear optical system with multiple components, the term is usually reserved for systems where phase-only SLMs or custom phase plates are used.

MPLC devices enable the simultaneous shaping of the phase and amplitude

profile by solely utilising phase manipulation masks which are ideally lossless. The individual phase masks allow us to change the transverse phase structure, and the propagation between multiple phase-modulating masks allows us to shape the amplitude structure. In the mode picture, this amplitude shaping can be attributed to the differing Gouy phase evolution between the paraxial modes the previous phase mask “excites” in the beam.

MPLC transformations can be designed to convert a single transverse field structure to a different one [125, 188] or to map pairwise a large set of orthogonal input structures into a different large set of output modes, with one static device. These large sets of orthogonal structures include orthogonal transverse fields propagating in a single beamline [66] and transverse fields sufficiently separated from each other on the transverse plane to make the fields orthogonal [174, 181, 187, 189–191]. Here we will focus on transformations within a single beamline, one example of which, implemented on an SLM, is shown in figure 3.7.

MPLC is, in principle, capable of shaping any set of d modes into any other set of d modes, as long as the linear transformation is unitary and there is a sufficient number of phase modulation planes. Although, unfortunately, there does not seem to be a clear way of determining the necessary number of phase planes needed for a given task as this number is highly dependent on the specific transformation being performed. In reference [125], the authors reported that for a specific construction of an MPLC, it is possible to perform any unitary transformation using MPLC, provided a sufficiently large but finite number of phase manipulation planes. However, as the authors also noted, compromises might need to be made on the quality of the MPLC transformation due to a limited number of available phase manipulation planes. Based on existing literature, transformations of a single paraxial mode, e.g. LG modes, seem to require three phase manipulation planes [125, 188]. When scaling up to an arbitrary number of input fields, a differing number of phase manipulation planes have been used and reported on. For example, in reference [187] the authors state that they have arrived empirically at a rule that, in general, a transformation with d inputs and outputs requires $2d + 1$ phase manipulation planes. However, as the method has been developed, specific transformations have been shown to require a significantly smaller number of planes without compromising too much on the quality, e.g. 7 phase manipulation planes for 210

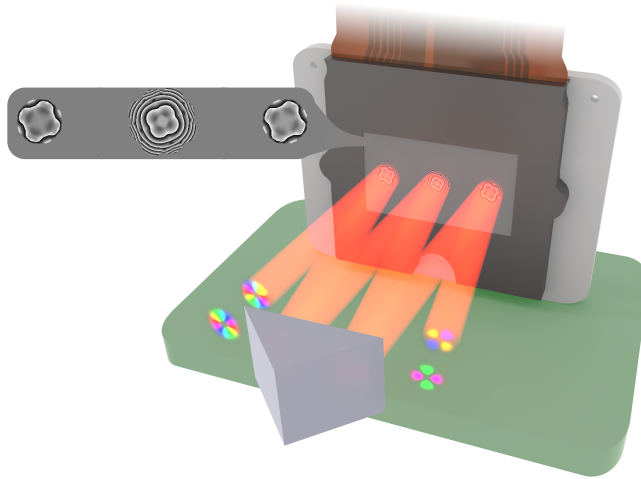


Figure 3.7 An example of an MPLC device implemented on an SLM using three phase modulation planes. The device allows for consecutively shaping the transverse phase profile at the masks while enabling amplitude modulation through propagation between each phase mask. The beam is reflected three times off of three different sections of the SLM by placing a mirror in front of it. To minimize the change of the beam being cut when passing next to the mirror, the mirror chosen for this application was a coated right-angle prism mirror. The shown transformation performs a beamsplitter-like unitary mapping for the two-dimensional set of LG modes with radial index $p = 0$ and OAM $\ell = \pm 2$, shaping either one of these modes into an even superposition of the two. The output superpositions are orthogonal to each other since the unitary device preserves the orthogonality of the input modes.

transverse spatial modes [174]. Additionally, in some applications the overall accuracy of the total unitary transformation might not be of importance and lower conversion efficiencies could be tolerated as long as, within the desired mode set, the cross-talk between the wanted output fields is small.

3.5.1 Wavefront Matching

At the heart of any MPLC device are the phase manipulation masks. To design a set of these phase manipulation masks, an inverse design optimization method is usually employed. This optimization usually takes some of the constraints and limitations of the physical system into account. Different methods have been suggested and used for the optimization of MPLC systems [192] and other similar systems [193], but the method used to optimize phase masks in the

present work was wavefront matching (WFM).

One example of an MPLC system, with three phase masks optimized through WFM, is shown in figure 3.8. The same transformation is also shown in figure 3.7 but in figure 3.8 we also see some of the intermediate stages of the smooth transformation provided by MPLC. To give a simple example of a multiplexing MPLC system, figure 3.9 shows an example of how the same WFM algorithm can be used to create a two-mode multiplexing device with five phase masks.

WFM gets its name from a waveguide design method [194], and one explanation of the method is given in reference [190] (with example codes provided in references [174, 195]). When using WFM, we first select the number of phase modulation planes N , set the free space propagation distance Δz between the planes, select the set of input modes (a set of normalized transverse-field structures $\{f_i(\mathbf{r}_\perp)\}$), and the desired set of output modes (a set of normalized transverse-field structures $\{b_j(\mathbf{r}_\perp)\}$). Before proceeding with the optimization, it is recommended to verify that the desired transformation is unitary. For most applications, this verification can be done by making sure that both the input and output field sets contain mutually orthogonal fields. To begin the optimization, we simulate the propagation of the transverse input fields forward through the system. In the simulation, we usually limit ourselves to a grid with the same pixel pitch as the SLM we are using. The wanted output fields are then conversely propagated backwards through the same system. To perform both of these propagations, we use the ASR propagation described in section 2.1.3, using the FFT algorithm to perform the Fourier transforms.

After the initial fields are propagated through the system, we can start optimizing the blank phase masks in sequence. Of course, as we update the phase masks over multiple iterations, we need to also keep updating the propagated fields as the updated masks affect the propagation of the fields through the system. The basic principle behind the method for updating the individual masks is to minimize the phase differences between each forwards-propagated input mode and corresponding backwards-propagated output mode at every phase mask plane. This process is then repeated while cycling through the phase mask planes until a minimum difference between the wanted output and the simulated output is reached. Ideally, this gives us a smooth transition by

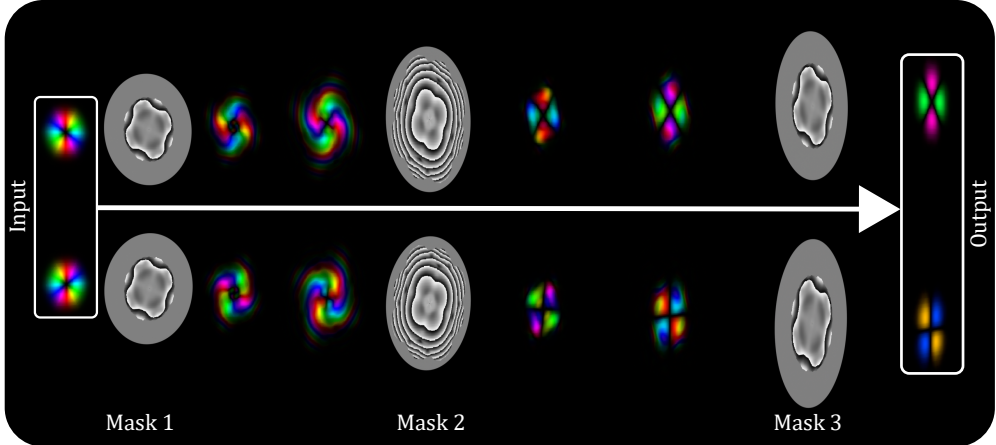


Figure 3.8 An image showing how an MPLC with three phase masks converts either of two input modes into their corresponding output mode. The masks are calculated with the WFM method to transform the two input modes with a single set of masks, in the same beamline. Some intermediate field structures are also shown to highlight the smooth transformation the device performs. The transformation shown here is identical to the one shown in figure 3.7.

perfectly matching the wavefronts of the forwards-propagated inputs with the backwards-propagated outputs at every phase modulation plane. The optimization can be started from any one of the phase masks and we first calculate the spatially varying phase difference between each pair of input and output modes at this mask. The difference is calculated by multiplying the forwards-propagated beam by the complex conjugate of the backwards-propagated beam at each pixel of the simulation grid

$$o_{kj}(x, y) = f_j(x, y; (k - 1) \times \Delta z) b_j^*(x, y; (k - 1) \times \Delta z), \quad (3.5)$$

where k is the index labelling the specific phase mask plane corresponding to a z -position $(k - 1) \times \Delta z$ (with mask $k = 1$ set at $z = 0$). The index j labels the pair of input and output modes. At this stage, if our optimization included only one phase modulation plane and one input-output mode pair, we could perfectly match the input to the output using a phase mask with the phase structure

$$\Phi_1 = -\arg(o_{11}), \quad (3.6)$$

provided that the amplitude structures of both the input and output were

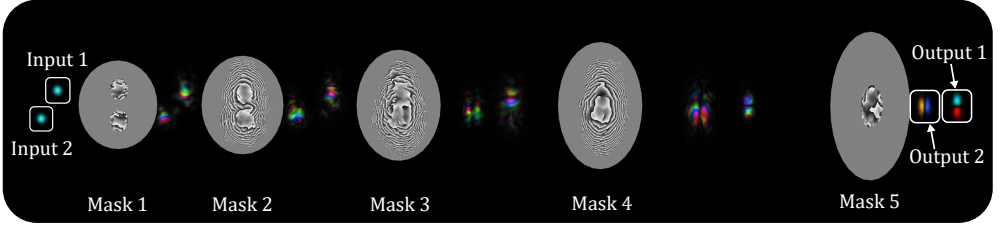


Figure 3.9 An image showing a multiplexing MPLC converting two Gaussian inputs, sent in at different transverse positions, to two Hermite-Gaussian modes in the same beamline. The MPLC uses 5 phase masks and the intermediate field structures are again shown in between the masks. Compared to the transformation in figure 3.7, the masks here have much higher spatial frequencies, which is due to this specific transformation being more difficult to implement, at least with the specific MPLC settings chosen for this transformation.

identical at the plane $k = 1$. This can be seen by stating the input field as

$$f_i(x, y; (k - 1) \times \Delta z) = a_f(x, y) \exp(i\theta_f(x, y))$$

and the output field as

$$b_i(x, y; (k - 1) \times \Delta z) = a_b(x, y) \exp(i\theta_b(x, y)).$$

With these definitions the single phase mask takes the form

$$\Phi_1(x, y) = -\theta_f(x, y) + \theta_b(x, y).$$

If we then set

$$a_f(x, y) = a_b(x, y) = a(x, y),$$

at the phase mask, our forward propagated beam exactly matches the wanted output after the phase mask

$$e^{i\Phi_1(x,y)} f_1(x, y; 0) = a(x, y) e^{i(\theta_f(x,y) - \theta_f(x,y) + \theta_b(x,y))} = b_1(x, y; 0). \quad (3.7)$$

In a more general situation, our device has multiple input-output pairs. Then the new phase mask is calculated as a sum of the o_{kj} terms for each pair of modes

$$\Phi_k(x, y) = -\arg \left(\sum_j o_{kj}(x, y) e^{-i\phi_j} \right). \quad (3.8)$$

This sum is comparable to a weighted average of the field overlaps at the plane k . This weighting comes from the amplitude of the product fields $o_{kj}(x, y)$, which gives more weight to positions where the amplitude of this product is larger. The additional phase factor ϕ_j is introduced to ensure that each term $o_{kj}(x, y)$ in the sum adds constructively to the new phase mask structure, while allowing the global phase of each input field to vary in the final transformation. In reference [190], and in the code provided with reference [174], the phase factor is the phase of the overlap integral between the mask calculated in the previous iteration $\Phi_k^{(\text{prev})}(x, y)$ and the product $o_{kj}(x, y)$

$$\phi_i = \arg \left(\int d^2\mathbf{r}_\perp o_{kj}(x, y) e^{i\Phi_k^{(\text{prev})}(x, y)} \right). \quad (3.9)$$

In simulation, the integral turns into a sum over the finite and discrete simulation grid where our initial input and output fields are normalized. However, based on our limited testing of the method, it does not seem to matter whether the mask from the previous iteration is taken into account. Simply using $\phi_i = \arg \left(\int d^2\mathbf{r}_\perp o_{kj}(x, y) \right)$, instead of the function given in equation (3.9), seems to produce equally good results in the update procedure described here ¹. The phase factor and mask update procedure used in **publication I** are identical to the ones in the code provided in reference [195].

With a sufficient number of iterations, the process almost always converges to a solution where the difference between the simulated and wanted output modes is minimized. Unfortunately, however, this minimum can be local [190] and, to change the outcome, the number of parameters and constraints one can apply to the optimization procedure are numerous.

3.5.2 Constraints and Parameters in Wavefront Matching

To improve the result of the WFM algorithm, we can change the numerous parameters used in the optimization procedure or include additional constraints that encourage the algorithm to arrive at certain types of solutions. In this final section of this chapter, we will look at some of the constraints we have found

¹However, if the term $\Phi_k(x, y)$ is used more as an updated structure added to the previous phase mask, instead of a completely new mask which we can use while discarding the previous one, equation (3.9) might be the better option.

useful when designing MPLC masks. We will also talk about the effects that some of the parameters have on the end results.

Based on experience, smoother phase masks seem to work better in the physical implementation of MPLC devices. Although there are numerous tricks one could think of to reach such an end result, we often achieve this by using a set of multiple wavelengths in the optimization. In the WFM algorithm, this can be implemented by simulating the propagation of the input-output pairs over a set of wavelengths around the wanted operation wavelength. In this case, the sum in equation (3.9) is summed over field pairs of different wavelengths as well. This usually minimizes the amount of higher spatial frequencies in the mask as those can result in drastically different behaviours for light with different wavelengths. It thus reduces the number of small details, limits the number of adjacent pixels with a large difference in grey values (which can cause significant pixel cross-talk on an SLM), and increases the bandwidth of the resulting phase masks. Of course, if gratings are added to these phase masks, as discussed in section 3.4, the bandwidth of the masks, and the number of phase jumps, will be defined by the grating instead of the underlying phase transformation. When adding multiple wavelengths to the WFM algorithm, it is especially important to equalize the average phase² for each term in the sum of equation (3.8). This is because the different wavelength components might have different global phases, although the transformations might be similar. Hence, the different terms o_{kj} would start interfering with each other in unwanted ways, unless the global phases of each term are adjusted.

Besides adding more wavelengths, adding absorbing boundaries to the simulation grid can help with removing nonphysical artefacts. The specific artefacts these boundaries remove are created when a part of the light field crosses the edge of the simulation grid. Although these artefacts are not an issue with all transformations, in tasks requiring large spatial frequencies they become more prevalent. When implementing the absorbing boundaries, we have found that applying them at the phase mask location is usually not sufficient. Thus, we also need to apply the absorbing edges at locations between the masks. Hence, we apply the absorbing edges by distributing these absorption planes randomly, in every iteration.

²This is taken care of by the phase factor in equation (3.9).

One more addition that can help in creating better solutions is partially or completely neglecting the low-intensity parts of the field in the mask updating procedure. An example of such a parameter is given in the example code of reference [174]. Lastly, enforcing symmetries such as rotation, reflection, or inversion symmetry on one or more of the masks, has also produced better results in some physical implementations. However, the effectiveness of this constraint is highly dependent on the transformation in question and the symmetries of the set of input and output modes.

Besides these constraints, parameters such as the size of the fields and propagation distance between phase masks can have a large effect on the solution the algorithm finds. Hence, the solutions can also be improved, quite significantly, by optimizing these parameters. More about the constraints and parameters in WFM can be found in references [174, 190].

To further improve the WFM algorithm, one could also consider additional experimental imperfections which could affect the physical implementation of the transformation. Some imperfections, which we did not consider in our own WFM algorithm, include the effects caused by the fields input angle to the phase masks (similar to the effects discussed in section 3.4), the effects of the discrete pixel size of the SLM, the fill factor of the SLM screen [153], and the pixel crosstalk.

4 PHOTON BUNCHING IN SPATIAL MODES

With the overview of the theoretical background in chapter 2 and the detailed look into the experimental methods in chapter 3, we will now use these concepts to explore two-photon interference in transverse field structures. We will start by looking into what photon bunching exactly is and how it works in the transverse-spatial degree of freedom, after which we move on to utilizing states produced by photon bunching as tools in the next two chapters

4.1 Two-Photon Interference

Photon bunching is a type of quantum interference between multiple photons and its name refers to how photons tend to group together, into the same mode, in certain situations. This bunching is a result of the bosonic nature of photons. One of the most common examples of photon bunching is HOM interference where two photons enter a balanced beamsplitter as is shown in figure 4.1. To calculate how quantum interference occurs in this scenario, we first assume that the photons occupy two paraxial modes $\{1, 2\}$, which allows us to write the quantum state in the form

$$\begin{aligned}
 |\Psi^{\text{in}}\rangle &= |1\rangle_{1,a} |1\rangle_{2,b} = \hat{a}_1^\dagger \hat{b}_2^\dagger |\{0\}\rangle \\
 &= \sum_{\sigma,\ell,p} \sum_{\sigma',\ell',p'} \int_0^\infty dk_0 \int_0^\infty dk'_0 C_{\sigma,\ell,p}^{(1)}(k_0) C_{\sigma',\ell',p'}^{(2)}(k'_0) \hat{a}_{\sigma,\ell,p}^\dagger(k_0) \hat{b}_{\sigma',\ell',p'}^\dagger(k'_0) |\{0\}\rangle,
 \end{aligned}
 \tag{4.1}$$

where we have stated the general paraxial beam in the LG basis according to equation (2.60). The indices $\{1, 2\}$ label the different properties of each photon, and the letters \hat{a} and \hat{b} used in the creation operator denote the different optical axes that the two photons have. The different photon paths also make the modes orthogonal. The operation of the balanced beamsplitter on these two input modes can be represented by a unitary transformation similar to the one

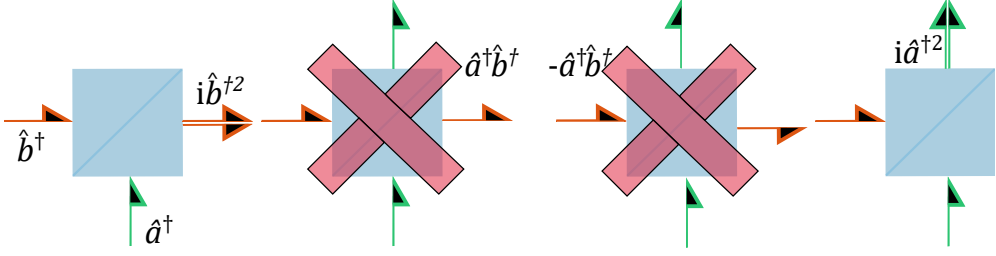


Figure 4.1 Picturesque representation of the quantum interference process described in equations (4.4) and (4.5). In the picture, two photons enter the beamsplitter from two separate input ports. The representation shows a set of classically expected output possibilities for the photon pair. The two terms where the photons would exit from separate output ports interfere destructively and the two photons bunch together. The figure is adapted from **publication I**.

shown in section 2.3

$$U = \frac{1}{\sqrt{2}} \begin{bmatrix} 1 & i \\ i & 1 \end{bmatrix}. \quad (4.2)$$

Hence, our operators evolve as

$$\hat{a}_1^\dagger \longrightarrow \frac{1}{\sqrt{2}} \left(\hat{a}_1^\dagger + i\hat{b}_1^\dagger \right), \quad \hat{b}_2^\dagger \longrightarrow \frac{1}{\sqrt{2}} \left(i\hat{a}_2^\dagger + \hat{b}_2^\dagger \right), \quad (4.3)$$

giving us an output state

$$|\Psi^{\text{out}}\rangle = \frac{1}{2} \left(i\hat{a}_1^\dagger\hat{a}_2^\dagger + \hat{a}_1^\dagger\hat{b}_2^\dagger - \hat{b}_1^\dagger\hat{a}_2^\dagger + i\hat{b}_1^\dagger\hat{b}_2^\dagger \right) |\{0\}\rangle. \quad (4.4)$$

From the above equation, we can see that if the transverse structures 1 and 2 are exactly identical, i.e. $C_{\sigma,\ell,p}^{(1)}(k_0) = C_{\sigma,\ell,p}^{(2)}(k_0)$, the two middle terms cancel each other and we are left with a two-photon N00N state between paths a and b

$$|\Psi^{\text{out}}\rangle = \frac{i}{2} \left(\hat{a}^{\dagger 2} + \hat{b}^{\dagger 2} \right) |\{0\}\rangle = \frac{i}{\sqrt{2}} \left(|2\rangle_a |0\rangle_b + |0\rangle_a |2\rangle_b \right). \quad (4.5)$$

Hence, the two photons bunch together and only exit the beamsplitter in the same output port. Figure 4.1 also gives a visual demonstration of this interference. Note however that we cannot know which output port the two photons exit from since they are in a superposition of being in path a “and/or” b . Additionally, since the unitary given in equation (4.2) is a MUB transformation, this example shows us that two-photon interference can be achieved by a change

into a different MUB.

If our two photons are not exactly indistinguishable $C_{\sigma,\ell,p}^{(1)}(k_0) \neq C_{\sigma,\ell,p}^{(2)}(k_0)$, nor perfectly orthogonal $\sum_{\sigma,\ell,p} \int_0^\infty dk_0 C_{\sigma,\ell,p}^{*(1)}(k_0)C_{\sigma,\ell,p}^{(2)}(k_0) \neq 0$, some quantum interference still occurs but with lower visibility. To demonstrate this, we can calculate the rate of coincident detections, similarly to the calculation performed in reference [196], using a projector

$$\hat{P} = \hat{P}_a \otimes \hat{P}_b, \quad (4.6)$$

with

$$\hat{P}_a = \sum_{\sigma,\ell,p} \int_0^\infty dk_0 \hat{a}_{\sigma,\ell,p}^\dagger(k_0) |\{0\}\rangle \langle\{0\}| \hat{a}_{\sigma,\ell,p}(k_0) \quad (4.7)$$

and

$$\hat{P}_b = \sum_{\sigma,\ell,p} \int_0^\infty dk_0 \hat{b}_{\sigma,\ell,p}^\dagger(k_0) |\{0\}\rangle \langle\{0\}| \hat{b}_{\sigma,\ell,p}(k_0). \quad (4.8)$$

By assuming that the unitary in equation (4.2) applies similarly to all LG modes and wave numbers being used, we can calculate the probability of detecting two photons in paths a and b simultaneously, from the state $|\Psi^{\text{out}}\rangle$, by calculating the projection

$$\begin{aligned} P_{\text{coinc}} &= \langle \Psi^{\text{out}} | \hat{P}_a \otimes \hat{P}_b | \Psi^{\text{out}} \rangle \\ &= \frac{1}{2} \left[1 - \left| \sum_{\sigma,\ell,p} \int_0^\infty dk_0 C_{\sigma,\ell,p}^{*(1)}(k_0) C_{\sigma,\ell,p}^{(2)}(k_0) \right|^2 \right], \end{aligned} \quad (4.9)$$

where we see that the coincidence detection probability ranges between 1/2 and 0, depending on the overlap of the modes (1) and (2) [22, 196]. This means that our coincidence detection probability will get closer to zero as the transverse structures (ℓ, p) , the polarization structures (σ) , and the spectral/temporal profiles $(k_0 = \omega_0/c)$ of the two photons get more identical. Hence, the two-photon detection probability can be tuned by, e.g., changing the arrival times of one of the photons compared to the other.

In our experiments, we tune this detection probability by moving the delay stage in the source (see figure 3.1). As is explained in reference [196] and can be inferred from the time dependence given in section 2.2.1, this delay effectively

corresponds to a frequency-dependant phase factor

$$\hat{b}^\dagger(k_0) \longrightarrow \hat{b}^\dagger(k_0)e^{-ik_0c\tau}, \quad (4.10)$$

where τ is the amount of time delay between the photons. To give an example of the effect of this temporal delay, we will assume that both of the photons have a uniform circular polarization σ_0 , a single-mode LG structure corresponding to indices $\{\ell_0, p_0\}$, and a Gaussian frequency profile centred at k_0 with a Gaussian width ς (related to the spectral width [19])

$$C_{\sigma,\ell,p}^{(1)}(k_0) = C_{\sigma,\ell,p}^{(2)}(k_0) = \begin{cases} \sqrt{\frac{c}{\varsigma\sqrt{\pi}}} e^{\frac{-c^2(k_0-k_c)^2}{2\varsigma^2}} & , \sigma = \sigma_0, \ell = \ell_0, p = p_0 \\ 0 & , \text{ otherwise} \end{cases} \quad (4.11)$$

Inserting this into equation (4.9), while noting that the phase shift in equation (4.10) effectively changes $C_{\sigma,\ell,p}^{(2)}(k_0)$ to $C_{\sigma,\ell,p}^{(2)}(k_0)e^{-ik_0c\tau}$, gives us

$$\begin{aligned} P_{\text{coinc}} &= \frac{1}{2} \left[1 - \left| \int_0^\infty dk_0 \frac{c}{\varsigma\sqrt{\pi}} e^{\frac{-c^2(k_0-k_c)^2}{\varsigma^2}} e^{-ik_0c\tau} \right|^2 \right] \\ &= \frac{1}{2} \left[1 - \left| \frac{1}{\sqrt{\pi}} \int_{-x_0}^\infty dx e^{-x^2 - i\varsigma\tau(x+x_0)} \right|^2 \right], \end{aligned} \quad (4.12)$$

where we have defined $x = c(k_0 - k_c)/\varsigma$, giving us the constant $x_0 = ck_c/\varsigma$. To calculate the integral, we can approximate that the lower limit is effectively at $-\infty$, as the constant x_0 is ~ 150 , for our experimental parameters, and the Gaussian envelope e^{-x^2} differs significantly from zero only within the range $(-3 \leq x \leq 3)$. This makes the integral into a regular Fourier transform, which simplifies equation (4.12) to

$$P_{\text{coinc}} = \frac{1}{2} \left[1 - e^{-\frac{\varsigma^2\tau^2}{2}} \right]. \quad (4.13)$$

Hence, as the temporal overlap of our photons is adjusted, the coincidence probability varies in a Gaussian manner, reaching a minimum at $\tau = 0$. This can also be seen from the plot of equation (4.13) in figure 4.2.

From the above calculations, we see that the only requirement for HOM interference to occur in a unitary transformation is to make the output modes

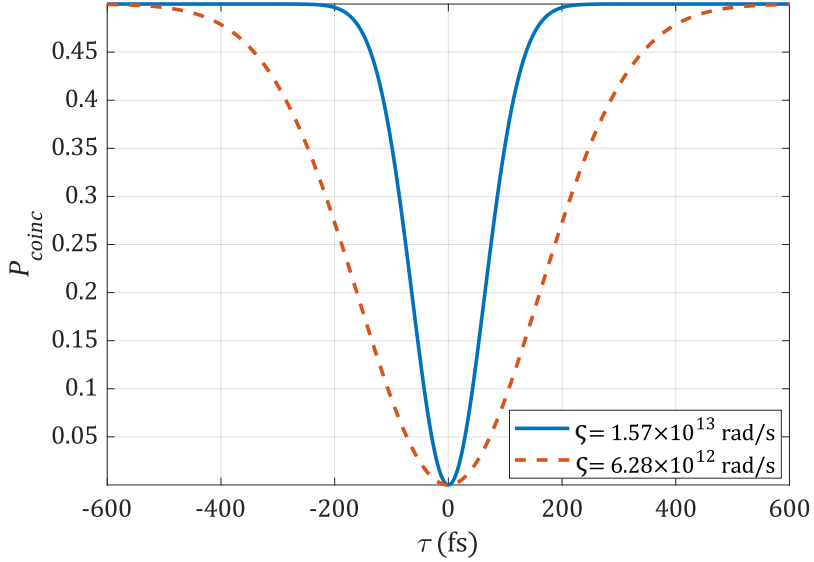


Figure 4.2 Plot of two different coincidence probability curves calculated with equation (4.13). The plots are made with two different values of ζ , where the blue solid curve corresponds to a value of ζ that roughly matches our experiment in **publication I**.

of the two photons indistinguishable from each other. Hence, photon bunching can be induced when the two photons are independent of each other, even when created in two different sources [197]. This is an important detail for applications of multi-photon interference such as some quantum communication and certain linear optical quantum computing schemes [22].

Experimental results

The first measurement we performed was to verify the indistinguishability of the photon pairs produced by our source (see sec. 3.1). To do this we measured HOM interference using a fibre beamsplitter instead of a free-space beamsplitter. This essentially involved adding the fibre beamsplitter between the source and the detectors, after which we scanned the delay stage to change the temporal overlap of the two photons. The measured two-photon coincidence data, accompanied by the single photon data in each detector, is shown in figure 4.3.

As can be seen from figure 4.3, our photons were not perfectly indistinguishable from each other, and they also did not produce the same Gaussian

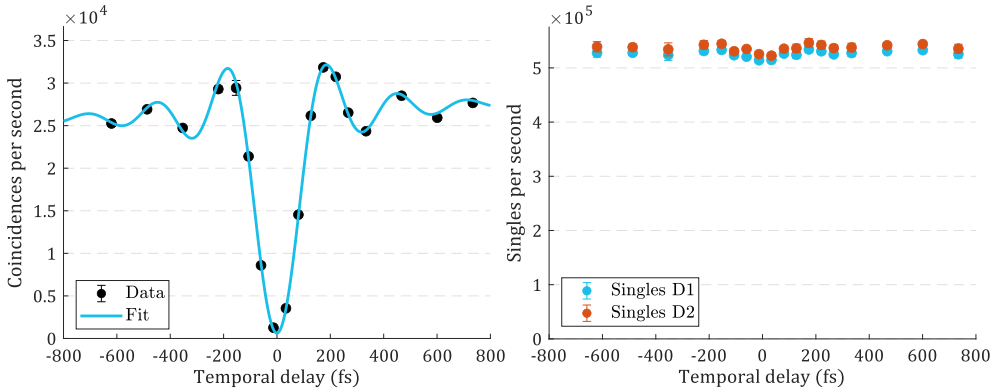


Figure 4.3 Plot of measured two-photon coincidence data over different temporal delays (left) with the corresponding single detections (from detectors D1 and D2) shown on the right. Accidental coincidences have been removed from the data and the solid line is a fit of the form shown in equation (4.14). The visibility of the two-photon interference (as defined in equation (4.15)) was $v = (97.7 \pm 0.02)\%$, calculated from the fit to the data. The error bars in the plot are standard deviations and the error in the visibility is a standard error calculated from the fit. The measurement was performed with the source settings used in **publication I** but with an effectively lower pump power (around 1.5 mW) to reduce the number of accidentals and minimize the effects of detector nonlinearity. The fluctuations in single counts are caused by a changing rate of two-photon states $|2\rangle$ arriving at each detector. As our detectors see these two-photon states as just a single detection, the overall number of detections slightly fluctuates as a consequence. The figure is a reprint of a figure in the supplementary material of **publication I** [198].

interference curve. Instead, the calculation of the dip shape is slightly more complicated due to the spectral correlations of SPDC photons [196]. In our system, the roughly rectangular transmission band of the BPF gives the HOM interference a sinc-like structure, as was calculated for a similar scenario in reference [199]. However, due to the filter not being a perfect rectangle, in addition to other wavelength filtering effects, our two-photon coincidence rates effectively follow a profile

$$R_c = R_{cl} \left(1 \pm v \operatorname{sinc}(d_1 \tau) e^{-(d_2 \tau)^2} \right) + S\tau, \quad (4.14)$$

where R_{cl} is the classically expected rate of photons, d_1 and d_2 are constants that depend on the spectral profile of the photons, and v is the visibility of the interference defined as

$$v = |R_{cl} - R_{qu}| / R_{cl}, \quad (4.15)$$

with R_{qu} being the coincidence detection rate at $\tau = 0$. The coefficient S is a slope that takes into account any linear decoupling, either over time or due to changes in the delay stage position. In equation 4.14, the Gaussian term is added as an ad hoc correction term to get a better fit to the data and the two different signs for v are used since the shape of the interference curve is inverted for certain measurement scenarios. As an example, for the state in equation (4.4), if we measured the number of photon pairs in path a instead of measuring coincident detections between the two paths a and b , our interference curve would have the plus sign in equation (4.14) [22].

4.2 Two-Photon Interference in Spatial Mode Unitaries

In the previous section, we saw one example of two-photon interference when we placed two photons into a superposition of two different paths using a MUB transformation. This is the most famous of such experiments [19] and is the most common type of two-photon interference in photonic quantum technological applications. However, as mentioned in the introduction, this is not the only manifestation of such two-photon interference. Specifically, for any unitary device placing the photons into a superposition of an arbitrary set of orthogonal modes, a similar interference should occur [26–28].

In **publication I** we set out to demonstrate that arbitrary control of such bunching is possible, while only shaping the transverse spatial field structure. To perform the initial test, we needed a unitary device that could bunch two photons with orthogonal transverse structures, within the same beam path. Effectively, the device should take a state with two photons in orthogonal LG modes

$$\begin{aligned} |\Psi^{\text{in}}\rangle &= |1\rangle_{-1,(1)} |1\rangle_{+1,(2)} \\ &= \int_0^\infty dk_0 \int_0^\infty dk'_0 C^{(1)}(k_0) C^{(2)}(k'_0) \hat{a}_{1,-1,0}^\dagger(k_0) \hat{a}_{1,+1,0}^\dagger(k'_0) |\{0\}\rangle. \end{aligned} \quad (4.16)$$

and send them into a superposition of the two modes we want the photons to bunch into. That is, the device would ideally perform a MUB transformation on the transverse spatial modes, instead of photon paths. For our measurement, we chose LG modes with OAM quanta $\ell \pm 1$ which the unitary would transform

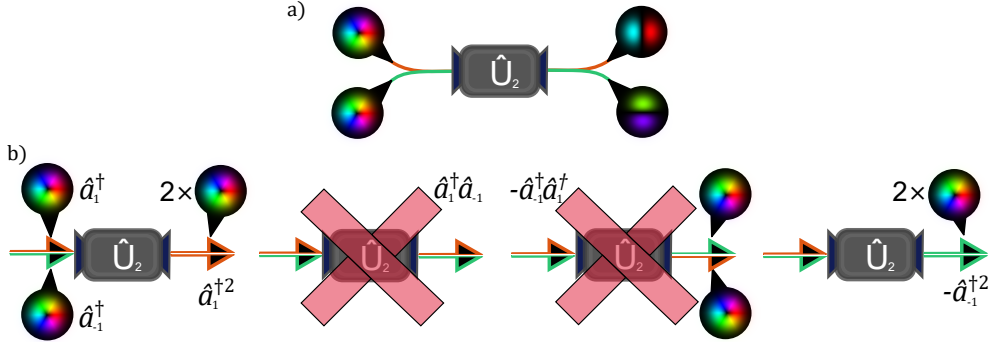


Figure 4.4 Picturesque representation of the quantum interference process in a modesplitter for two LG modes. Here the device \hat{U}_2 is a black box converting the two LG modes according to equation (4.17) as is shown in (a). (b) shows the bunching in the modesplitter, similarly to figure 4.1. The figure is adapted from **publication I**.

as

$$\begin{aligned} \hat{a}_{1,-1,0}^\dagger(k_0) &\longrightarrow \frac{1}{\sqrt{2}} \left(\hat{a}_{1,1,0}^\dagger(k_0) - \hat{a}_{1,-1,0}^\dagger(k_0) \right) \\ \hat{a}_{1,+1,0}^\dagger(k_0) &\longrightarrow \frac{1}{\sqrt{2}} \left(\hat{a}_{1,1,0}^\dagger(k_0) + \hat{a}_{1,-1,0}^\dagger(k_0) \right). \end{aligned} \quad (4.17)$$

This unitary mapping is similar to the beamsplitter transformation, but this time in the transverse-spatial degree of freedom. Hence, similarly to the previous section, the device should give us an output state

$$\begin{aligned} |\Psi^{\text{out}}\rangle &= \int_0^\infty dk_0 \int_0^\infty dk'_0 C^{(1)}(k_0) C^{(2)}(k'_0) \\ &\times \frac{1}{2} \left[\hat{a}_{1,1,0}^\dagger(k_0) \hat{a}_{1,1,0}^\dagger(k'_0) + \hat{a}_{1,1,0}^\dagger(k_0) \hat{a}_{1,-1,0}^\dagger(k'_0) \right. \\ &\left. - \hat{a}_{1,-1,0}^\dagger(k_0) \hat{a}_{1,1,0}^\dagger(k'_0) - \hat{a}_{1,-1,0}^\dagger(k_0) \hat{a}_{1,-1,0}^\dagger(k'_0) \right] |\{0\}\rangle, \end{aligned} \quad (4.18)$$

which produces the coincidence detection probability in equation (4.9) when we detect coincidences between the two orthogonal LG modes ($\ell = \pm 1$), in the same path.

This calculation tells us that the unitary device which should produce bunching between orthogonal transverse spatial modes is a beamsplitter transformation between a pair of such modes. Due to its similarity with a beamsplitter, we will call such a device a modesplitter.

To produce two-photon interference between transverse spatial modes in **publication I**, we constructed a unitary device that performs a modesplitting

transformation between transverse spatial modes. We constructed this device using the MPLC scheme introduced in chapter 3. As an example, we could have used the unitary transformations displayed in figures 3.7 and 3.8, if we wanted to create a modesplitting transformation between the LG modes with OAM values ± 2 .

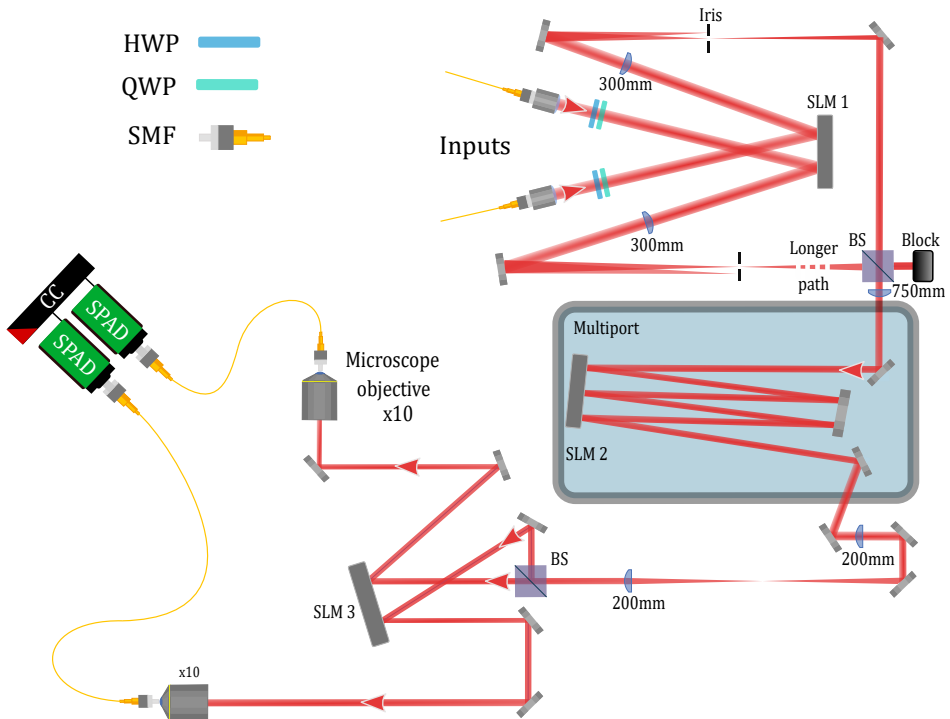


Figure 4.5 A drawing of the experimental setup. The photons are input into the system from the SMFs shown at the top of the figure and waveplates are used to orient their polarization to match the operating polarization of the first SLM. Amplitude and phase modulating masks are then used to shape the photons at separate regions of the first SLM, after which the first diffraction orders of the masks are selected using an iris in a 4f imaging system. The two photons are probabilistically overlapped to the same beam path using a beamsplitter, after which they are imaged onto the second SLM which performs the MPLC transformation. After the unitary transformation, the photons are imaged again and split from each other, probabilistically, with a second beamsplitter before they are directed onto a third SLM which performs a projective measurement on the photons with phase-flattening masks. The first diffraction orders of the measurement masks are then coupled into different SMFs, after which we post-select on two-photon coincidences using the same SPADs and coincidence counter introduced in chapter 3. Note that the “longer path” was added to emphasize the fact that the optical path lengths were roughly equal for both arms before the beamsplitter. The figure is adapted from the supplementary of **publication I** [198].

The first modesplitting transformation studied in **publication I** had a similar construction to the one in figure 3.8 but used the basis of LG modes with OAM values ± 1 . For such a device, when the two photons entering the MPLC device were indistinguishable from each other in every way besides the transverse structure, we should be able to measure two-photon bunching into the wanted spatial modes, which is visualized in figure 4.4.

It should be noted that a prior experiment achieved a similar effect by converting a polarization N00N state into a N00N state of so-called vector beams [29]. Vector beams have a spatially varying polarization structure in addition to a structured transverse profile. In contradistinction to an MPLC, the device utilized by the authors was a q-plate which limits the effect into a 2-dimensional subspace due to the involvement of polarization. It also restricts the space of transverse-spatial modes that can be used since it is a single-plane unitary device.

Experimental results

To experimentally test this bunching, we used the photon pair source introduced in chapter 3 and directed them through the two SMFs to the experimental setup shown in figure 4.5. The two photons were prepared in the two LG modes using the mode carving masks introduced in chapter 3. The measurement was performed by only modulating the phase structure of the photons. The initial measurements were done with the device performing the unitary described in equation (4.17) and visualized in figure 4.4. The results for two different projective measurements are shown in figure 4.6.

For the first two measurements we calculated visibilities of $(88.0 \pm 3.8)\%$, for the coincidences between orthogonal modes, and $(90.9 \pm 4.5)\%$ for coincidences within the same mode. Both of these measurements were also larger than the 50% visibility that is achievable for classical light fields prepared in a specific way [200–202]. However, as this 50% visibility bound is not accepted by everyone to be a sign of quantum behaviour [202], **publication I** also has measurements of the same interference in different MUBs. Observing the interference in different MUBs gives us a clear demonstration of quantum behaviour, as will be discussed in the next section. It should be noted that the error bars in figure 4.6 were calculated from only five repetitions of the measurement at

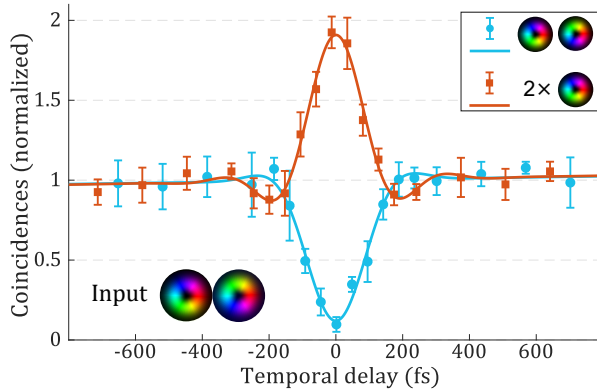


Figure 4.6 Plot showing the measurement data for the two initial measurements performed with a unitary modesplitter performing the transformation in equation (4.17). The two different plots are with the same pair of input modes shown in the lower left inset. A dip is shown for a projection onto the orthogonal pair of LG modes while a bump was measured for measurements projecting the photons onto the same mode. The legend shows the modes on which the pair of photons was projected. The error bars are standard deviations calculated from five repetitions at each point and the solid lines are fits of the form given in equation (4.14). The figure is adapted from **publication I**.

each position due to the system decoupling over time and the photon counts being comparatively low. As is detailed in the Supplementary material of **publication I** [198], we chose to show standard deviations of a limited number of measurements instead of the commonly shown Poissonian error estimates. We chose to do this because Poissonian errors represent a best-case scenario for our measurement errors and are much smaller for our data than the errors shown in figure 4.6. With Poissonian errors, we refer to the error estimate where the standard deviation is taken to be the square root of the number of detected events. The Poisson distribution gives us the best-case errors as it represents the expected distribution in the number of identical independent random events occurring within a fixed time interval [203], and already the statistics of our photon pair generation are well described by the Poisson process [149, 204]. Hence, any additional sources of error, such as experimental instability, would just add to the Poissonian errors in our system.

Besides the simple two-photon interference in the two-mode modesplitter, we also measured more complicated interference effects with different high-dimensional unitaries in **publication I**. Being able to change the unitary simply by changing the phase masks on our second SLM showcases the flexibility

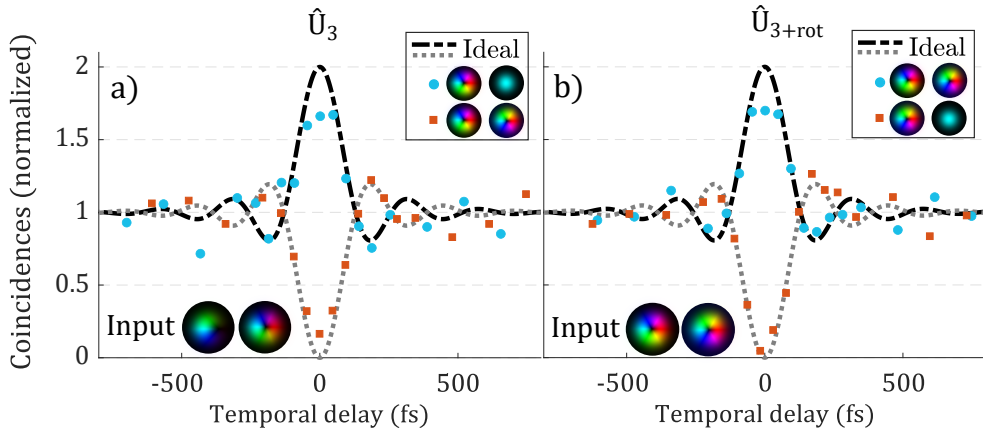


Figure 4.7 Measurements with (a) a balanced three-dimensional unitary sending each of the input LG modes ($\{\ell, p\} = \{-1, 0\}, \{0, 0\}, \{1, 0\}$) into a balanced superposition of the same modes. A superposition of these three LG modes is used as an input to induce anti-coalescence in one of the pairs of modes (blue dots) while a different pair of detected modes show coalescence (orange squares). In (b) the same effects are introduced by making the unitary unbalanced while using pure LG modes as inputs. The input modes are again shown in the bottom left corner and the legend shows the pair of modes the photons were projected on in the measurements. The error bars were omitted for clarity but can be found in the supplementary of **publication I** [198]. The ideal curves are theoretical curves calculated for the effects using the interference curve measured for the source, with the expected ideal visibility of the interference. The figure is a reprint of a figure in the supplementary of **publication I** [198].

of MPLC, although more phase manipulation planes would have been needed to produce better quality unitary transformations for larger mode sets. The flexibility in selecting the unitary is also shown in figure 4.7(b) where we were able to utilize the added number of modes to observe photon anti-coalescence between orthogonal modes while still observing bunching between a different pair of modes using the same inputs and unitary. In figure 4.7(a) we demonstrated the same effects using a three-dimensional beamsplitter-like unitary while structuring the input photons in a superposition that produced the same effect. This was done to additionally highlight the flexibility we have in creating complex superpositions of transverse spatial modes. Note that the error bars for the plots in figure 4.7 are shown in the supplementary material [198], along with the number of repetitions performed per each measurement.

Besides the measurements presented in this section, we also used the MPLC device to measure interference effects in higher-dimensional MUB transforma-

tion unitaries. This included a three-dimensional unitary and three different four-dimensional unitaries. These results can be found in **publication I**.

4.3 Creating N00N States Through Two-Photon Interference

As we saw already in equation (4.5), two-photon bunching in a balanced two-dimensional splitting unitary can create a two-photon N00N state between two orthogonal modes. Also, in section 2.3 we briefly discussed how N00N-states can be useful in metrological applications. Hence, creating N00N states between transverse spatial modes of light would be interesting for testing how the properties of spatial modes could be harnessed in different applications of the N00N states.

If we want to create transverse-spatial N00N states, however, we should have an efficient way of generating them since losses in such states are detrimental to the benefits such states offer [205]. In the setup given in figure 4.5, we already have too many losses from combining the two photons into the same beam path through a beamsplitter. Hence, if we wanted a principally lossless method of creating two-photon N00N states between transverse spatial modes, we would need to construct a two-mode multiplexer similar to the one shown in figure 3.9.

From the experiments presented in **publication I** we know that two-photon interference can be tuned using MPLC devices and we now know that MPLC multiplexers would be the optimal devices for creating two-photon N00N states between two transverse fields in the same beam path. What is left to do is to create transverse-spatial N00N states and see if they can be useful in any applications or fundamental studies. Since creating an MPLC system with SLMs is quite challenging and lossy, and we just wanted to create N00N states to utilize them in proof-of-principle experiments, we went with a different approach for creating N00N states in the next experiments.

The experimental system we built to test such N00N states had some similarities with the one presented in figure 4.5 and a simplified diagram of it is shown in figure 4.8. In this second setup, we perform the bunching into the wanted modes by already preparing the two photons in the required superpositions before combining them to the same beam path (a more detailed diagram of the experimental system can be found in the supplementary material of **pub-**

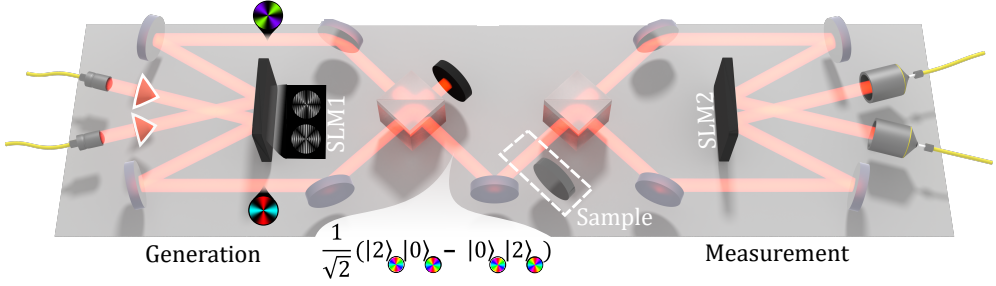


Figure 4.8 A simplified rendered image of the experimental system used in **publication II**. The two photons are again directed from the source using two SMFs and sent onto two separate sections of an SLM. The photons are independently structured into superpositions of OAM modes, as described in the main text, and combined into the same beam path using a beamsplitter. After being combined, the photons can bunch into the wanted transverse structures if they are temporally overlapped after the beamsplitter. The insets show an example of the SLM masks used to create a two-photon NOON state of idealized OAM modes with $\ell = \pm 2$ and a flat radial structure. A position is also shown where a single sample could be probed with this NOON state. However, note that no sample was used in the actual experiment and the effects of a possible sample were simulated using the final SLM. Finally, a second beamsplitter is used to probabilistically split the two photons into separate paths to again allow independent projections onto specific pairs of transverse structures using the methods described in chapter 3. A more detailed drawing of this experimental system can be found in the supplementary of **publication II** [206]. The figure is a reprint of a figure in **publication II**.

lication II [206]). How this method achieves bunching can be seen from the property of modes already introduced in equation 2.45 and hinted at in figure 4.4(a). Meaning that, if we prepare the two photons in a set of modes that can be written as orthogonal superpositions of the modes we want our photons to bunch into

$$\begin{aligned}\hat{a}_{s1}^\dagger(k_0) &= \frac{1}{\sqrt{2}} \left(\hat{a}_{1,10}^\dagger(k_0) - \hat{a}_{1,-10}^\dagger(k_0) \right) \\ \hat{a}_{s2}^\dagger(k_0) &= \frac{1}{\sqrt{2}} \left(\hat{a}_{1,10}^\dagger(k_0) + \hat{a}_{1,-10}^\dagger(k_0) \right),\end{aligned}\tag{4.19}$$

we should be able to achieve bunching by simply creating a separable two-photon state

$$|\Psi\rangle = |1\rangle_{s1,(1)} |1\rangle_{s2,(2)}\tag{4.20}$$

through independently structuring the two photons on an SLM. If we then overlap the two photons, e.g. by using the beamsplitter shown in figure 4.8, we should end up with the state shown in equation (4.18). Hence, due to

the two photons being in the same beam path, we can always find a basis where the two photons are separable. This is true even for a perfect two-photon N00N state between orthogonal transverse spatial modes which exhibit quantum correlations (this is also true for polarization [205]).

Before utilizing this method for testing properties of N00N states in **publications II** and **III**, we verified that this method is capable of producing a N00N state, by creating a two-photon N00N state between two OAM modes

$$|\Psi^{N00N}\rangle = \frac{1}{\sqrt{2}} (|2\rangle_\ell |0\rangle_{-\ell} - |0\rangle_\ell |2\rangle_{-\ell}). \quad (4.21)$$

The OAM modes we utilize here are just structures of light with identical uniform polarizations and well-defined azimuthal profiles. The radial and spectral structures can be arbitrary for these modes, as long as they are the same for both of the modes. One idealized example for such modes with OAM indices $\ell = \pm 2$ is shown in the insets of figure 4.8.

To quantify how good our N00N states are, we measure an entanglement witness value

$$\mathcal{W} = |\langle \hat{\sigma}_x \otimes \hat{\sigma}_x \rangle| + |\langle \hat{\sigma}_y \otimes \hat{\sigma}_y \rangle| + |\langle \hat{\sigma}_z \otimes \hat{\sigma}_z \rangle|. \quad (4.22)$$

This witness effectively verifies that we have correlations in all three MUBs of our two-dimensional space in comparison to the classical case where we can only have perfect correlations in one basis. Here $\hat{\sigma}_i$ are the Pauli operators for the two possible OAM modes of each photon. More details on how such entanglement witnesses are calculated can be found in reference [147]. For this entanglement witness, a perfect two-photon N00N state would produce a value $\mathcal{W} = 3$, while a perfectly correlated classical state can only produce a value of $\mathcal{W} = 1$. In **publication II** we measured the entanglement witness value for a N00N state, with OAM $\ell = \pm 1$, to be $\mathcal{W} = 2.92 \pm 0.02$ which is close to the maximal value 3. The error for our witness value was calculated through error propagation, starting from the standard deviation in our measurements of photon rates for each relevant measurement setting.

The entanglement witness measurement verifies that our N00N states are close to ideal. Hence, we can use the experimental system shown in figure 4.8 to investigate spatial mode N00N states in the next chapter. Before we do

that, however, we should address the fact that our two photons are seemingly entangled when they are in a N00N state. Although the measured quantum correlations seem to hint at this, it should be noted that this is only true in post-selection. This means that we can only get nonlocal quantum correlations for these transverse-spatial N00N states by splitting the two photons nondeterministically and post-selecting on cases where photons were separated. Hence, the two-photon transverse-spatial N00N state is not an entangled state in the traditional sense, due to the lack of nonlocality. The quantum correlations they exhibit are still very real, however, and lead to effects we utilize in the next two chapters.

5 METROLOGY WITH TRANSVERSE-SPATIAL N00N STATES

To test the usability of the transverse-spatial N00N states in metrological applications, we first need to identify which parameters such states are specifically suited for measuring. To get some insight into how we can determine this, we will spend the first part of this chapter looking into the concepts of Fisher information (FI) and quantum Fisher information (QFI). After exploring the different parameters that need to be optimized in creating a suitable probe state for a given parameter, we will look into the experimental demonstrations of parameter estimation with transverse-spatial N00N states given in **publications II** and **III**.

5.1 Fisher Information and Quantum Limits of Estimation

The field of metrology is full of mathematical tools and practices that help with estimating a set of parameters. For example, these tools can help with choosing optimal probes, optimizing the related measurements, or choosing an appropriate estimator for the parameter to extract the maximal amount of information from the measurement data. If one wants to get a more complete understanding of all of the nuances related to metrology, or photonic quantum metrology specifically, there is plenty of literature exploring the topics [127–129, 207]. Here we will only focus on a few concepts relating to the specific type of parameter estimation we are interested in; optimizing a quantum probe-state for single parameter estimation. To do this we will be looking at FI and QFI. We will mostly be following reference [128] to do this.

5.1.1 Fisher Information

The process of single-parameter estimation using quantum states of light can be broken down into five separate steps. First we need to prepare a specific probe state, then let the probe state interact with the system and encode information about the parameter (λ) to the probe state, extract the information from the state with a measurement, and finally, use an estimator to arrive at an estimate of the parameter λ . In actual applications of this process, multiple probe states are usually created and the final parameter estimate is calculated from this set of independent repetitions of the measurement. For now however, we will be focusing on a single predefined probe state which we will assume to be a pure quantum state $|\Psi^{probe}\rangle$. We will investigate what is the smallest possible measurement uncertainty we could achieve, in principle, with such a probe state. If we additionally fix the measurement of our probe state, we can use Fisher information to do exactly this.

In the context we have set here, Fisher information acts as a metric that can tell us how much information our measurement of the probe state can extract about a parameter λ . If our measurement is described as a POVM, effectively giving us a discrete set of possible measurement outcomes i for each probe state, the related FI can be calculated as

$$F(\lambda) = \sum_i \frac{1}{P(i|\lambda)} \left(\frac{\partial P(i|\lambda)}{\partial \lambda} \right)^2, \quad (5.1)$$

when $P(i|\lambda)$ is the probability of measurement outcome i conditioned on the value of the parameter λ . One important property of FI is that if we have ν independent probes that are measured the same way, independently of each other, the total Fisher information can be calculated as

$$F^{\text{tot}}(\lambda) = \sum_{j=1}^{\nu} F^{(j)}(\lambda), \quad (5.2)$$

where $F^{(j)}(\lambda)$ is the FI of the j^{th} probe. Another important property of the FI is that it can be used to calculate the best variance achievable using a fixed probe state, fixed measurement, and an arbitrary number of independent identical probes ν . This bound on the variance is called the Cramér-Rao bound

(CRB) and for locally unbiased estimators, it is of the form

$$\Delta\lambda^2 \geq \frac{1}{\nu F(\lambda)}. \quad (5.3)$$

If an estimator can reach this lowest possible uncertainty, it is called efficient.

5.1.2 Quantum Fisher Information

If we start again with a single parameter estimation process, with a fixed number of identical and independent probe states but do not fix the measurement, we can calculate the theoretically lowest possible CRB. This can be calculated using the QFI ($F_Q(\lambda)$) which maximizes the FI over all possible POVMs, giving us the quantum Cramér-Rao bound (QCRB)

$$\Delta\lambda^2 \geq \frac{1}{\nu F(\lambda)} \geq \frac{1}{\nu F_Q(\lambda)}. \quad (5.4)$$

To calculate the QFI in a more general case, one can look into references [127–129, 207]. For our purposes though, it is sufficient to limit ourselves to pure states while having the parameter λ be encoded by a unitary transformation. This means that our state undergoes a unitary evolution $\hat{U}_\lambda = e^{-i\lambda\hat{G}}$ where \hat{G} is a Hermitian operator called the generator of the unitary. Under these conditions, the QFI simplifies to

$$F_Q(\lambda; \psi) = 4\Delta^2\hat{G} = 4 \left(\langle \hat{G}^2 \rangle_\psi - \langle \hat{G} \rangle_\psi^2 \right), \quad (5.5)$$

where the expectation values are calculated for the initial probe state $|\psi\rangle$. This means that the best quantum states for estimating a specific parameter maximizes the variance of the generator of the unitary evolution that encodes the parameter λ . Additionally, pure probe states have a larger, or equally large, QFI compared to mixed states [128].

For experimental implementations, in addition to finding a probe state that can maximize the variance of the generator, we also need a POVM and an estimator to saturate the QCRB. For the case of single parameter estimation, it is theoretically possible to saturate the QCRB with a suitable measurement [128, 208]. As we will see in section 5.3 however, the physical implementation

of a measurement might not always be so straightforward.

5.1.3 Standard Quantum Limit and Heisenberg Limit

The final piece of our optimization puzzle is determining what probe states are the best for each single-parameter estimation task. This we can do by considering the QFI and QCRB for different input states. For more details on this, one can look, e.g., into reference [128]. However, for our purposes, it is sufficient to note that with more “classical” probe states, such as coherent states, parameter estimation in an interferometric scheme follows the standard quantum limit (SQL)

$$\Delta\lambda \geq \frac{1}{\sqrt{\nu N F_Q^{(1)}}}. \quad (5.6)$$

Here $F_Q^{(1)}$ is a constant dependent on the physical system, N is the number of photons in the probe state (the average number of photons for coherent states), and ν is again the number of repeated measurements with identical independent probe states. In the scaling shown in equation (5.6), the defining feature is that the minimum uncertainty scales with the square root of the total number of photons used in the estimation process $\Delta\lambda \propto 1/\sqrt{\nu \times N}$.

For N00N states, we have N photons in a state

$$|\Psi^{N00N}\rangle = \frac{1}{\sqrt{2}} \left(|N\rangle_{g_1} |0\rangle_{g_2} + e^{i\varphi} |0\rangle_{g_1} |N\rangle_{g_2} \right), \quad (5.7)$$

where φ is an arbitrary phase and the labels g_i denote eigenstates of the generator of the unitary \hat{G} . The generator and eigenstates are selected so that the relation $\hat{G} |N\rangle_{g_i} = N g_i |N\rangle_{g_i}$ holds. In such a case, our uncertainty scales as

$$\Delta\lambda \geq \frac{1}{\sqrt{\nu N} |g_1 - g_2|}. \quad (5.8)$$

This $\Delta\lambda \propto 1/N$ scaling is the ultimate limit on estimation precision called the Heisenberg Limit (HL). The value $|g_1 - g_2|$ in equation (5.8) comes from the variance of the generator

$$\Delta^2 \hat{G} = \frac{N^2}{4} (g_1 - g_2)^2. \quad (5.9)$$

Thus, with N00N states, we can reach the HL in estimating a single parameter λ , when the generator of the encoding unitary transformation has eigenstates of the form $\hat{G}|N\rangle_{g_i} = Ng_i|N\rangle_{g_i}$. If the set of eigenstates allows it, we can additionally improve the precision of our estimation by choosing modes with an extremely large difference in the values g_i .

5.2 Angular Superresolution with Orbital Angular Momentum N00N States

In **publication II** we used the theory presented in the previous sections to construct transverse-spatial N00N states for sensing rotations. By a rotation of a paraxial beam, we mean rotations around the optical axis, which happens to be the z -axis in our formalism. As is shown in standard quantum mechanics textbooks [115], the generator of rotation around an axis is the angular momentum operator in the direction of that axis. Hence, the unitary operator describing the evolution of our quantum state upon a rotation of ϕ is

$$\hat{U}_{\text{rot}} = e^{-i\frac{\hat{L}_z}{\hbar}\phi}, \quad (5.10)$$

where \hat{L}_z is the OAM operator given in equation (2.58) and we have ignored any effects rotation has on the polarization. Since LG mode Fock states are eigenstates of this generator, we know that having a N00N state between two LG modes as a probe state would give us an HL scaling in the uncertainty of the rotation angle. Specifically, if we choose a N00N state

$$|\Psi_\phi\rangle = \frac{1}{\sqrt{2}} (|N\rangle_{\ell_1} |0\rangle_{\ell_2} - |0\rangle_{\ell_1} |N\rangle_{\ell_2}), \quad (5.11)$$

where the two modes are in the same beam path and have an LG mode structure with $p = 0$ and $\ell = \ell_i$, we should be able to achieve a sensitivity scaling of

$$\Delta\phi \geq \frac{1}{|\ell_1 - \ell_2|N\sqrt{\nu}}, \quad (5.12)$$

according to equation (5.8). To achieve this scaling we define the OAM modes as

$$|1\rangle_{\ell_i} = \sum_{\sigma,p} \int_0^\infty dk_0 C_{\sigma,p}(k_0) \hat{a}_{\sigma,\ell_i,p}^\dagger(k_0) |\{0\}\rangle = \hat{a}_{\ell_i}^\dagger |\{0\}\rangle, \quad (5.13)$$

where every mode with an OAM index ℓ_i has an identical normalized spectrum, polarization, and the same weights on the radial indices

$$\sum_{\sigma,p} \int_0^\infty dk_0 |C_{\sigma,p}(k_0)|^2 = 1. \quad (5.14)$$

Using the mode in equation (5.13), we can also calculate the QCRB¹ directly through a calculation of the variance for the OAM operator using the relations

$$\hat{a}_{\sigma,\ell,p}(k_0) |N\rangle = f_{\sigma,\ell,p}(k_0) \hat{a} |N\rangle \quad \text{and} \quad \hat{a}_{\sigma,\ell,p}^\dagger(k_0) |N\rangle = f_{\sigma,\ell,p}^*(k_0) \hat{a}^\dagger |N\rangle, \quad (5.15)$$

where $f_{\sigma,\ell,p}(k_0)$ is an arbitrary normalized amplitude function and the operator \hat{a} is defined as

$$\hat{a} = \sum_{\sigma,\ell,p} \int_0^\infty dk_0 f_{\sigma,\ell,p}^*(k_0) \hat{a}_{\sigma,\ell,p}(k_0) \quad \text{with} \quad \sum_{\sigma,\ell,p} \int_0^\infty dk_0 |f_{\sigma,\ell,p}(k_0)|^2 = 1$$

and

$$|N\rangle = \frac{(\hat{a}^\dagger)^N}{\sqrt{N!}} |\{0\}\rangle. \quad (5.16)$$

The derivation of equations (5.15) can be done by following a similar derivation in reference [119].

The uncertainty in equation (5.12) can be minimized by choosing $\ell_2 = -\ell_1 = \ell > 0$ while maximizing the value of ℓ . Although the value of ℓ is unbounded in theory, the larger the value is, the larger the paraxial beam is going to be as well (when we keep the Gaussian radius $w(z)$ fixed). Hence, the maximum amount of OAM is limited by the aperture size of our system. Of course, we can reduce the Gaussian radius of our OAM modes to compensate for this but, at some point, we will reach a limit on the level of detail to which we can structure

¹Note that in the supplementary of **publication II** we also calculate this bound using a simplified notation where most other degrees of freedom are ignored by assuming arbitrary single modes with well defined OAM.

our light fields. In addition, light fields with such small details diverge rapidly, requiring small-scale custom optics to deal with. If we would go to small enough beam sizes, we would eventually reach the limit of paraxiality, requiring us to reformulate our theory [209, 210].

Experimental results

To experimentally verify this rotation sensitivity, in **publication II** we create single-photon and two-photon N00N states using the method described in section 4.3. The details of the two-photon experiment are explained in section 4.3 and, for the single-photon case, we simply used the same photon source to generate heralded single photons as is described in reference [142].

For the single-photon case, only one of the input and output fibres, shown in figure 4.8, were used. The other photon was sent to a detector immediately from the source. The data was then measured as coinciding detections between the two detectors while accounting for the delayed detection of the signal photon. The single-photon nature of our heralded single photons was quantified in our work [172] where a $g^2(0)$ value of 0.022 ± 0.003 was measured. This $g^2(0)$ value was measured for the same source with slightly different alignment and pump power, using the method described in reference [60].

In the rotation experiment, we effectively created different N00N states

$$|\Psi_\phi\rangle = \frac{1}{\sqrt{2}} (|N\rangle_\ell |0\rangle_{-\ell} - |0\rangle_\ell |N\rangle_{-\ell}), \quad (5.17)$$

with $N = \{1, 2\}$. Using the unitary operator describing the state evolution under rotation (see equation (5.10)), we expect the modes to evolve as

$$\hat{U}_{\text{rot}}^\dagger \hat{a}_{\ell_i}^\dagger \hat{U}_{\text{rot}} = e^{i\ell_i\phi} \hat{a}_{\ell_i}^\dagger, \quad (5.18)$$

which can be calculated using the Baker-Hausdorff lemma in equation (2.77). What equation (5.18) tells us is that a rotation around the optical axis corresponds simply to a global phase shift for a pure OAM mode. Linking the rotation to a phase shift gives us a more intuitive picture of why the OAM N00N state is a good probe state for estimating the rotation. The link is clearer if we remind ourselves of the increased phase sensitivity of N00N-state

interferometers discussed in section 2.3. Hence, by rotating a superposition of OAM modes, we effectively have a N00N-state interferometer in a single beam. Due to this mapping of rotation to phase shift, OAM modes have already been used in a few earlier theoretical and experimental studies looking into using different types of quantum states to measure such rotations [48–51]. The novel feature of the measurements presented here is the usage of a single-beam spatial mode N00N state which has the robustness and convenience of a single-beam operation.

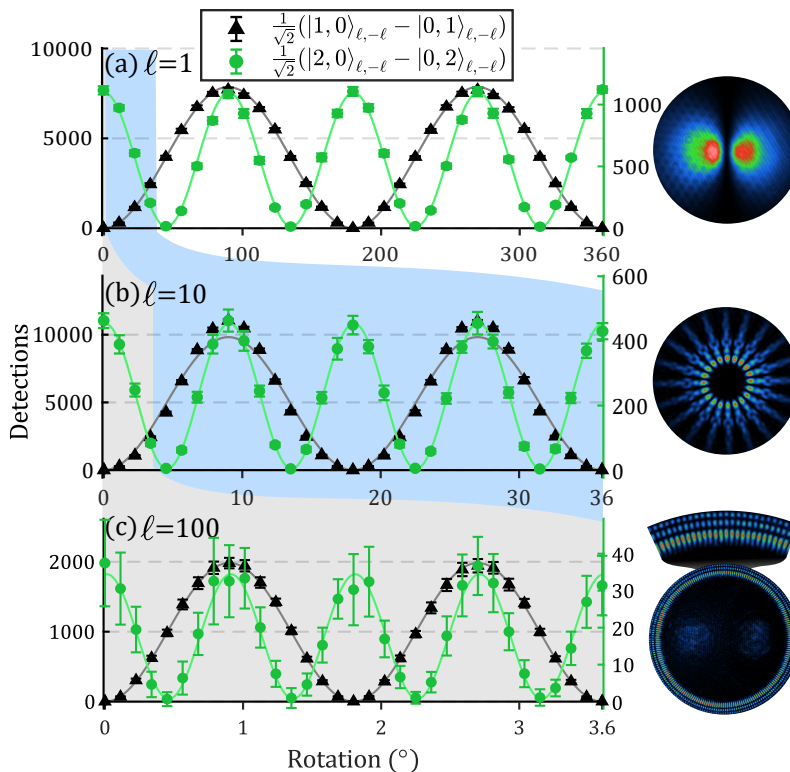


Figure 5.1 Measurement data from different OAM N00N states. The black triangles are single-photon N00N state measurements and the green dots are two-photon N00N state measurements. The solid lines are fits of the form shown in equation (5.19) and the images on the right side are false-colour camera images of the corresponding single-photon structures made visible with a laser. The error bars in the plots are standard deviations calculated from at least 19 repetitions of the measurement and accidental coincidences have been subtracted for the two-photon measurements. More details about the data can be found in **publication II**. The figure is a reprint of a figure in **publication II**.

In our measurements, we simulated a rotation of the beam by rotating the

measurement masks on our final SLM (shown in figure 4.8). Using the measurement masks we project the photons onto superpositions of the constituent OAM modes as described in **publication II**. The expected detection signal is of the form

$$\frac{R_A}{2} \left[1 - \cos \left(2N\ell \frac{\pi}{180^\circ} \phi - \theta_c \right) \right] + R_D, \quad (5.19)$$

an ideal version of which is calculated in the supplementary of **publication II** [206]. In the above equation, R_A and R_D are parameters effectively giving us the height of the fringes and the bottom of the fringes, and θ_c is a phase offset. The measurement data for N00N states with OAM values $\{\pm 1, \pm 10, \pm 100\}$ is shown in figure 5.1. From this data, we can clearly see the angular superresolution of OAM N00N states from the increased density of fringes with larger photon numbers.

In addition to the superresolution measurements, we also investigated the scaling in measurement sensitivity for our OAM N00N states and looked into whether they show this HL scaling or not when ignoring the losses in our experimental scheme. The details and result of this investigation can be found in **publication II**.

5.3 Longitudinal Superresolution with Radial Mode N00N States

Besides rotations, structured light fields can be used to measure other parameters as well. For spatial structuring, transverse displacement [54] and longitudinal displacements are the obvious choices. In **publication III** we focused on the latter one of these two, which in our specific case of paraxial modes, corresponds to measuring distances along the optical axis of the beam.

For translation along the optical axis, the generator of the unitary evolution is

$$-\frac{\hat{P}_z}{\hbar} = -\sum_{\sigma} \int d^2\mathbf{k}_{\perp} \int_0^{\infty} dk_0 k_z(\mathbf{k}_{\perp}, k_0) \hat{a}_{\sigma}^{\dagger}(\mathbf{k}_{\perp}, k_0) \hat{a}_{\sigma}(\mathbf{k}_{\perp}, k_0), \quad (5.20)$$

where we have chosen the negative sign to match the signs of the phase terms of the field (see equation (2.51)) and modified the momentum operators shown in references [94, 119] to fit our formalism. If we then restrict ourselves to transverse-spatial N00N states between two orthogonal modes labelled 1 and 2

$$|\Psi_z\rangle = \frac{1}{\sqrt{2}} (|N\rangle_1 |0\rangle_2 - |0\rangle_1 |N\rangle_2), \quad (5.21)$$

we can calculate the QFI for longitudinal translation, with any pair of modes, using

$$F_Q(z; \psi_z) = \frac{4}{\hbar^2} \Delta^2 \hat{P}_z \Big|_{\Psi_z}. \quad (5.22)$$

If the modes have the normalized structures

$$\begin{aligned} \hat{a}_1 &= \sum_{\sigma} \int_0^{\infty} dk_0 f_{\sigma}^*(\mathbf{k}_{\perp}, k_0) \hat{a}_{\sigma}(\mathbf{k}_{\perp}, k_0) \\ \hat{a}_2 &= \sum_{\sigma} \int_0^{\infty} dk_0 g_{\sigma}^*(\mathbf{k}_{\perp}, k_0) \hat{a}_{\sigma}(\mathbf{k}_{\perp}, k_0), \end{aligned} \quad (5.23)$$

we can use similar relations to the ones shown in equation (5.15) to calculate the QFI, while assuming that we have a single frequency and single polarization

$$\begin{aligned} |f_{\sigma}(\mathbf{k}_{\perp}, k_0)|^2 &\approx \delta_{\sigma,+1} \delta(k_0 - k_c) |f_1(\mathbf{k}_{\perp})|^2, \\ |g_{\sigma}(\mathbf{k}_{\perp}, k_0)|^2 &\approx \delta_{\sigma,+1} \delta(k_0 - k_c) |f_2(\mathbf{k}_{\perp})|^2. \end{aligned} \quad (5.24)$$

The momentum variance then takes the form

$$\Delta^2 \hat{P}_z \Big|_{\Psi_z} = \frac{\hbar^2}{4} \left[N^2 (\langle k_z \rangle_1 - \langle k_z \rangle_2)^2 + 2N (\Delta^2 k_z \Big|_1 + \Delta^2 k_z \Big|_2) \right]. \quad (5.25)$$

In the above equation, $\langle k_z^n \rangle_i$ is the n^{th} moment of k_z for mode i , which is calculated as

$$\langle k_z^n \rangle_i = \int d^2 \mathbf{k}_{\perp} k_z^n(\mathbf{k}_{\perp}, k_c) |f_i(\mathbf{k}_{\perp})|^2, \quad (5.26)$$

when $f_i(\mathbf{k}_{\perp})$ is the transverse field structure of the mode i (e.g. an LG or an HG mode).

From equation (5.25) we see that the first term is similar to the N00N-state QFI shown in equation (5.9), as it scales with N^2 . Hence, we can assume that such monochromatic transverse-spatial N00N states have the potential for quantum-enhanced measurement precision of longitudinal shifts as well. The only requirement we have is that the two orthogonal modes being occupied have different average momenta in the direction of the optical axis.

In the supplementary of **publication III** [143], R.F. Barros has calculated the QFI in the case where modes 1 and 2 are HG modes. These HG modes, as

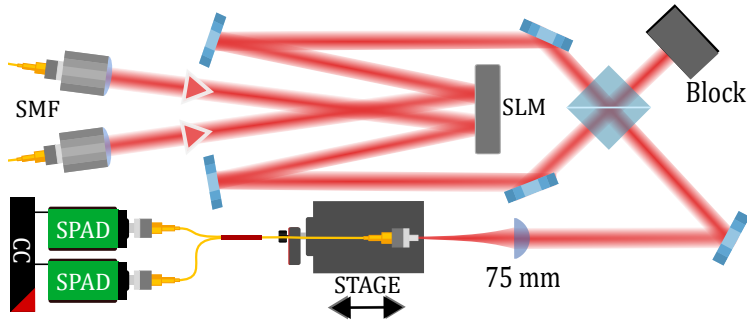


Figure 5.2 Simplified figure of the experimental setup utilized in **publication III**. The generation is done using the mode carving method described in chapter 3 and the photons are again combined in a beamsplitter to enable bunching. The measurement is done by coupling the two photons into an SMF after which we post-select for two photons coupling into the SMF at the same time using a fibre beamsplitter, two detectors, and a coincidence counter. The SMF is then scanned backwards through the focus to measure the signal at different points z . The figure is a reprint of a figure in **publication III**.

already mentioned in section 2.1.2, are paraxial modes with Cartesian symmetries and the QFI for these modes is of the form

$$F_Q(|\Psi_z\rangle) = \frac{N^2}{4} \frac{d}{dz} \Delta\Phi_G|_{z=0} + \frac{N}{4z_R^2} (M_1 + M'_1 + M_2 + M'_2), \quad (5.27)$$

where $M_i = n + m + 1$ is the mode order of mode i , $M'_i = n^2 + m^2 + 1$, and $\Delta\Phi_G|_{z=0}$ is the Gouy phase difference between the modes at the waist. The indices n and m define the structure of the HG modes (similarly to ℓ and p for LG modes), and $\Delta\Phi_G = (M_1 - M_2) \tan^{-1}(z/z_R)$. The derivative of the Gouy phase difference then gives us $\frac{d}{dz} \Delta\Phi_G|_{z=0} = (M_1 - M_2)/z_R$.

Equation (5.25) tells us that as the difference between the average momenta in the z -direction gets bigger, the amount of information encoded in our state increases. Equation (5.27) additionally tells us that for a monochromatic light field of HG modes having the same waist, this difference in average momenta corresponds to a mode order difference. That is, the larger the difference between the mode orders of the constituent modes, the more information about z is encoded into the state upon translation. When calculating equation (5.27) for LG modes [143], the first term is unaltered, and hence, we should also be able to observe some longitudinal superresolution using N00N states of LG modes.

To demonstrate this superresolution, we create transverse-spatial N00N states

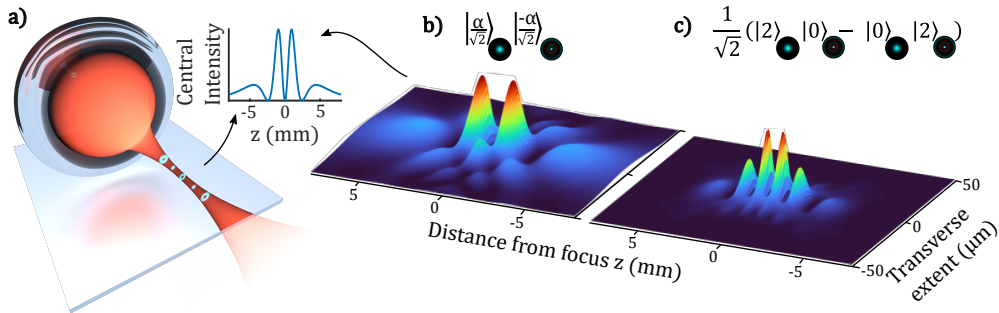


Figure 5.3 (a) contains a rendered image showing the concept of the experiment in **publication III**, where a changing intensity in the centre of the beam corresponds to interference due to the difference in the Gouy phases of the modes. The inset shows the central intensity of the beam. (b) shows the expected intensity and (c) a two-photon probability along a line containing the optical axis. The two-photon structure was made visible by post-selecting for the two photons existing at the same position, and it also shows an increased density of fringes at the centre of the beam. The figure is a reprint of a figure in **publication III**.

between radial modes, i.e., LG modes without any OAM. A simplified diagram of the experimental system is shown in figure 5.2. Devising a measurement capable of saturating this longitudinal QFI might be tricky since the physical size of the modes changes as they propagate. One option for a measurement might be a mode sorting of the Fourier transform of the beam as the momentum space structure of the modes does not change in size upon propagation (see equation (2.12)). However, such a projection would need to properly account for the position-dependent phase.

In our proof-of-principle experiment, we measured the two-photon N00N state by simply scanning an SMF through the focus of the N00N state. The radial modes were specifically chosen since the central intensity of these superposition structures interferes, resulting in a changing intensity at the centre of the beam, as is also visualized in figure 5.3.

We measured the interference signal first with a laser while only using one of the inputs. These measurement results are shown on the upper row of figure 5.4. The corresponding two-photon measurements are shown in the lower row of the same figure. By comparing the results, we see that the N00N states have an increased fringe spacing. The solid lines, in the plot, correspond to fits and more about the form of those fits can be found in **publication III**.

In both the case of rotational and longitudinal superresolution, we see that

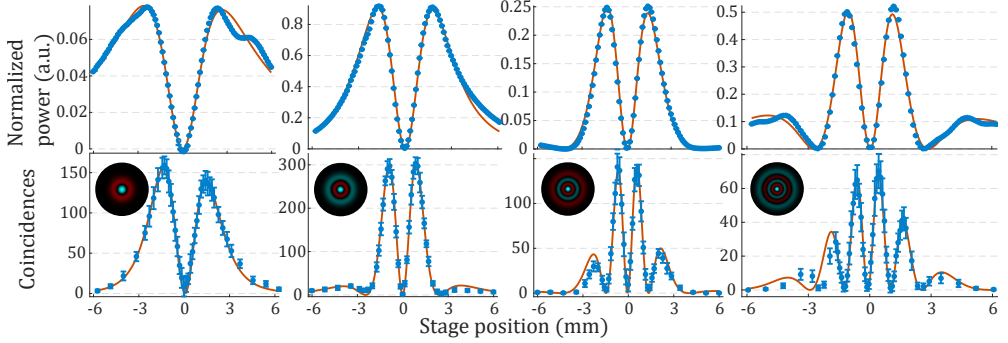


Figure 5.4 Measurement results from **publication III**. The upper row shows data measured with a laser in a superposition of a Gaussian beam and a higher-order radial mode. The insets of a mode in each column show the radial mode used in those measurements. The error bars are standard deviations and more information on the fits and measurements can be found in **publication III**. The lower row shows the corresponding two-photon N00N state measurements, with the same Gaussian and radial modes, with accidental detections removed. In the data, we see that the fringes are confined closer to the focus ($z = 0$) for the N00N states, with an increased number of fringes compared to the laser for $p = \{3, 4\}$. Also, as could be expected from equation (5.27), the fringes get denser with a larger mode order difference. The figure is a reprint of a figure in **publication III**.

we can engineer single beam quantum states of light that could, in principle, surpass the SQL scaling in parameter estimation. In both of these cases, it is important to create a large momentum difference between the two modes to increase the sensitivity. By analogy, if we would extend the presented method to measuring lateral displacements, we would need to create a N00N state between two field structures with a large difference in the transverse momentum. One example of such field structures is given in reference [54]. Additionally, for longitudinal superresolution, Bessel beams might be a better alternative to LG modes due to their momentum being well-defined along the optical axis [211].

Of course, in the case of longitudinal displacement, it would be better to induce wavelength scale phase differences as in a traditional interferometer. If we would like to increase the sensitivity while maintaining the single beamline operation, creating a N00N state between different wavelengths would be ideal. Nevertheless, the two experiments presented here demonstrate that we can engineer single beamline quantum states of light to measure different parameters with beyond SQL scaling.

6 PHOTON NUMBER STATES AND THE GOUY PHASE

Besides testing different metrological applications, we can use our transverse-spatial N00N states to investigate fundamental details about the nature of photons. In **publication III** we demonstrate this by measuring the Gouy phase of photon number states. Although one might simply assume that the phase sensitivity of Fock states extends to the Gouy phase, as it is such a central property of the modes, it is surprising that there seem to be no prior investigations into the Gouy phase of Fock states.

6.1 Propagation of N-photon Fock states

To start off with, we can use the translation unitary to calculate what we would expect the Gouy phase evolution of number states to be. Because this calculation is performed in the supplementary of **publication III** [143] using a slightly simplified formalism, we will repeat some of the steps here.

We can start with our photons occupying a mode corresponding to the creation operator

$$\hat{a}_i^\dagger(z=0) = \sum_{\sigma} \int_0^{\infty} dk_0 f_{\sigma}(k_0) \int d^2\mathbf{k}_{\perp} \mathcal{U}_{\ell_p}(\mathbf{k}_{\perp}) \hat{a}_{\sigma}^{\dagger}(\mathbf{k}_{\perp}, k_0), \quad (6.1)$$

where we have assumed that the transverse structure of our mode is an LG mode, at the waist position, and the spectral structure $f_{\sigma}(k_0)$ is assumed to be monochromatic with a single polarization. The evolution of each plane-wave component of our field can be calculated as

$$\hat{a}_{\sigma}^{\dagger}(\mathbf{k}_{\perp}, k_0, z) = e^{-i \frac{\hat{P}_z z}{\hbar}} \hat{a}_{\sigma}^{\dagger}(\mathbf{k}_{\perp}, k_0) e^{i \frac{\hat{P}_z z}{\hbar}} = e^{-i k_z(\mathbf{k}_{\perp}, k_0) z} \hat{a}_{\sigma}^{\dagger}(\mathbf{k}_{\perp}, k_0) \quad (6.2)$$

where we have used the definition in equation (5.20), the commutation relations in equation (2.56), and the Baker-Hausdorff lemma in equation (2.77). This gives us the translated mode

$$\hat{a}_i^\dagger(z) = \sum_{\sigma} \int_0^{\infty} dk_0 f_{\sigma}(k_0) \int d^2\mathbf{k}_{\perp} e^{-i k_z(\mathbf{k}_{\perp}, k_0)z} \mathcal{U}_{\ell p}(\mathbf{k}_{\perp}) \hat{a}_{\sigma}^{\dagger}(\mathbf{k}_{\perp}, k_0), \quad (6.3)$$

which we can restate using the relation in equation (2.62) as

$$\begin{aligned} \hat{a}_i^\dagger(z) &= \sum_{\sigma} \int_0^{\infty} dk_0 f_{\sigma}(k_0) \int d^2\mathbf{r}_{\perp} \hat{a}_{\sigma}^{\dagger}(\mathbf{r}_{\perp}, k_0) \\ &\quad \times \frac{1}{2\pi} \int d^2\mathbf{k}_{\perp} e^{i\mathbf{k}_{\perp} \cdot \mathbf{r}_{\perp}} e^{-i k_z(\mathbf{k}_{\perp}, k_0)z} \mathcal{U}_{\ell p}(\mathbf{k}_{\perp}) \end{aligned} \quad (6.4)$$

where the last integral corresponds exactly to the ASR propagation shown in equation (2.12), giving us

$$\hat{a}_i^\dagger(z) = \sum_{\sigma} \int_0^{\infty} dk_0 f_{\sigma}(k_0) e^{-i k_0 z} \int d^2\mathbf{r}_{\perp} u_{\ell p}(\mathbf{r}_{\perp}, -z; k_0) \hat{a}_{\sigma}^{\dagger}(\mathbf{r}_{\perp}, k_0) \quad (6.5)$$

We can now define a slightly adjusted form of an LG mode which does not have the Gouy phase ($\Phi_G(z; k_0) = (2p + |\ell| + 1) \tan^{-1}(z/z_R)$) but includes the plane wave phase

$$u'_{\ell p}(\mathbf{r}_{\perp}, -z; k_0) = u_{\ell p}(\mathbf{r}_{\perp}, -z; k_0) e^{-i k_0 z} e^{i \Phi_G(-z; k_0)}, \quad (6.6)$$

giving us modes

$$\begin{aligned} \hat{a}_i^\dagger(z) &= \sum_{\sigma} \int_0^{\infty} dk_0 f_{\sigma}(k_0) e^{-i \Phi_G(-z; k_0)} \int d^2\mathbf{r}_{\perp} u'_{\ell p}(\mathbf{r}_{\perp}, -z; k_0) \hat{a}_{\sigma}^{\dagger}(\mathbf{k}_{\perp}, k_0) \\ &\approx e^{-i \Phi_G(-z; k_0)} \hat{a}_i^{\dagger'}(z), \end{aligned} \quad (6.7)$$

where we have used the assumption that the mode is monochromatic, allowing us to separate a constant Gouy phase term from the mode $\hat{a}_i^{\dagger'}(z)$.

What the above derivation allows us to do is to describe the Fock state evolution upon translation. That is, if we have N photons occupying the mode in equation (6.1) and propagate it from $z = 0$ to an arbitrary position z , we

can state the Fock state as

$$\begin{aligned}
 |N\rangle_i &= \frac{\left(\hat{a}_i^\dagger(0)\right)^N}{\sqrt{N!}} |\{0\}\rangle \longrightarrow \frac{e^{-iN\Phi_G(-z;k_0)} \left(\hat{a}'_i(z)\right)^N}{\sqrt{N!}} |\{0\}\rangle \\
 &= e^{-iN\Phi_G(-z;k_0)} |N\rangle_{i',z}.
 \end{aligned} \tag{6.8}$$

What this result tells us is that the N -photon Fock state does evolve with an increased Gouy phase and we just need to project on the correct state to see its effects. It turns out that one such measurement scenario is the one presented in section 5.3, and the measurement results in figure 5.4 confirm this experimentally. More information on this can be found in **publication III**.

6.2 Implications of the N -photon Gouy phase

Besides confirming that the Gouy phase of N photons differs from the Gouy phase of single photons [100, 212] and classical waves, in **publication III** we additionally investigated the implications of the N photon Gouy phase. Specifically, we first looked into how this Gouy phase fits in with the so-called effective de Broglie wavelength of N photons. We additionally investigated if it fits into the framework of any of the multiple physical and mathematical interpretations of the classical Gouy phase [213–221].

The effective de Broglie wavelength of light is usually used in the context of interference of multi-photon quantum states and it ascribes an effective wavelength of λ/N for N -photons occupying the same mode with wavelength λ . Sometimes in discussions, this concept is taken as far as to mean that N -photon Fock states evolve identically to a classical mode with a shorter wavelength. Although this gives an accurate image of the Fock state evolution in some cases, e.g. for the free-space plane-wave phase e^{ik_0z} [222–224], it does not give us the full picture. One such case where the effective de Broglie wavelength doesn't reproduce the same effect as true Fock state evolution is when it comes to the Gouy phase. This difference is described in detail in **publication III** and in the news and views article in reference [225].

As for linking the N -photon Gouy phase to the different interpretations of the Gouy phase, we found that by using the momentum spread in equation (5.25), we can link the N -photon Gouy phase to the uncertainty interpre-

tation of the Gouy phase [215]. In simple terms, this interpretation says that a larger spread in transverse momentum should correspond to a larger Gouy phase shift that evolves faster around the focus. For monochromatic fields, the spread in transverse momentum is directly linked to the spread in longitudinal momentum. Hence, our QFI calculations in section 5.3 show that the faster Gouy phase change of Fock states in section 6.1 is accompanied by a larger spread in transverse-momentum, as is required by the uncertainty interpretation [215]. However, our investigation in **publication III** did not look into whether the momentum uncertainty of equation (5.25) could be used to calculate the Gouy phase evolution of Fock states, as is done for the classical Gouy phase in reference [215].

7 CONCLUSION AND OUTLOOK

In this thesis, we first derived a theoretical representation of quantized paraxial light fields, with the goal of explaining the theoretical and experimental background of the published works attached to the end of this thesis. Afterwards, we explored more details behind the experiments performed in this thesis and discussed some of the implications of these results. The three publications this thesis is built around explored the interference of two photons in the transverse-spatial degree of freedom. We restricted ourselves to the set of paraxial LG modes but the formalism and effects of this thesis are not restricted to these sets of modes or only two photons.

The thesis work builds upon the long line of works investigating interference of multiple-photons [5, 22], by first utilizing a relatively new tool in optics, i.e. MPLC devices, to induce different quantum interference effects of two-photons in the high-dimensional state space of transverse spatial modes. This work highlights the flexibility that MPLC provides for engineering different multi-photon interference effects through custom-made unitaries. These unitaries are, in principle, capable of performing an arbitrary linear optical transformation for an arbitrarily large set of modes. Of course, these theoretically limitless options are limited by some of the physical realities discussed in this thesis, such as the lossiness of the physical implementations or the restrictions caused by limited aperture and pixel sizes. Nevertheless, the experiment performed in **publication I** is a part of the first steps required in bringing the MPLC method into the quantum domain.

Besides using complicated inverse-design methods to engineer transverse-spatial quantum states, our work in **publication II** additionally highlighted a much simpler method of creating such states. This was done by simply performing the required structuring of the photons separately, before bringing them to interfere in the same beam path. We were able to use the method to generate

high-quality two-photon N00N states and the method could also be scaled to other quantum states with a larger number of photons. One straightforward example of such an extension to N photons is the creation of Holland-Burnett states which can also beat the SQL in metrological applications [226]. However, this scaling in photon number presents other difficulties such as the increased losses of a probabilistic system. Although the losses caused by post-selection might be tolerable in proof-of-principle experiments with a few photons, larger photon numbers would require a more efficient system if a single-beam quantum state is required. One example of such a device would be the aforementioned deterministic spatial-mode multiplexer.

As far as we are aware, **publication II** shows the first instance of this simple method for two-photon bunching in the transverse spatial domain. However, the effect itself is quite fundamental and might have been used before as a part of a more complicated quantum state engineering experiment.

Finally, we applied the transverse-spatial N00N states to different proof-of-principle applications. The first of these was to demonstrate that we can use the tools of quantum metrology to engineer quantum states for single parameter estimation tasks. In **publication II** we demonstrated this for rotation sensing and in **publication III** we extended it to longitudinal displacement measurements using a single beam. Although the second one of these does not have a clear measurement scheme for achieving supersensitive parameter estimation, even with future technologies, the experiments demonstrate a possible future application of quantum state engineering using transverse-spatially structured photons. In addition to these metrological applications, in **publication III** we showed how investigating such quantum states can give us new perspectives into physical systems and phenomena. Specifically, we were able to give a concrete example of how the concept of effective de Broglie wavelength breaks down when it comes to the fundamental wave property of the Gouy phase in paraxial beams. The same measurements also showed a link to a specific physical interpretation of the Gouy phase effect [215], hinting at a possibility of extending the interpretation to quantum states.

7.1 Outlook

Since this thesis work includes novel methods of shaping quantum light, it will be interesting to see how the methods are utilized and built upon. Hence, here we will briefly list some possible future research applications of the methods presented here.

To start off with, the unitary devices of **publication I** could find use in experiments performing some quantum information processing tasks, as the method can be used to create quantum gates [66]. Besides applications in quantum information, the MPLC system has already been extended into devices that can shape the spatiotemporal structure of a vectorial light field [227]. Extending such shaping techniques to quantum light might enable the generation of novel types of structured quantum states. Including the spectral/temporal and polarization degrees of freedom would increase the dimensionality of the state space and introduce novel properties for metrological applications. One might be able to then additionally combine different degrees of freedom to achieve a combined effect in parameter estimation, similarly to the combination of OAM and SAM in reference [50].

We also anticipate that the unitary MPLC devices and the simplified quantum state engineering method introduced in **publication II** will be useful in simulating different systems or testing different measurement schemes in the high-dimensional state space of transverse spatial modes. One example of such an application is already investigated in reference [228]. Additionally, the mode and photon number-dependent nature of the Gouy phase, explored in **publication III**, might open up interesting possibilities in the future. Especially since it should extend beyond photonic systems and should occur in any bosonic system with focused wave dynamics.

Finally, this thesis work outlines a theoretical formalism for operating with photon number quantum states of paraxial beams and includes experiments utilizing some very fundamental features of photons. Hence, we hope that our work can help anyone wanting to learn more about the fundamental properties, possibilities, and limitations of quantized paraxial fields of light in linear optics.

REFERENCES

- [1] T. Young. *A course of lectures on natural philosophy and the mechanical arts*. Vol. 1. London, Printed for J. Johnson, 1807, pp. 464–465. DOI: 10.5962/bhl.title.22458.
- [2] J.C. Maxwell. “A Dynamical Theory of the Electromagnetic Field”. In: *Philosophical Transactions of the Royal Society of London, vol.155* (1865), pp. 459–505. URL: www.jstor.org/stable/108892.
- [3] A. Einstein. “Über einen die Erzeugung und Verwandlung des Lichtes betreffenden heuristischen Gesichtspunkt”. In: *Annalen der Physik* 322.6 (1905), pp. 132–148. DOI: 10.1002/andp.19053220607.
- [4] P.A.M. Dirac. *The principles of quantum mechanics*. 3rd edition. Oxford university press, 1947, p. 9.
- [5] Z.Y. Ou. *Multi-Photon Quantum Interference*. New York, NY: Springer, 2007. ISBN: 038725532X.
- [6] G. Magyar and L. Mandel. “Interference fringes produced by superposition of two independent maser light beams”. In: *Nature* 198 (1963), pp. 255–256. DOI: 10.1038/198255a0.
- [7] R.L. Pfleegor and L. Mandel. “Interference effects at the single photon level”. In: *Physics Letters A* 24.13 (1967), pp. 766–767. DOI: 10.1016/0375-9601(67)90259-9.
- [8] R.L. Pfleegor and L. Mandel. “Interference of Independent Photon Beams”. In: *Physical Review* 159 (5 1967), pp. 1084–1088. DOI: 10.1103/PhysRev.159.1084.
- [9] R.L. Pfleegor and L. Mandel. “Further Experiments on Interference of Independent Photon Beams at Low Light Levels*†”. In: *Journal of the Optical Society of America* 58.7 (1968), pp. 946–950. DOI: 10.1364/JOSA.58.000946.

- [10] U. Fano. “Quantum Theory of Interference Effects in the Mixing of Light from Phase-Independent Sources”. In: *American Journal of Physics* 29.8 (1961), pp. 539–545. DOI: 10.1119/1.1937827.
- [11] L. Mandel. “Photon interference and correlation effects produced by independent quantum sources”. In: *Physical Review A* 28 (1983), pp. 929–943. DOI: 10.1103/PhysRevA.28.929.
- [12] R. Ghosh et al. “Interference of two photons in parametric down conversion”. In: *Physical Review A* 34 (5 1986), pp. 3962–3968. DOI: 10.1103/PhysRevA.34.3962.
- [13] R. Ghosh and L. Mandel. “Observation of nonclassical effects in the interference of two photons”. In: *Physical Review Letters* 59 (17 1987), pp. 1903–1905. DOI: 10.1103/PhysRevLett.59.1903.
- [14] P. Grangier, G. Roger, and A. Aspect. “Experimental Evidence for a Photon Anticorrelation Effect on a Beam Splitter: A New Light on Single-Photon Interferences”. In: *Europhysics Letters* 1.4 (1986), p. 173. DOI: 10.1209/0295-5075/1/4/004.
- [15] J.F. Clauser et al. “Proposed Experiment to Test Local Hidden-Variable Theories”. In: *Physical Review Letters* 23 (1969), pp. 880–884. DOI: 10.1103/PhysRevLett.23.880.
- [16] S.J. Freedman and J.F. Clauser. “Experimental Test of Local Hidden-Variable Theories”. In: *Physical Review Letters* 28 (1972), pp. 938–941. DOI: 10.1103/PhysRevLett.28.938.
- [17] J.F. Clauser. “Experimental Limitations to the Validity of Semiclassical Radiation Theories”. In: *Physical Review A* 6 (1972), pp. 49–54. DOI: 10.1103/PhysRevA.6.49.
- [18] A. Aspect, P. Grangier, and G. Roger. “Experimental Tests of Realistic Local Theories via Bell’s Theorem”. In: *Physical Review Letters* 47 (1981), pp. 460–463. DOI: 10.1103/PhysRevLett.47.460.
- [19] C.K. Hong, Z.Y. Ou, and L. Mandel. “Measurement of subpicosecond time intervals between two photons by interference”. In: *Physical Review Letters* 59 (18 1987), pp. 2044–2046. DOI: 10.1103/PhysRevLett.59.2044.

- [20] Y. H. Shih and C.O. Alley. “New Type of Einstein-Podolsky-Rosen-Bohm Experiment Using Pairs of Light Quanta Produced by Optical Parametric Down Conversion”. In: *Physical Review Letters* 61 (26 1988), pp. 2921–2924. DOI: 10.1103/PhysRevLett.61.2921.
- [21] J.G. Rarity and P.R. Tapster. “Fourth-order interference in parametric downconversion”. In: *Journal of the Optical Society of America B* 6.6 (1989), pp. 1221–1226. DOI: 10.1364/JOSAB.6.001221.
- [22] F. Bouchard et al. “Two-photon interference: the Hong–Ou–Mandel effect”. In: *Reports on Progress in Physics* 84.1 (2020), p. 012402. DOI: 10.1088/1361-6633/abcd7a.
- [23] B. P. Abbott et al. “Observation of Gravitational Waves from a Binary Black Hole Merger”. In: *Physical Review Letters* 116 (6 2016), p. 061102. DOI: 10.1103/PhysRevLett.116.061102.
- [24] E. Knill, R. Laflamme, and G.J. Milburn. “A scheme for efficient quantum computation with linear optics”. In: *Nature* 409 (2001), pp. 46–52. DOI: 10.1038/35051009.
- [25] J.-W. Pan et al. “Experimental Entanglement Swapping: Entangling Photons That Never Interacted”. In: *Physical Review Letters* 80 (1998), pp. 3891–3894. DOI: 10.1103/PhysRevLett.80.3891.
- [26] D. Branning et al. “Engineering the Indistinguishability and Entanglement of Two Photons”. In: *Physical Review Letters* 83 (1999), pp. 955–958. DOI: 10.1103/PhysRevLett.83.955.
- [27] T. Kobayashi et al. “Frequency-domain Hong–Ou–Mandel interference”. In: *Nature Photonics* 10 (2016), pp. 441–444. DOI: 10.1038/nphoton.2016.74.
- [28] A. Mohanty et al. “Quantum interference between transverse spatial waveguide modes”. In: *Nature Communications* 8.1 (2017), p. 14010. DOI: 10.1038/ncomms14010.
- [29] V. D’Ambrosio et al. “Tunable Two-Photon Quantum Interference of Structured Light”. In: *Physical Review Letters* 122 (1 2019), p. 013601. DOI: 10.1103/PhysRevLett.122.013601.

- [30] S. Leedumrongwatthanakun et al. “Programmable linear quantum networks with a multimode fibre”. In: *Nature Photonics* 14.3 (2020), pp. 139–142. DOI: 10.1038/s41566-019-0553-9.
- [31] C. Esposito et al. “Quantum walks of two correlated photons in a 2D synthetic lattice”. In: *npj Quantum Information* 8 (2022), p. 34. DOI: 10.1038/s41534-022-00544-09.
- [32] Adrian Makowski et al. *Large Reconfigurable Quantum Circuits with SPAD Arrays and Multimode Fibers*. 2023. arXiv: 2305.16206 [quant-ph].
- [33] L. Allen et al. “Orbital angular momentum of light and the transformation of Laguerre-Gaussian laser modes”. In: *Physical Review A* 45 (1992), pp. 8185–8189. DOI: 10.1103/PhysRevA.45.8185.
- [34] H. He et al. “Direct Observation of Transfer of Angular Momentum to Absorptive Particles from a Laser Beam with a Phase Singularity”. In: *Physical Review Letters* 75 (1995), pp. 826–829. DOI: 10.1103/PhysRevLett.75.826.
- [35] M.E.J. Friese et al. “Optical angular-momentum transfer to trapped absorbing particles”. In: *Physical Review A* 54 (2 1996), pp. 1593–1596. DOI: 10.1103/PhysRevA.54.1593.
- [36] N.B. Simpson et al. “Mechanical equivalence of spin and orbital angular momentum of light: an optical spanner”. In: *Optics Letters* 22.1 (1997), pp. 52–54. DOI: 10.1364/OL.22.000052.
- [37] L. Paterson et al. “Controlled Rotation of Optically Trapped Microscopic Particles”. In: *Science* 292.5518 (2001), pp. 912–914. DOI: 10.1126/science.1058591.
- [38] M.P. MacDonald et al. “Creation and Manipulation of Three-Dimensional Optically Trapped Structures”. In: *Science* 296.5570 (2002), pp. 1101–1103. DOI: 10.1126/science.1069571.
- [39] D.G Grier. “A revolution in optical manipulation”. In: *Nature* 424 (2003), pp. 810–816. DOI: 10.1038/nature01935.
- [40] M. Padgett and R Bowman. “Tweezers with a twist”. In: *Nature Photonics* 5 (2011), pp. 343–348. DOI: 10.1038/nphoton.2011.81.

- [41] F. Cardano et al. “Quantum walks and wavepacket dynamics on a lattice with twisted photons”. In: *Science Advances* 1.2 (2015), e1500087. DOI: 10.1126/sciadv.1500087.
- [42] G. Molina-Terriza, J.P. Torres, and L. Torner. “Twisted photons”. In: *Nature Physics* 3 (2007), pp. 305–310. DOI: 10.1038/nphys607.
- [43] M. Erhard et al. “Twisted photons: new quantum perspectives in high dimensions”. In: *Light: Science & Applications* 7 (2018), p. 17146. DOI: 10.1038/lsa.2017.146.
- [44] M. Tsang, R. Nair, and X.-M. Lu. “Quantum Theory of Superresolution for Two Incoherent Optical Point Sources”. In: *Physical Review X* 6 (3 2016), p. 031033. DOI: 10.1103/PhysRevX.6.031033.
- [45] F. Yang et al. “Far-field linear optical superresolution via heterodyne detection in a higher-order local oscillator mode”. In: *Optica* 3.10 (2016), pp. 1148–1152. DOI: 10.1364/OPTICA.3.001148.
- [46] Z. Yu and S. Prasad. “Quantum Limited Superresolution of an Incoherent Source Pair in Three Dimensions”. In: *Physical Review Letters* 121 (18 2018), p. 180504. DOI: 10.1103/PhysRevLett.121.180504.
- [47] Y. Zhou et al. “Quantum-limited estimation of the axial separation of two incoherent point sources”. In: *Optica* 6 (2019), pp. 534–541. DOI: 10.1364/OPTICA.6.000534.
- [48] A.K. Jha, G.S. Agarwal, and R.W. Boyd. “Supersensitive measurement of angular displacements using entangled photons”. In: *Physical Review A* 83 (5 2011), p. 053829. DOI: 10.1103/PhysRevA.83.053829.
- [49] R. Fickler et al. “Quantum Entanglement of High Angular Momenta”. In: *Science* 338.6107 (2012), pp. 640–643. DOI: 10.1126/science.1227193.
- [50] V. D’Ambrosio et al. “Photonic polarization gears for ultra-sensitive angular measurements”. In: *Nature Communications* 4.1 (2013), p. 2432. DOI: 10.1038/ncomms3432.
- [51] K. Liu et al. “Squeezing-enhanced rotating-angle measurement beyond the quantum limit”. In: *Applied Physics Letters* 113.26 (2018), p. 261103. DOI: 10.1063/1.5066028.

- [52] N. Treps et al. “Surpassing the Standard Quantum Limit for Optical Imaging Using Nonclassical Multimode Light”. In: *Physical Review Letters* 88 (20 2002), p. 203601. DOI: 10.1103/PhysRevLett.88.203601.
- [53] N. Tischler et al. “All-Optical Self-Referenced Transverse Position Sensing with Subnanometer Precision”. In: *ACS Photonics* 5.9 (2018), pp. 3628–3633. DOI: 10.1021/acsphotonics.8b00532.
- [54] R. Barboza et al. “Ultra-sensitive measurement of transverse displacements with linear photonic gears”. In: *Nature Communications* 13.1 (2022), p. 1080. DOI: 10.1038/s41467-022-28700-2.
- [55] S. Gröblacher et al. “Experimental quantum cryptography with qutrits”. In: *New Journal of Physics* 8.5 (2006), p. 75. DOI: 10.1088/1367-2630/8/5/075.
- [56] G. Vallone et al. “Free-Space Quantum Key Distribution by Rotation-Invariant Twisted Photons”. In: *Physical Review Letters* 113 (6 2014), p. 060503. DOI: 10.1103/PhysRevLett.113.060503.
- [57] M. Krenn et al. “Twisted photon entanglement through turbulent air across Vienna”. In: *Proceedings of the National Academy of Sciences* 112.46 (2015), pp. 14197–14201. DOI: 10.1073/pnas.1517574112.
- [58] M. Mirhosseini et al. “High-dimensional quantum cryptography with twisted light”. In: *New Journal of Physics* 17.3 (2015), p. 033033. DOI: 10.1088/1367-2630/17/3/033033.
- [59] A. Sit et al. “High-dimensional intracity quantum cryptography with structured photons”. In: *Optica* 4.9 (2017), pp. 1006–1010. DOI: 10.1364/OPTICA.4.001006.
- [60] F. Bouchard et al. “Experimental investigation of high-dimensional quantum key distribution protocols with twisted photons”. In: *Quantum* 2 (2018), p. 111. DOI: 10.22331/q-2018-12-04-111.
- [61] D. Cozzolino et al. “Orbital Angular Momentum States Enabling Fiber-based High-dimensional Quantum Communication”. In: *Physical Review Applied* 11 (6 2019), p. 064058. DOI: 10.1103/PhysRevApplied.11.064058.

- [62] H. Cao et al. “Distribution of high-dimensional orbital angular momentum entanglement over a 1 km few-mode fiber”. In: *Optica* 7.3 (2020), pp. 232–237. DOI: 10.1364/OPTICA.381403.
- [63] A.N. de Oliveira, S.P. Walborn, and C.H. Monken. “Implementing the Deutsch algorithm with polarization and transverse spatial modes”. In: *Journal of Optics B: Quantum and Semiclassical Optics* 7.9 (2005), p. 288. DOI: 10.1088/1464-4266/7/9/009.
- [64] A. Babazadeh et al. “High-Dimensional Single-Photon Quantum Gates: Concepts and Experiments”. In: *Physical Review Letters* 119 (18 2017), p. 180510. DOI: 10.1103/PhysRevLett.119.180510.
- [65] X. Gao et al. “Arbitrary d -dimensional Pauli X gates of a flying qudit”. In: *Physical Review A* 99 (2 2019), p. 023825. DOI: 10.1103/PhysRevA.99.023825.
- [66] F. Brandt et al. “High-dimensional quantum gates using full-field spatial modes of photons”. In: *Optica* 7.2 (2020), pp. 98–107. DOI: 10.1364/OPTICA.375875.
- [67] X. Gao et al. “Computer-Inspired Concept for High-Dimensional Multipartite Quantum Gates”. In: *Physical Review Letters* 125 (5 2020), p. 050501. DOI: 10.1103/PhysRevLett.125.050501.
- [68] S. Ru et al. “Realization of a deterministic quantum Toffoli gate with a single photon”. In: *Physical Review A* 103 (2 2021), p. 022606. DOI: 10.1103/PhysRevA.103.022606.
- [69] S. Goel et al. *Inverse-design of high-dimensional quantum optical circuits in a complex medium*. 2022. DOI: 10.48550/ARXIV.2204.00578.
- [70] Y. Wang et al. “Qudits and High-Dimensional Quantum Computing”. In: *Frontiers in Physics* 8 (2020). DOI: 10.3389/fphy.2020.589504.
- [71] H. Bechmann-Pasquinucci and W. Tittel. “Quantum cryptography using larger alphabets”. In: *Physical Review A* 61 (6 2000), p. 062308. DOI: 10.1103/PhysRevA.61.062308.
- [72] N.J. Cerf et al. “Security of Quantum Key Distribution Using d -Level Systems”. In: *Physical Review Letters* 88 (12 2002), p. 127902. DOI: 10.1103/PhysRevLett.88.127902.

- [73] S. Ecker et al. “Overcoming Noise in Entanglement Distribution”. In: *Physical Review X* 9 (4 2019), p. 041042. DOI: 10.1103/PhysRevX.9.041042.
- [74] T.C. Ralph, K.J. Resch, and A. Gilchrist. “Efficient Toffoli gates using qudits”. In: *Physical Review A* 75 (2 2007), p. 022313. DOI: 10.1103/PhysRevA.75.022313.
- [75] B.P. Lanyon et al. “Simplifying quantum logic using higher-dimensional Hilbert spaces”. In: *Nature Physics* 5.2 (2009), pp. 134–140. DOI: 10.1038/nphys1150.
- [76] S. Ramelow et al. “Discrete Tunable Color Entanglement”. In: *Physical Review Letters* 103 (25 2009), p. 253601. DOI: 10.1103/PhysRevLett.103.253601.
- [77] B. Brecht et al. “Photon Temporal Modes: A Complete Framework for Quantum Information Science”. In: *Physical Review X* 5 (4 2015), p. 041017. DOI: 10.1103/PhysRevX.5.041017.
- [78] N. Herrera Valencia et al. “High-Dimensional Pixel Entanglement: Efficient Generation and Certification”. In: *Quantum* 4 (2020), p. 376. DOI: 10.22331/q-2020-12-24-376.
- [79] S. Designolle et al. “Genuine High-Dimensional Quantum Steering”. In: *Physical Review Letters* 126 (20 2021), p. 200404. DOI: 10.1103/PhysRevLett.126.200404.
- [80] J. Wang et al. “Multidimensional quantum entanglement with large-scale integrated optics”. In: *Science* 360.6386 (2018), pp. 285–291. DOI: 10.1126/science.aar7053.
- [81] U.L. Andersen et al. “Hybrid discrete- and continuous-variable quantum information”. In: *Nature Physics* 11.9 (2015), pp. 713–719. ISSN: 1745-2481. DOI: 10.1038/nphys3410.
- [82] D. Cozzolino et al. “High-Dimensional Quantum Communication: Benefits, Progress, and Future Challenges”. In: *Advanced Quantum Technologies* 2.12 (2019), p. 1900038. DOI: <https://doi.org/10.1002/qute.201900038>.

- [83] F. Flamini, N. Spagnolo, and F. Sciarrino. “Photonic quantum information processing: a review”. In: *Reports on Progress in Physics* 82.1 (2018), p. 016001. DOI: 10.1088/1361-6633/aad5b2.
- [84] A. Forbes and I. Nape. “Quantum mechanics with patterns of light: Progress in high dimensional and multidimensional entanglement with structured light”. In: *AVS Quantum Science* 1.1 (2019), p. 011701. DOI: 10.1116/1.5112027.
- [85] M. Erhard, M. Krenn, and A. Zeilinger. “Advances in high-dimensional quantum entanglement”. In: *Nature Reviews Physics* 2.7 (2020), pp. 365–381. DOI: 10.1038/s42254-020-0193-5.
- [86] A.E. Willner et al. “Orbital angular momentum of light for communications”. In: *Applied Physics Reviews* 8.4 (2021), p. 041312. DOI: 10.1063/5.0054885.
- [87] C. He, Y. Shen, and A. Forbes. “Towards higher-dimensional structured light”. In: *Light: Science & Applications* 11.1 (2022), p. 205. DOI: 10.1038/s41377-022-00897-3.
- [88] M. Piccardo et al. “Roadmap on multimode light shaping”. In: *Journal of Optics* 24.1 (2021), p. 013001. DOI: 10.1088/2040-8986/ac3a9d.
- [89] L.G. Gouy. “Sur la propagation anormale des ondes”. In: *Annales des Chimie et de Physique* 24 (1891), p. 145.
- [90] L.G. Gouy. “Sur une propriété nouvelle des ondes lumineuses”. In: *CR Hebdomadaires Séances Acad. Sci.* 110 (1890), p. 1251.
- [91] B.E.A. Saleh and M.C. Teich. “Fundamentals of Photonics”. In: John Wiley & Sons, Ltd, 1991. ISBN: 9780471213741. DOI: <https://doi.org/10.1002/0471213748>.
- [92] D. Andrews and M. Babiker, eds. *The Angular Momentum of Light*. Cambridge University Press, 2012. DOI: 10.1017/CBO9780511795213.
- [93] C. Gerry and P. Knight. *Introductory Quantum Optics*. Cambridge University Press, 2004. DOI: 10.1017/CBO9780511791239.
- [94] G. Grynberg et al. *Introduction to Quantum Optics: From the Semi-classical Approach to Quantized Light*. Cambridge University Press, 2010. DOI: 10.1017/CBO9780511778261.

- [95] R.W. Boyd. *Nonlinear Optics*. Academic Press, 2013. ISBN: 9780121216801.
- [96] M. Lax, W.H. Louisell, and W.B. McKnight. “From Maxwell to paraxial wave optics”. In: *Physical Review A* 11 (1975), pp. 1365–1370. DOI: 10.1103/PhysRevA.11.1365.
- [97] L.W. Davis. “Theory of electromagnetic beams”. In: *Physical Review A* 19 (1979), pp. 1177–1179. DOI: 10.1103/PhysRevA.19.1177.
- [98] P. Vaveliuk, B. Ruiz, and A. Lencina. “Limits of the paraxial approximation in laser beams”. In: *Optics Letters* 32 (2007), pp. 927–929. DOI: 10.1364/OL.32.000927.
- [99] M.A. Bandres and J.C. Gutiérrez-Vega. “Ince–Gaussian beams”. In: *Optics Letters* 29 (2004), pp. 144–146. DOI: 10.1364/OL.29.000144.
- [100] D. Kawase et al. “Observing Quantum Correlation of Photons in Laguerre–Gauss Modes Using the Gouy Phase”. In: *Physical Review Letters* 101 (2008), p. 050501. DOI: 10.1103/PhysRevLett.101.050501.
- [101] J.P. Torres et al. “Preparation of engineered two-photon entangled states for multidimensional quantum information”. In: *Physical Review A* 67 (5 2003), p. 052313. DOI: 10.1103/PhysRevA.67.052313.
- [102] J.H. Poynting. “The wave motion of a revolving shaft, and a suggestion as to the angular momentum in a beam of circularly polarised light”. In: *Proceedings of the Royal Society of London. Series A* 82 (1909), pp. 560–567. DOI: 10.1098/rspa.1909.0060.
- [103] R.A. Beth. “Mechanical Detection and Measurement of the Angular Momentum of Light”. In: *Physical Review* 50 (1936), pp. 115–125. DOI: 10.1103/PhysRev.50.115.
- [104] J.D. Jackson. *Classical electrodynamics*. Wiley, 1998. ISBN: 9780471309321.
- [105] G.F. Calvo, A. Picón, and E. Bagan. “Quantum field theory of photons with orbital angular momentum”. In: *Physical Review A* 73 (1 2006), p. 013805. DOI: 10.1103/PhysRevA.73.013805.
- [106] E. Leader and C. Lorcé. “The angular momentum controversy: What’s it all about and does it matter?” In: *Physics Reports* 541.3 (2014), pp. 163–248. DOI: 10.1016/j.physrep.2014.02.010.

- [107] H. He, N.R. Heckenberg, and H. Rubinsztein-Dunlop. “Optical Particle Trapping with Higher-order Doughnut Beams Produced Using High Efficiency Computer Generated Holograms”. In: *Journal of Modern Optics* 42.1 (1995), pp. 217–223. DOI: 10.1080/09500349514550171.
- [108] Y. Shen et al. “Optical vortices 30 years on: OAM manipulation from topological charge to multiple singularities”. In: *Light: Science & Applications* 8 (2019), p. 90. DOI: 10.1038/s41377-019-0194-2.
- [109] E. Karimi et al. “Radial quantum number of Laguerre-Gauss modes”. In: *Physical review A* 89 (2014), p. 063813. DOI: 10.1103/PhysRevA.89.063813.
- [110] W.N. Plick et al. “The Forgotten Quantum Number: A short note on the radial modes of Laguerre-Gauss beams”. In: *arXiv preprint* (2013). DOI: 10.48550/arXiv.1306.6517.
- [111] W.N. Plick and M. Krenn. “Physical meaning of the radial index of Laguerre-Gauss beams”. In: *Physical Review A* 92 (2015), p. 063841. DOI: 10.1103/PhysRevA.92.063841.
- [112] J. Audretsch. *Entangled Systems: New Directions in Quantum Physics*. Wiley, 2007. ISBN: 978-3-527-40684-5.
- [113] C. Fabre and N. Treps. “Modes and states in quantum optics”. In: *Reviews of Modern Physics* 92 (3 2020), p. 035005. DOI: 10.1103/RevModPhys.92.035005.
- [114] M. Maggiore. *A Modern introduction to quantum field theory*. Oxford University Press, 2005. ISBN: 978-0-19-852074-0.
- [115] J.J. Sakurai and J. Napolitano. *Modern Quantum Mechanics*. 2nd ed. Cambridge University Press, 2017. DOI: 10.1017/9781108499996.
- [116] Y.B. Band and Y. Avishai. “14 - Many-Body Theory”. In: *Quantum Mechanics with Applications to Nanotechnology and Information Science*. Academic Press, 2013, pp. 825–870. DOI: 10.1016/B978-0-444-53786-7.00014-9.
- [117] A. Beggi et al. “Back and forth from Fock space to Hilbert space: a guide for commuters”. In: *European Journal of Physics* 39.6 (2018), p. 065401. DOI: 10.1088/1361-6404/aad760.

- [118] J.P. Dowling. “Quantum optical metrology – the lowdown on high-N00N states”. In: *Contemporary Physics* 49.2 (2008), pp. 125–143. DOI: 10.1080/00107510802091298.
- [119] A. Wünsche. “Quantization of Gauss–Hermite and Gauss–Laguerre beams in free space”. In: *Journal of Optics B: Quantum and Semiclassical Optics* 6.3 (2004), S47. DOI: 10.1088/1464-4266/6/3/009.
- [120] R.J. Glauber. “The Quantum Theory of Optical Coherence”. In: *Physical Review* 130 (6 1963), pp. 2529–2539. DOI: 10.1103/PhysRev.130.2529.
- [121] T. Durt et al. “On mutually unbiased bases”. In: *International Journal of Quantum Information* 08.04 (2010), pp. 535–640. DOI: 10.1142/S0219749910006502.
- [122] S. Pirandola et al. “Advances in quantum cryptography”. In: *Advances in Optics and Photonics* 12.4 (2020), pp. 1012–1236. DOI: 10.1364/AOP.361502.
- [123] C.H. Bennett and G. Brassard. “Quantum cryptography: Public key distribution and coin tossing”. In: *Proceedings of International Conference on Computers, Systems and Signal Processing* 1 (1984), pp. 175–179. DOI: 10.48550/arXiv.2003.06557.
- [124] J.C. Garcia-Escartin, V. Gimeno, and J.J. Moyano-Fernández. “Optimal approximation to unitary quantum operators with linear optics”. In: *Quantum Information Processing* 20.9 (2021), p. 314. DOI: 10.1007/s11128-021-03254-2.
- [125] J.-F. Morizur et al. “Programmable unitary spatial mode manipulation”. In: *Journal of the Optical Society of America A* 27.11 (2010), pp. 2524–2531. DOI: 10.1364/JOSAA.27.002524.
- [126] S.L. Braunstein and P. van Loock. “Quantum information with continuous variables”. In: *Reviews of Modern Physics* 77 (2 2005), pp. 513–577. DOI: 10.1103/RevModPhys.77.513.
- [127] V. Giovannetti, S. Lloyd, and L. Maccone. “Advances in quantum metrology”. In: *Nature Photonics* 5.4 (2011), pp. 222–229. DOI: 10.1038/nphoton.2011.35.

- [128] E. Polino et al. “Photonic quantum metrology”. In: *AVS Quantum Science* 2.2 (2020), p. 024703. DOI: 10.1116/5.0007577.
- [129] M. Barbieri. “Optical Quantum Metrology”. In: *PRX Quantum* 3 (1 2022), p. 010202. DOI: 10.1103/PRXQuantum.3.010202.
- [130] Z.Y. Ou, L.J. Wang, and L. Mandel. “Vacuum effects on interference in two-photon down conversion”. In: *Physical Review A* 40 (3 1989), pp. 1428–1435. DOI: 10.1103/PhysRevA.40.1428.
- [131] V. Srivastav et al. “Characterizing and Tailoring Spatial Correlations in Multimode Parametric Down-Conversion”. In: *Physical Review Applied* 18 (5 2022), p. 054006. DOI: 10.1103/PhysRevApplied.18.054006.
- [132] T.E. Keller and M.H. Rubin. “Theory of two-photon entanglement for spontaneous parametric down-conversion driven by a narrow pump pulse”. In: *Physical Review A* 56 (2 1997), pp. 1534–1541. DOI: 10.1103/PhysRevA.56.1534.
- [133] Y. Shih. “Entangled biphoton source - property and preparation”. In: *Reports on Progress in Physics* 66.6 (2003), p. 1009. DOI: 10.1088/0034-4885/66/6/203.
- [134] D. Ljunggren and M. Tengner. “Optimal focusing for maximal collection of entangled narrow-band photon pairs into single-mode fibers”. In: *Physical Review A* 72 (6 2005), p. 062301. DOI: 10.1103/PhysRevA.72.062301.
- [135] M. Fiorentino et al. “Spontaneous parametric down-conversion in periodically poled KTP waveguides and bulk crystals”. In: *Optics Express* 15.12 (2007), pp. 7479–7488. DOI: 10.1364/OE.15.007479.
- [136] A. Christ et al. “Theory of quantum frequency conversion and type-II parametric down-conversion in the high-gain regime”. In: *New Journal of Physics* 15.5 (2013), p. 053038. DOI: 10.1088/1367-2630/15/5/053038.
- [137] S. Lerch et al. “Tuning curve of type-0 spontaneous parametric down-conversion”. In: *Journal of the Optical Society of America B* 30.4 (2013), pp. 953–958. DOI: 10.1364/JOSAB.30.000953.
- [138] N. Tischler et al. “Measurement and Shaping of Biphoton Spectral Wave Functions”. In: *Physical Review Letters* 115 (19 2015), p. 193602. DOI: 10.1103/PhysRevLett.115.193602.

- [139] K. Zielnicki et al. “Joint spectral characterization of photon-pair sources”. In: *Journal of Modern Optics* 65.10 (2018), pp. 1141–1160. DOI: 10.1080/09500340.2018.1437228.
- [140] C. Couteau. “Spontaneous parametric down-conversion”. In: *Contemporary Physics* 59.3 (2018), pp. 291–304. DOI: 10.1080/00107514.2018.1488463.
- [141] M.M. Fejer et al. “Quasi-phase-matched second harmonic generation: tuning and tolerances”. In: *IEEE Journal of Quantum Electronics* 28.11 (1992), pp. 2631–2654. DOI: 10.1109/3.161322.
- [142] C.K. Hong and L. Mandel. “Experimental realization of a localized one-photon state”. In: *Physical Review Letters* 56 (1 1986), pp. 58–60. DOI: 10.1103/PhysRevLett.56.58.
- [143] See Supplemental Material **publication III**. URL: <https://doi.org/10.1038/s41566-022-01077-w>.
- [144] C.M. Natarajan, M.G. Tanner, and R.H. Hadfield. “Superconducting nanowire single-photon detectors: physics and applications”. In: *Superconductor Science and Technology* 25.6 (2012), p. 063001. DOI: 10.1088/0953-2048/25/6/063001.
- [145] R. Fickler et al. “Real-time imaging of quantum entanglement”. In: *Scientific reports* 3.1 (2013), pp. 1–5. DOI: 10.1038/srep01914.
- [146] X.Y. Zou, L.J. Wang, and L. Mandel. “Violation of classical probability in parametric down-conversion”. In: *Optics Communications* 84.5 (1991), pp. 351–354. DOI: 10.1016/0030-4018(91)90101-I.
- [147] R. Fickler. “Quantum entanglement of complex structures of photons”. PhD thesis. 2015. DOI: 10.1007/978-3-319-22231-8.
- [148] S.G. Lukishova. “Fifteen years of quantum optics, quantum information, and nano-optics educational facility at the Institute of Optics, University of Rochester”. In: *Optical Engineering* 61.8 (2022), p. 081811. DOI: 10.1117/1.OE.61.8.081811.

- [149] M.M. Hayat, S.N. Torres, and L.M. Pedrotti. “Theory of photon coincidence statistics in photon-correlated beams”. In: *Optics Communications* 169.1 (1999), pp. 275–287. ISSN: 0030-4018. DOI: 10.1016/S0030-4018(99)00384-3.
- [150] Laser Components. *Single Photon Counting Module COUNT[®] T-Series: datasheet*. Accessed: 22/02/2023. URL: www.lasercomponents.com/fileadmin/user_upload/home/Datasheets/lc-photon-counter/count-t.pdf.
- [151] K. Schätzel et al. “Correction of detection-system dead-time effects on photon-correlation functions”. In: *Journal of the Optical Society of America B* 6.5 (1989), pp. 937–947. DOI: 10.1364/JOSAB.6.000937.
- [152] V. Tiwari and N.S. Bisht. “Spatial Light Modulators and Their Applications in Polarization Holography”. In: *Holography*. Ed. by J. Rosen. IntechOpen, 2022. Chap. 1. DOI: 10.5772/intechopen.107110.
- [153] A. Jesacher. “Applications of Spatial Light Modulators for Optical Trapping and Image Processing”. PhD thesis. 2007.
- [154] *Application Note: HOLOEYE Spatial Light Modulators*. Accessed: 23/02/2023. URL: holoeye.com/wp-content/uploads/Application_Note_SLM-V.59.pdf.
- [155] M. Takeda, H. Ina, and S. Kobayashi. “Fourier-transform method of fringe-pattern analysis for computer-based topography and interferometry”. In: *Journal of the Optical Society of America* 72.1 (1982), pp. 156–160. DOI: 10.1364/JOSA.72.000156.
- [156] N. Verrier and M. Atlan. “Off-axis digital hologram reconstruction: some practical considerations”. In: *Applied Optics* 50.34 (2011), H136–H146. DOI: 10.1364/AO.50.00H136.
- [157] J. Carpenter. *digHolo : High-speed library for off-axis digital holography and Hermite-Gaussian decomposition*. 2022. DOI: 10.48550/ARXIV.2204.02348.
- [158] A. Jesacher et al. “Wavefront correction of spatial light modulators using an optical vortex image”. In: *Optics Express* 15.9 (2007), pp. 5801–5808. DOI: 10.1364/OE.15.005801.

- [159] X. Xun and R.W. Cohn. “Phase calibration of spatially nonuniform spatial light modulators”. In: *Applied Optics* 43.35 (2004), pp. 6400–6406. DOI: 10.1364/AO.43.006400.
- [160] R.W. Gerchberg and Saxton W.O. “A Practical Algorithm for the Determination of Phase from Image and Diffraction Plane Pictures”. In: *Optik* 35.2 (1972), pp. 237–246. URL: www.u.arizona.edu/~ppoon/GerchbergandSaxton1972.pdf.
- [161] N.R. Heckenberg et al. “Laser beams with phase singularities”. In: *Optical and Quantum Electronics* 24.9 (1992), S951–S962. DOI: 10.1007/BF01588597.
- [162] N.R. Heckenberg et al. “Generation of optical phase singularities by computer-generated holograms”. In: *Optics Letters* 17.3 (1992), pp. 221–223. DOI: 10.1364/OL.17.000221.
- [163] J. Arlt et al. “The production of multiringed Laguerre–Gaussian modes by computer-generated holograms”. In: *Journal of Modern Optics* 45.6 (1998), pp. 1231–1237. DOI: 10.1080/09500349808230913.
- [164] J. Arlt et al. “Parametric down-conversion for light beams possessing orbital angular momentum”. In: *Physical Review A* 59 (5 1999), pp. 3950–3952. DOI: 10.1103/PhysRevA.59.3950.
- [165] A. Mair et al. “Entanglement of the orbital angular momentum states of photons”. In: *Nature* 412.6844 (2001), pp. 313–316. DOI: 10.1038/35085529.
- [166] J.A. Davis et al. “Encoding amplitude information onto phase-only filters”. In: *Applied Optics* 38.23 (1999), pp. 5004–5013. DOI: 10.1364/AO.38.005004.
- [167] J. Leach et al. “Vortex knots in light”. In: *New Journal of Physics* 7.1 (2005), p. 55. DOI: 10.1088/1367-2630/7/1/055.
- [168] V. Arrizón et al. “Pixelated phase computer holograms for the accurate encoding of scalar complex fields”. In: *Journal of the Optical Society of America A* 24.11 (2007), pp. 3500–3507. DOI: 10.1364/JOSAA.24.003500.

- [169] E. Bolduc et al. “Exact solution to simultaneous intensity and phase encryption with a single phase-only hologram”. In: *Optics Letters* 38.18 (2013), pp. 3546–3549. DOI: 10.1364/OL.38.003546.
- [170] M. Plöschner et al. “Spatial tomography of light resolved in time, spectrum, and polarisation”. In: *Nature Communications* 13.1 (2022). Supplementary information, p. 4294. DOI: 10.1038/s41467-022-31814-2.
- [171] J. Carpenter. *Gerchberg-Saxton algorithm (Tutorial)*. Youtube. 2021. URL: <https://youtu.be/momXpSbOqMQ>.
- [172] S.Z.D. Plachta et al. “Quantum advantage using high-dimensional twisted photons as quantum finite automata”. In: *Quantum* 6 (2022), p. 752. DOI: 10.22331/q-2022-06-30-752.
- [173] J. Leach et al. “Measuring the Orbital Angular Momentum of a Single Photon”. In: *Physical Review Letters* 88 (25 2002), p. 257901. DOI: 10.1103/PhysRevLett.88.257901.
- [174] N.K. Fontaine et al. “Laguerre-Gaussian mode sorter”. In: *Nature Communications* 10.1 (2019), p. 1865. DOI: 10.1038/s41467-019-09840-4.
- [175] H. Defienne and D. Faccio. “Arbitrary spatial mode sorting in a multi-mode fiber”. In: *Physical Review A* 101 (6 2020), p. 063830. DOI: 10.1103/PhysRevA.101.063830.
- [176] J. Leach et al. “Interferometric Methods to Measure Orbital and Spin, or the Total Angular Momentum of a Single Photon”. In: *Physical Review Letters* 92 (1 2004), p. 013601. DOI: 10.1103/PhysRevLett.92.013601.
- [177] G.C.G. Berkhout et al. “Efficient Sorting of Orbital Angular Momentum States of Light”. In: *Physical Review Letters* 105 (15 2010), p. 153601. DOI: 10.1103/PhysRevLett.105.153601.
- [178] A. Dudley et al. “Efficient sorting of Bessel beams”. In: *Optics Express* 21.1 (2013), pp. 165–171. DOI: 10.1364/OE.21.000165.
- [179] M. Mirhosseini et al. “Efficient separation of the orbital angular momentum eigenstates of light”. In: *Nature Communications* 4.1 (2013), p. 2781. DOI: 10.1038/ncomms3781.

- [180] Y. Zhou et al. “Sorting Photons by Radial Quantum Number”. In: *Physical Review Letters* 119 (26 2017), p. 263602. DOI: 10.1103/PhysRevLett.119.263602.
- [181] R. Saad et al. “Highly Selective 7 Orbital Angular Momentum Mode Multiplexer Based on Multi-Plane Light Conversion”. In: *2017 European Conference on Optical Communication (ECOC)*. 2017, pp. 1–3. DOI: 10.1109/ECOC.2017.8345890.
- [182] G.F. Walsh et al. “Parallel sorting of orbital and spin angular momenta of light in a record large number of channels”. In: *Optics Letters* 43.10 (2018), pp. 2256–2259. DOI: 10.1364/OL.43.002256.
- [183] X. Gu et al. “Gouy Phase Radial Mode Sorter for Light: Concepts and Experiments”. In: *Physical Review Letters* 120 (10 2018), p. 103601. DOI: 10.1103/PhysRevLett.120.103601.
- [184] G. Gibson et al. “Free-space information transfer using light beams carrying orbital angular momentum”. In: *Optics Express* 12.22 (2004), pp. 5448–5456. DOI: 10.1364/OPEX.12.005448.
- [185] A. Trichili et al. “Encoding information using Laguerre Gaussian modes over free space turbulence media”. In: *Optics Letters* 41.13 (2016), pp. 3086–3089. DOI: 10.1364/OL.41.003086.
- [186] F. Bouchard et al. “Measuring azimuthal and radial modes of photons”. In: *Optics Express* 26.24 (2018), pp. 31925–31941. DOI: 10.1364/OE.26.031925.
- [187] G. Labroille et al. “Efficient and mode selective spatial mode multiplexer based on multi-plane light conversion”. In: *Optics Express* 22.13 (2014), pp. 15599–15607. DOI: 10.1364/OE.22.015599.
- [188] M. Hiekkamäki, S. Prabhakar, and R. Fickler. “Near-perfect measuring of full-field transverse-spatial modes of light”. In: *Optics Express* 27.22 (2019), pp. 31456–31464. DOI: 10.1364/OE.27.031456.
- [189] G. Labroille et al. *Mode selective 10-mode multiplexer based on multi-plane light conversion*. 2016. DOI: 10.1364/OFC.2016.Th3E.5.

- [190] N.K. Fontaine et al. “Design of High Order Mode-Multiplexers using Multiplane Light Conversion”. In: *2017 European Conference on Optical Communication (ECOC)*. 2017, pp. 1–3. DOI: 10.1109/ECOC.2017.8346129.
- [191] N.K. Fontaine et al. “Hermite-Gaussian mode multiplexer supporting 1035 modes”. In: *Optical Fiber Communication Conference (OFC) 2021*. 2021, p. M3D.4. DOI: 10.1364/OFC.2021.M3D.4.
- [192] H. Kupianskyi, S.A.R. Horsley, and D.B. Phillips. “High-dimensional spatial mode sorting and optical circuit design using multi-plane light conversion”. In: *APL Photonics* 8.2 (2023). DOI: 10.1063/5.0128431.
- [193] N. Barré and A. Jesacher. “Inverse design of gradient-index volume multimode converters”. In: *Optics Express* 30.7 (2022), pp. 10573–10587. DOI: 10.1364/OE.450196.
- [194] Y. Sakamaki et al. “New Optical Waveguide Design Based on Wavefront Matching Method”. In: *Journal of Lightwave Technology* 25.11 (2007), pp. 3511–3518. DOI: 10.1109/JLT.2007.906798.
- [195] M. Hiekkamäki, S. Prabhakar, and R. Fickler. *Wavefront Matching Code for Transverse Spatial Mode Conversion*. Dec. 2019. DOI: 10.5281/zenodo.3570622.
- [196] A.M. Brańczyk. *Hong-Ou-Mandel Interference*. 2017. DOI: 10.48550/ARXIV.1711.00080.
- [197] R. Kaltenbaek et al. “Experimental Interference of Independent Photons”. In: *Physical Review Letters* 96 (24 2006), p. 240502. DOI: 10.1103/PhysRevLett.96.240502.
- [198] See Supplemental Material **publication I**. URL: <http://link.aps.org/supplemental/10.1103/PhysRevLett.126.123601>.
- [199] S. Prabhakar et al. “Turbulence and the Hong-Ou-Mandel effect”. In: *Physical Review A* 97 (1 2018), p. 013835. DOI: 10.1103/PhysRevA.97.013835.
- [200] J.G. Rarity, P.R. Tapster, and R. Loudon. “Non-classical interference between independent sources”. In: *Journal of Optics B: Quantum and Semiclassical Optics* 7.7 (2005), S171. DOI: 10.1088/1464-4266/7/7/007.

- [201] Y.-S. Kim et al. “Conditions for two-photon interference with coherent pulses”. In: *Physical Review A* 87 (6 2013), p. 063843. DOI: 10.1103/PhysRevA.87.063843.
- [202] S. Sadana et al. “Near-100% two-photon-like coincidence-visibility dip with classical light and the role of complementarity”. In: *Physical Review A* 100 (1 2019), p. 013839. DOI: 10.1103/PhysRevA.100.013839.
- [203] A.J. Hayter. *Probability and statistics for engineers and scientists*. Cengage Learning, 2012.
- [204] J. Schneeloch et al. “Introduction to the absolute brightness and number statistics in spontaneous parametric down-conversion”. In: *Journal of Optics* 21.4 (2019), p. 043501. DOI: 10.1088/2040-8986/ab05a8.
- [205] S. Slussarenko et al. “Unconditional violation of the shot-noise limit in photonic quantum metrology”. In: *Nature Photonics* 11.11 (2017), pp. 700–703. ISSN: 1749-4893. DOI: 10.1038/s41566-017-0011-5.
- [206] Supplemental Material of **publication II**. URL: <http://link.aps.org/supplemental/10.1103/PhysRevLett.127.263601>.
- [207] R. Demkowicz-Dobrzański, M. Jarzyna, and J. Kołodyński. “Chapter Four - Quantum Limits in Optical Interferometry”. In: ed. by E. Wolf. Vol. 60. *Progress in Optics*. Elsevier, 2015, pp. 345–435. DOI: <https://doi.org/10.1016/bs.po.2015.02.003>.
- [208] S.L. Braunstein and C.M. Caves. “Statistical distance and the geometry of quantum states”. In: *Physical Review Letters* 72 (22 1994), pp. 3439–3443. DOI: 10.1103/PhysRevLett.72.3439.
- [209] P. Woźniak et al. “Tighter spots of light with superposed orbital-angular-momentum beams”. In: *Physical Review A* 94 (2 2016), p. 021803. DOI: 10.1103/PhysRevA.94.021803.
- [210] M. Krenn, N. Tischler, and A. Zeilinger. “On small beams with large topological charge”. In: *New Journal of Physics* 18.3 (2016), p. 033012. DOI: 10.1088/1367-2630/18/3/033012.
- [211] S. Prabhakar et al. “High-accuracy longitudinal position measurement using self-accelerating light”. In: *Applied Optics* 60.11 (2021), pp. 3203–3210. DOI: 10.1364/AO.420590.

- [212] F.C.V. de Brito et al. “Gouy phase of type-I SPDC-generated biphotons”. In: *Physics Letters A* 386 (2021), p. 126989. ISSN: 0375-9601. DOI: <https://doi.org/10.1016/j.physleta.2020.126989>.
- [213] O. Baladron-Zorita et al. “Isolating the Gouy phase shift in a full physical-optics solution to the propagation problem”. In: *Journal of the Optical Society of America A* 36.9 (2019), pp. 1551–1558. DOI: 10.1364/JOSAA.36.001551.
- [214] R.W. Boyd. “Intuitive explanation of the phase anomaly of focused light beams”. In: *Journal of the Optical Society of America* 70.7 (1980), pp. 877–880. DOI: 10.1364/JOSA.70.000877.
- [215] S. Feng and H.G. Winful. “Physical origin of the Gouy phase shift”. In: *Optics Letters* 26.8 (2001), pp. 485–487. DOI: 10.1364/OL.26.000485.
- [216] P. Hariharan and P.A. Robinson. “The gouy phase shift as a geometrical quantum effect”. In: *Journal of Modern Optics* 43.2 (1996), pp. 219–221. DOI: 10.1080/09500349608232735.
- [217] T.D. Visser and E. Wolf. “The origin of the Gouy phase anomaly and its generalization to astigmatic wavefields”. In: *Optics Communications* 283.18 (2010), pp. 3371–3375. DOI: 10.1016/j.optcom.2010.04.099.
- [218] R. Simon and N. Mukunda. “Bargmann invariant and the geometry of the G uyoy effect”. In: *Physical Review Letters* 70 (7 1993), pp. 880–883. DOI: 10.1103/PhysRevLett.70.880.
- [219] D. Subbarao. “Topological phase in Gaussian beam optics”. In: *Optics Letters* 20.21 (1995), pp. 2162–2164. DOI: 10.1364/OL.20.002162.
- [220] J. Yang and H.G. Winful. “Generalized eikonal treatment of the Gouy phase shift”. In: *Optics Letters* 31.1 (2006), pp. 104–106. DOI: 10.1364/OL.31.000104.
- [221] T. Lee et al. “Origin of Gouy Phase Shift Identified by Laser-Generated Focused Ultrasound”. In: *ACS Photonics* 7.11 (2020), pp. 3236–3245. DOI: 10.1021/acsp Photonics.0c01313.
- [222] J. Jacobson et al. “Photonic de Broglie Waves”. In: *Physical Review Letters* 74 (24 1995), pp. 4835–4838. DOI: 10.1103/PhysRevLett.74.4835.

- [223] K. Edamatsu, R. Shimizu, and T. Itoh. “Measurement of the Photonic de Broglie Wavelength of Entangled Photon Pairs Generated by Spontaneous Parametric Down-Conversion”. In: *Physical Review Letters* 89 (21 2002), p. 213601. DOI: 10.1103/PhysRevLett.89.213601.
- [224] P. Walther et al. “De Broglie wavelength of a non-local four-photon state”. In: *Nature* 429 (2004), pp. 158–161. DOI: 10.1038/nature02552.
- [225] X. Gu and M. Krenn. “Phase anomaly brings quantum implications”. In: *Nature Photonics* 16 (2022), pp. 815–817. DOI: 10.1038/s41566-022-01118-4.
- [226] A. Datta et al. “Quantum metrology with imperfect states and detectors”. In: 83 (6 2011), p. 063836. DOI: 10.1103/PhysRevA.83.063836.
- [227] M. Mounaix et al. “Time reversed optical waves by arbitrary vector spatiotemporal field generation”. In: *Nature communications* 11 (2020), p. 5813. DOI: 10.1038/s41467-020-19601-3.
- [228] M. Eriksson et al. *Sensing rotations with multiplane light conversion*. 2023. arXiv: 2301.10265 [quant-ph].

PUBLICATIONS

PUBLICATION

I

High-Dimensional Two-Photon Interference Effects in Spatial Modes

Markus Hiekkamäki and Robert Fickler

Physical Review Letters 126 (2021), p. 123601

Publication reprinted with the permission of the copyright holders.

High-Dimensional Two-Photon Interference Effects in Spatial ModesMarkus Hiekkamäki^{✉*} and Robert Fickler^{✉*}*Tampere University, Photonics Laboratory, Physics Unit, Tampere FI-33720, Finland* (Received 7 November 2020; accepted 18 February 2021; published 22 March 2021; corrected 9 June 2022)

Two-photon interference is a fundamental quantum optics effect with numerous applications in quantum information science. Here, we study two-photon interference in multiple transverse-spatial modes along a single beam-path. Besides implementing the analog of the Hong-Ou-Mandel interference using a two-dimensional spatial-mode splitter, we extend the scheme to observe coalescence and anticorrelation in different three- and four-dimensional spatial-mode multiports. The operation within spatial modes, along a single beam path, lifts the requirement for interferometric stability and opens up new pathways of implementing linear optical networks for complex quantum information tasks.

DOI: [10.1103/PhysRevLett.126.123601](https://doi.org/10.1103/PhysRevLett.126.123601)

Two-photon interference at a beam splitter, i.e., Hong-Ou-Mandel (HOM) interference [1], is one of the most important effects in photonic quantum information science [2]. Its applications range from quantum computing [3], to cryptography [4] and from repeaters [5] to sensing [6], as well as quantum foundations [7]. Because of its importance, it has been studied with photons from different sources [8,9] and in different degrees of freedom (DOF) [10–12]. Domains that can encode high-dimensional quantum states, such as spatial, spectral, and temporal DOF, have attracted a lot of attention as they can be used to implement schemes with multiple input and output ports, i.e., multiports. Such linear optical networks are of importance for performing increasingly complex tasks in photonic quantum computing that require multiphoton interference [13–17].

Transverse-spatial modes, i.e., propagation invariant photonic structures that discretize the transverse-spatial domain, comprise a popular Hilbert space for encoding high-dimensional quantum states [18]. One prominent family of spatial modes is the Laguerre-Gaussian (LG) family that is defined by two quantum numbers, ℓ and p , describing the photons' azimuthal and radial structures, respectively. The azimuthal DOF has gained significant popularity as it is connected to the orbital angular momentum (OAM) of photons [19]. Benefits of encoding quantum states in photonic spatial structures include mature technologies for generating and detecting high-dimensional states, as well as intrinsic phase stability of complex superposition states, ensured by single beam-path operation.

In this Letter, we demonstrate two-photon interferences in multiple transverse-spatial modes. We use the technique of multiplane light conversion (MPLC) [20] to implement various spatial-mode unitaries, leading to different interference effects between two structured photons. We first observe bunching of photon pairs into the same spatial mode by implementing the direct spatial-mode analog of

HOM interference using a two-dimensional “mode splitter.” Utilizing the same setup and benefiting from the advantages spatial modes offer, we study various two-photon interferences in high-dimensional state spaces along with complex superposition states. The flexibility of our high-dimensional spatial-mode multiport further allows observing both coalescence and anticorrelation of photon pairs with three and four input and output modes. Our demonstration opens up paths to realize novel implementations and complement existing high-dimensional linear optical networks for quantum information science.

In the conventional HOM interference, photon bunching is obtained when two photons that are indistinguishable, i.e., perfectly overlapping in polarization, spatial structure, and time, are sent into a balanced beam splitter from separate inputs. While classically four different output situations are possible, only the two possibilities in which both photons exit through the same output port will remain after the interference [see Fig. 1(a)], which can be attributed to the bosonic nature of photons. A common way of assessing the quality of the interference is evaluating the change in coincident detections of the two exiting photons while scanning the temporal delay between them. This quality can be quantified with a visibility $V = |R_{cl} - R_{qu}|/R_{cl} \in [0, 1]$ [21] between the classically expected rate R_{cl} and the rate R_{qu} observed due to quantum interference.

In our experiment, we replace the beam splitter acting on the paths with a mode splitter acting on the transverse-spatial modes of the photons. Hence, the photons bunch into the transverse-spatial modes, which is in contrast to previous quantum interference measurements, where spatial-mode overlap served as a *condition* for observing two-photon bunching into paths [26–30]. We note that in one recent experiment single-path two-photon interference between two spatially structured photons was observed, however, using polarization structures which limit the dimensionality to two [31].

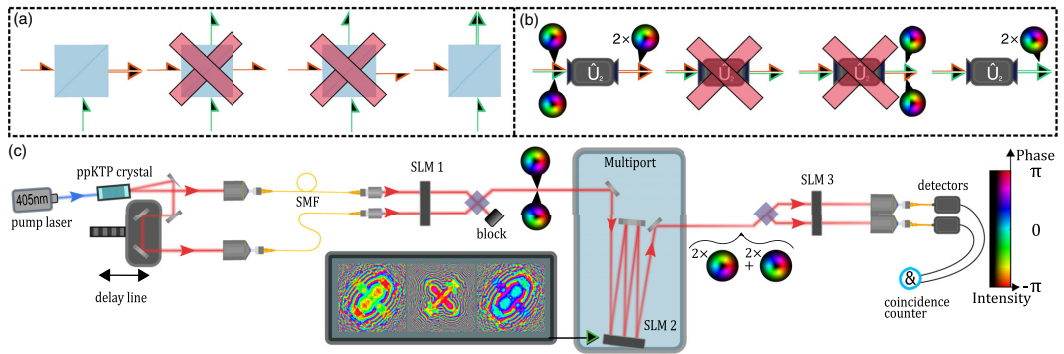


FIG. 1. Conceptual sketch of two-photon interference and the experimental setup. (a) Conventional HOM interference in a regular beam splitter between two paths. (b) Its spatial mode analog implemented with a mode splitter. (c) The setup used to demonstrate two-photon interferences in different mode splitters. Photon pairs are produced in a periodically poled potassium titanyl phosphate (ppKTP) crystal, adjusted in their temporal overlap using a delay line, and coupled into single mode fibers. Three spatial light modulators are used for spatial mode generation [22] (SLM1), unitary transformation [14] (SLM2), and measurement [23,24] (SLM3). Single photon detectors and a coincidence counter are used to detect the photon pairs. For more details, see the main text and Supplemental Material [25]. The two-dimensional color map shown in (c) is used in all of the figures.

To study HOM interference between two spatial modes, we prepare the photons in orthogonal OAM modes, i.e., one photon with $\ell = +1$ and the second having $\ell = -1$. Note that although our scheme would be able to transform any combination of spatial modes [14], we are only involving the OAM degree of freedom. Using the Fock-state notation $|n\rangle_\ell$, where n is the photon number and the subscript labels the OAM value, we can write the input state as $|1\rangle_{-1}|1\rangle_{+1} = |1, 1\rangle$. Analogous to the classic HOM interference, a balanced mode splitter unitary \hat{U}_2 transforms the two input modes into two equally weighted superpositions which leads, via interference, to the state

$$|\Psi_{2D}\rangle = \frac{1}{\sqrt{2}}(|0, 2\rangle - |2, 0\rangle), \quad (1)$$

if the two photons are perfectly indistinguishable in polarization, time, spectrum, as well as path [see Fig. 1(b) and the Supplemental Material [25] for more details]. This state is distinct from earlier spatial-mode interference experiments [26–30], as it is a so-called NOON state in a single optical path, which is a desirable state for quantum metrology tasks due to its increased phase sensitivity [32]. The single beam-path operation is similar to quantum interference with polarization [10,33], however, with the much larger state space that spatial modes offer. Thus, enabling more complex unitary transformations and a pathway to building single-path linear optical networks.

In the experiment [see sketch of the setup in Fig. 1(c) and Supplemental Material [25]], we generate photon pairs using spontaneous parametric down-conversion, ensure their temporal overlap through a delay line in the path of one photon, and couple both photons into single mode

fibers (SMF), thereby spatially filtering them to a Gaussian mode. Using a fiber beam splitter, we obtain an initial HOM visibility of $97.7\% \pm 0.2\%$ (see the Supplemental Material [25]). Note that for all visibility values given throughout the Letter, the errors denote a standard error calculated from a fit to the data. For more information on the specific function we fit to the data, see the Supplemental Material [25], which is partially based on the derivation in Ref. [34]. A few examples of these fits are shown in Fig. 2. We then imprint the desired spatial modes onto the photons using a spatial light modulator (SLM) and an amplitude and phase modulation technique to guarantee the best mode quality at the cost of loss (around 94%–99% loss per photon) [22]. Lossless schemes exist [35] but we abstain from using them due to their complexity. After imprinting the modes, the two photons are overlapped probabilistically with a balanced beam splitter. The input spatial modes are chosen to be orthogonal to avoid any interference in the combining beam splitter.

The photons are then input into the spatial-mode multiport, i.e., an MPLC setup, that we use to implement any unitary operation on the biphoton state. The three phase modulations in our MPLC setup, that define each unitary, are generated using free-space wavefront matching (WFM), which is described in more detail in the Supplemental Material [25], and an example code can be found in Ref. [36], and earlier works [14,37]. When generating these transformations, the pixelization and limited number of phase values (8 bit) of our SLMs are taken into account. Our 2D mode splitter achieved a simulated efficiency above 99% for a bandwidth of roughly 5 nm around the target wavelength. Importantly, out of the 1% loss, only a small fraction (1%) remains in our operating state space, i.e.,

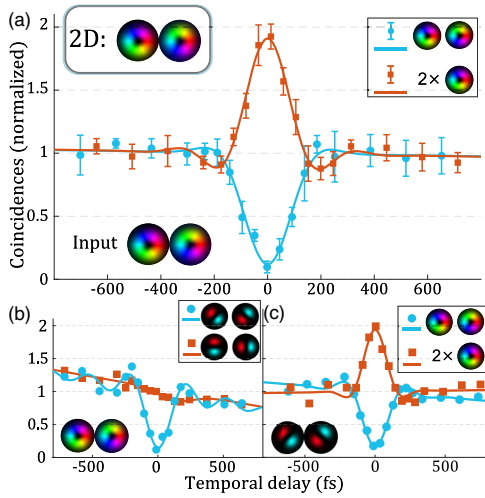


FIG. 2. Measurement of two-photon bunching in a two-dimensional mode splitter. (a) HOM-like interference visualized in Fig. 1(b). Insets show the input modes of both photons (lower left) and legends depict the mode pair they were projected onto (upper right). (b) Interference data with the same input two-photon state projected onto two different MUBs. (c) Flipped scenario of (b), i.e., the input states are in a different MUB and projected onto the OAM basis. The mode splitter unitary \hat{U}_2 was the same in all three scenarios. The error bars are standard deviations calculated from multiple consecutive measurements and the curves are fits. In (b) and (c) the error bars were omitted for clarity and can be found in the Supplemental Material [25]. The change in the overall coincidence rates, especially visible in (b), is a result of decoupling over time.

contributes to errors. Note that this particular transformation for OAM modes $\ell = \pm 1$ resembles two rotated cylindrical lenses [38]. The simulated evolution of the photon's structure in the 2D transformation, with all the other utilized phase modulations, are displayed in the Supplemental Material [25].

After the two-photon state has been transformed through the mode splitter, the photons are probabilistically split into separate paths using another beam splitter. Their individual spatial modes are then measured using another phase modulation and SMF coupling followed by detection [23,24]. The signals of the detectors are fed into a time tagging unit, which registers coincident detections through temporal correlations. If the two-photon interference in spatial modes was successful, no coincidence counts will be detected when the photons are projected on orthogonal modes, i.e., using the projection operator $\hat{P}_{+1-1} = |1\rangle_{-1}|1\rangle_{+1}\langle 1|_{-1}\langle 1|_{+1} = |1,1\rangle\langle 1,1|$. Simultaneously scanning the temporal delay between the photons results in a dip in coincidence detections, identical to a classic HOM dip.

For the 2D mode splitter, we obtain a HOM-interference dip with a visibility $88.0\% \pm 3.8\%$, that is well above the classical limit of 50% [39]. When the two photons are projected onto the same state, i.e., $\hat{P}_{+1+1} = |0,2\rangle\langle 0,2|$, we observe an increase in coincidences due to bunching, i.e., a HOM bump, with a visibility $90.9\% \pm 4.5\%$. This change in the projection only requires changing one hologram on SLM3. Both results are shown in Fig. 2(a).

We then take advantage of a particular benefit of spatial modes and study the interference when generating and detecting superposition states, a task that is usually difficult to implement in other degrees of freedom. At first, we keep the photons in the same input state, but project them onto orthogonal states of the two other mutually unbiased bases (MUB), which we define as $|\Psi_{D/A}\rangle = 1/\sqrt{2}(|1,0\rangle \pm i|0,1\rangle)$ and $|\Psi_{H/V}\rangle = 1/\sqrt{2}(|1,0\rangle \pm |0,1\rangle)$. When projecting the photons onto the orthogonal states of the (D/A)-MUB, we again find an interference dip with a visibility of $85.6\% \pm 6.2\%$. However, when projecting both photons onto the (H/V)-MUB, no bunching is observed as both photons are transformed through the mode splitter into the eigenstates of this basis [see Fig. 2(b)].

To show that it is irrelevant whether we prepare or project onto superpositions, we then generate photons in the superposition states $|\Psi_A\rangle$ and $|\Psi_D\rangle$ but perform the projection measurements \hat{P}_{+1-1} and \hat{P}_{+1+1} . The results are similar to the ones using no superposition states, with visibilities $84.0\% \pm 4.1\%$ and $93.8\% \pm 9.5\%$, for the dip and the bump, respectively [see Fig. 2(c)]. Note that, although the interference remains the same, the relative phase changes in the output state, allowing tuning of the obtained state.

To verify generation of the entangled state described in Eq. (1), we perform an entanglement witness test on the two postselected photons, which verifies nonseparability if the sum of the visibilities measured in at least two MUBs is larger than 1 [40–42]. From our measurements in all three MUBs, we obtain a witness value of $w = 2.2 \pm 0.1$, which is more than 11 standard deviations above the classical limit (see Supplemental Material [25] for details).

We then scale our state space to larger dimensions, i.e., study two-photon interferences in high-dimensional mode splitters. At first, we choose a balanced three-dimensional mode splitter \hat{U}_3 operating on the state space spanned by LG modes with $\ell = -1, 0, +1$. With this unitary, that splits the photons into an even superposition of all three spatial modes, different interference effects can be observed. For example, if we again send in the same input state, now written as $|\Psi\rangle = |1\rangle_{-1}|0\rangle_0|1\rangle_{+1} = |1,0,1\rangle$, we will not observe a perfect bunching. By measuring correlations using any of the projectors \hat{P}_{+1-1} , \hat{P}_{+10} , or \hat{P}_{0-1} , a HOM dip with a maximum visibility of 0.5 can be observed (see Supplemental Material [25]). Experimentally we measure visibilities of $39.7\% \pm 2.9\%$, $49.3\% \pm 3.1\%$,

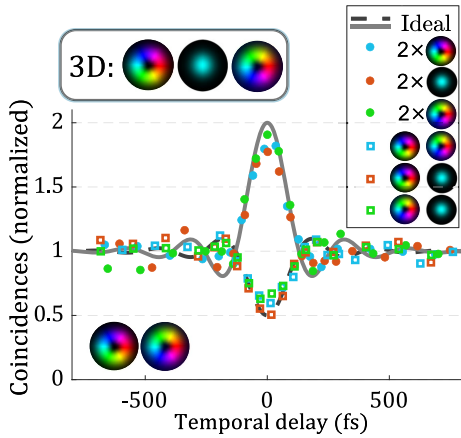


FIG. 3. Two-photon interference in a three-dimensional mode splitter. The two-photon input state, shown in the inset on the lower left, was sent into a balanced unitary \hat{U}_3 . The resulting interference was measured when projecting the photon pair onto every combination of our initial basis states. The ideal curves were calculated from the theoretically expected visibilities and the two-photon properties measured at the source. The omitted error bars and more experimental details can be found in the Supplemental Material [25].

and $38.3\% \pm 2.8\%$. Similarly to the two-dimensional case, projecting both photons onto the same mode with \hat{P}_{+1+1} , \hat{P}_{00} , or \hat{P}_{-1-1} , results in a twofold increase in coincidences. The corresponding measurements lead to visibilities $84.3\% \pm 5.6\%$, $77.2\% \pm 4.8\%$, and $94.7\% \pm 7.2\%$, respectively (see Fig. 3). For the high-dimensional interference curves, we display ideal curves instead of fits, to keep the figure simple and compare the data to theoretically expected results. The imperfect visibilities are likely due to small misalignments and imperfections in the unitary implemented with only three phase modulations for these increasingly complex transformation. For completeness, we also confirmed that this three-dimensional unitary works with superposition states, which is shown in the Supplemental Material [25].

Naturally, scaling these effects into higher-dimensional state spaces, i.e., realizing linear optical networks, is important for quantum information applications [13–17]. However, this scaling also provides some fundamentally interesting effects that cannot be observed in a classical HOM setting, i.e., a two-dimensional system. One such effect is anticoalescence, where two-photon interference causes an increase in coincidences when projecting the biphoton state onto two orthogonal spatial modes, while still having a separable state as an input. In three dimensions, this phenomena can be observed if either the input states or the unitary is prepared in an unbalanced superposition basis. An example of the latter has been

demonstrated using paths and an imperfect tritter [43], which could also be modeled as a lossy asymmetric beam splitter [44]. We demonstrate anticoalescence by exploiting the flexibility of our multiport, and compare the interference obtained with the balanced mode splitter \hat{U}_3 to an unbalanced unitary $\hat{U}_{\text{Rot}+3}$, while keeping the same two-photon state $|1, 0, 1\rangle$ as input and output. As already shown in Fig. 3, for the balanced mode splitter \hat{U}_3 we observe coalescence. However, when using the unbalanced mode splitter $\hat{U}_{\text{Rot}+3}$ we find an increase in coincidences with a visibility of $77.4\% \pm 6.4\%$ caused by anticoalescence [see Fig. 4(a)]. Because of the imperfections outlined earlier, our measured visibilities are slightly lower than the theoretically expected 100%. Because of the bosonic nature of photons, bunching is still the driving force of these interferences, which manifests as HOM dips when projecting on the two other orthogonal mode pairs (see Supplemental Material [25]). We further verified the same anticoalescence using the balanced unitary \hat{U}_3 and unbalanced superposition states, which can be found in the Supplemental Material [25].

When going beyond three dimensions, tuning the observed interference becomes easier since the mode splitter unitary can be kept balanced while changing its internal phases [43]. We demonstrate this tunability using a balanced four-dimensional mode splitter

$$\hat{U}_4 = \frac{1}{2} \begin{bmatrix} 1 & 1 & 1 & 1 \\ 1 & e^{i\varphi} & -1 & -e^{i\varphi} \\ 1 & -1 & 1 & -1 \\ 1 & -e^{i\varphi} & -1 & e^{i\varphi} \end{bmatrix}, \quad (2)$$

for which we adjust the internal phase values φ to 0, $\pi/2$, or π , corresponding to an anticoalescence, no interference, and coalescence, respectively. The chosen four-dimensional state space is spanned by the OAM modes with $\ell = \pm 2, \pm 1$. Although any two-mode combination of the mode set could have been used, we kept the same input state $|\Psi\rangle = |0\rangle_{-2}|1\rangle_{-1}|1\rangle_{+1}|0\rangle_{+2} = |0, 1, 1, 0\rangle$ and projected on the same output state, i.e., \hat{P}_{-1+1} , as before to show that the change in interference only stems from the different unitary operation. In our measurements [shown in Fig. 4(b)] we obtained a visibility of $75.0\% \pm 6.1\%$ for $\varphi = 0$, no significant interference for $\varphi = \pi/2$ and a visibility of $63.2\% \pm 6.4\%$ for $\varphi = \pi$. While not being perfect, the obtained visibilities are above the classical limit, with at least 95% confidence. We again attribute the discrepancy between theory and experiment to the limitations of our small MPLC system performing more complex transformations. Already in simulations, the limited number of phase screens leads to an increase in mode-independent loss, around 27%–37%, and a slightly unbalanced mode splitter. Although MPLC setups have been implemented using a larger number of phase

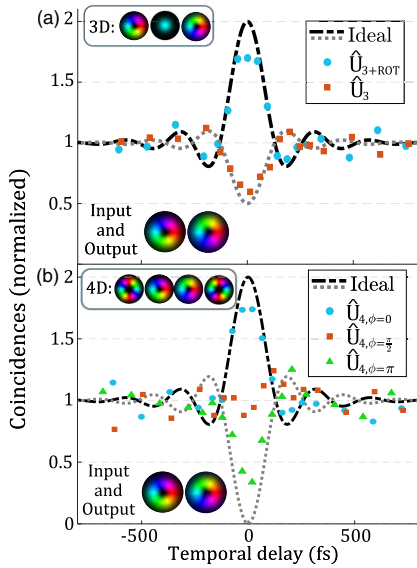


FIG. 4. Two-photon anticoalescence in a high-dimensional unitaries. The results in (a) show how imperfect coalescence in a three-dimensional state space can be changed to anticoalescence by changing to an unbalanced mode splitter unitary. Further, in (b), three different balanced four-dimensional mode splitters are used to tune the observed coalescence with the same input and output states. Definitions for the unitaries and error bars can be found in the Supplemental Material [25].

modulations on a single SLM [14,37], we refrained from doing so here due to the additional losses induced by every SLM reflection.

The multiphoton interference effects shown here, demonstrate that a reconfigurable spatial-mode multiport, implemented through MPLC, can be used in the quantum domain, opening up multiple new research avenues and quantum technological applications harnessing the benefits of spatial modes. The current limitation of our experimental scheme is the lossy method of generating the spatial modes [22] and the limited efficiency of our SLMs (75% efficiency per reflection), that limits the number of phase modulation planes. However, these limitations are only of a technical nature and can be tackled in the future with more expensive devices, e.g., high-quality deformable mirrors, and novel methods, e.g., lossless generation and detection of structured photons [35]. Because our scheme is intrinsically stable and can be fully automatized [14], scaling to large mode numbers, i.e., the realization of large linear optical networks along a single path, seems feasible. Additionally, other input states, such as entangled states or multipartite states, could be used to investigate more complex multiphoton interferences. The well-controlled two-photon interference can further be applied in

generating custom-tailored NOON states of spatial modes, studying complex quantum walks within the spatial-mode set [45], simplifying fundamental research endeavours such a high-dimensional multipartite entanglement [46], or applying spatial modes in complex quantum information tasks like photonic quantum processors [13,47], high-dimensional quantum teleportation [48], or Boson sampling [49].

The authors thank Marcus Huber, Mario Krenn, Shashi Prabhakar, and Lea Kopf for fruitful discussions. M. H. and R. F. acknowledge the support of the Academy of Finland through the Competitive Funding to Strengthen University Research Profiles (decision 301820) and the Photonics Research and Innovation Flagship (PREIN—decision 320165). M. H. also acknowledges support from the Magnus Ehrnrooth foundation through its graduate student scholarship. R. F. also acknowledges support from the Academy of Finland through the Academy Research Fellowship (Decision 332399).

* markus.hiekkamaki@tuni.fi

† robert.fickler@tuni.fi

- [1] C. K. Hong, Z. Y. Ou, and L. Mandel, Measurement of Subpicosecond time Intervals Between Two Photons by Interference, *Phys. Rev. Lett.* **59**, 2044 (1987).
- [2] F. Bouchard, A. Sit, Y. Zhang, R. Fickler, F. M. Miatto, Y. Yao, F. Sciarrino, and E. Karimi, Two-photon interference: The Hong-Ou-Mandel effect, [arXiv:2006.09335](https://arxiv.org/abs/2006.09335).
- [3] P. Kok, W. J. Munro, K. Nemoto, T. C. Ralph, J. P. Dowling, and G. J. Milburn, Linear optical quantum computing with photonic qubits, *Rev. Mod. Phys.* **79**, 135 (2007).
- [4] F. Xu, X. Ma, Q. Zhang, H.-K. Lo, and J.-W. Pan, Secure quantum key distribution with realistic devices, *Rev. Mod. Phys.* **92**, 025002 (2020).
- [5] S. Muralidharan, L. Li, J. Kim, N. Lütkenhaus, M. D. Lukin, and L. Jiang, Optimal architectures for long distance quantum communication, *Sci. Rep.* **6**, 20463 (2016).
- [6] V. Giovannetti, S. Lloyd, and L. Maccone, Advances in quantum metrology, *Nat. Photonics* **5**, 222 (2011).
- [7] D. Bouwmeester, J.-W. Pan, K. Mattle, M. Eibl, H. Weinfurter, and A. Zeilinger, Experimental quantum teleportation, *Nature (London)* **390**, 575 (1997).
- [8] N. Somaschi, V. Giesz, L. De Santis, J. C. Loredano, M. P. Almeida, G. Hornecker, S. L. Portalupi, T. Grange, C. Antón, J. Demory *et al.*, Near-optimal single-photon sources in the solid state, *Nat. Photonics* **10**, 340 (2016).
- [9] Y.-M. He, H. Wang, C. Wang, M.-C. Chen, X. Ding, J. Qin, Z.-C. Duan, S. Chen, J.-P. Li, R.-Z. Liu *et al.*, Coherently driving a single quantum two-level system with dichromatic laser pulses, *Nat. Phys.* **15**, 941 (2019).
- [10] D. Branning, W. P. Grice, R. Erdmann, and I. A. Walmsley, Engineering the Indistinguishability and Entanglement of Two Photons, *Phys. Rev. Lett.* **83**, 955 (1999).
- [11] A. Mohanty, M. Zhang, A. Dutt, S. Ramelow, P. Nussenzveig, and M. Lipson, Quantum interference

- between transverse spatial waveguide modes, *Nat. Commun.* **8**, 14010 (2017).
- [12] T. Kobayashi, R. Ikuta, S. Yasui, S. Miki, T. Yamashita, H. Terai, T. Yamamoto, M. Koashi, and N. Imoto, Frequency-domain Hong-Ou-Mandel interference, *Nat. Photonics* **10**, 441 (2016).
- [13] J. Carolan, C. Harrold, C. Sparrow, E. Martín-López, N. J. Russell, J. W. Silverstone, P. J. Shadbolt, N. Matsuda, M. Oguma, M. Itoh *et al.*, Universal linear optics, *Science* **349**, 711 (2015).
- [14] F. Brandt, M. Hiekkamäki, F. Bouchard, M. Huber, and R. Fickler, High-dimensional quantum gates using full-field spatial modes of photons, *Optica* **7**, 98 (2020).
- [15] C. Reimer, M. Kues, P. Roztockı, B. Wetzel, F. Grazioso, B. E. Little, S. T. Chu, T. Johnston, Y. Bromberg, L. Caspani *et al.*, Generation of multiphoton entangled quantum states by means of integrated frequency combs, *Science* **351**, 1176 (2016).
- [16] P. Imany, J. A. Jaramillo-Villegas, M. S. Alshaykh, J. M. Lukens, O. D. Odele, A. J. Moore, D. E. Laird, M. Qi, and A. M. Weiner, High-dimensional optical quantum logic in large operational spaces, *npj Quantum Inf.* **5**, 59 (2019).
- [17] S. Leedumrongwathanakun, L. Innocenti, H. Defienne, T. Juffmann, A. Ferraro, M. Paternostro, and S. Gigan, Programmable linear quantum networks with a multimode fibre, *Nat. Photonics* **14**, 139 (2020).
- [18] M. Erhard, R. Fickler, M. Krenn, and A. Zeilinger, Twisted photons: New quantum perspectives in high dimensions, *Light Sci. Appl.* **7**, 17146 (2018).
- [19] L. Allen, M. W. Beijersbergen, R. J. C. Spreeuw, and J. P. Woerdman, Orbital angular momentum of light and the transformation of Laguerre-Gaussian laser modes, *Phys. Rev. A* **45**, 8185 (1992).
- [20] G. Labroille, B. Denolle, P. Jian, P. Genevieux, N. Treps, and J.-F. Morizur, Efficient and mode selective spatial mode multiplexer based on multi-plane light conversion, *Opt. Express* **22**, 15599 (2014).
- [21] G. Weihs, M. Reck, H. Weinfurter, and A. Zeilinger, Two-photon interference in optical fiber multiports, *Phys. Rev. A* **54**, 893 (1996).
- [22] E. Bolduc, N. Bent, E. Santamato, E. Karimi, and R. W. Boyd, Exact solution to simultaneous intensity and phase encryption with a single phase-only hologram, *Opt. Lett.* **38**, 3546 (2013).
- [23] A. Mair, A. Vaziri, G. Weihs, and A. Zeilinger, Entanglement of the orbital angular momentum states of photons, *Nature (London)* **412**, 313 (2001).
- [24] M. Krenn, M. Malik, M. Erhard, and A. Zeilinger, Orbital angular momentum of photons and the entanglement of Laguerre-Gaussian modes, *Phil. Trans. R. Soc. A* **375**, 20150442 (2017).
- [25] See Supplemental Material at <http://link.aps.org/supplemental/10.1103/PhysRevLett.126.123601> for additional data, extended discussion on methods, raw data, and detailed description of the setup.
- [26] E. Nagali, L. Sansoni, F. Sciarrino, F. De Martini, L. Marrucci, B. Piccirillo, E. Karimi, and E. Santamato, Optimal quantum cloning of orbital angular momentum photon qubits through Hong-Ou-Mandel coalescence, *Nat. Photonics* **3**, 720 (2009).
- [27] E. Karimi, D. Giovannini, E. Bolduc, N. Bent, F. M. Miatto, M. J. Padgett, and R. W. Boyd, Exploring the quantum nature of the radial degree of freedom of a photon via Hong-Ou-Mandel interference, *Phys. Rev. A* **89**, 013829 (2014).
- [28] Y. Zhang, S. Prabhakar, C. Rosales-Guzmán, F. S. Roux, E. Karimi, and A. Forbes, Hong-Ou-Mandel interference of entangled Hermite-Gauss modes, *Phys. Rev. A* **94**, 033855 (2016).
- [29] M. Malik, M. Erhard, M. Huber, M. Krenn, R. Fickler, and A. Zeilinger, Multi-photon entanglement in high dimensions, *Nat. Photonics* **10**, 248 (2016).
- [30] Y. Zhang, F. S. Roux, T. Konrad, M. Agnew, J. Leach, and A. Forbes, Engineering two-photon high-dimensional states through quantum interference, *Sci. Adv.* **2**, e1501165 (2016).
- [31] V. D'Ambrosio, G. Carvacho, I. Agresti, L. Marrucci, and F. Sciarrino, Tunable Two-Photon Quantum Interference of Structured Light, *Phys. Rev. Lett.* **122**, 013601 (2019).
- [32] V. Giovannetti, S. Lloyd, and L. Maccone, Quantum-enhanced measurements: Beating the standard quantum limit, *Science* **306**, 1330 (2004).
- [33] S. Slussarenko, M. M. Weston, H. M. Chrzanowski, L. K. Shalm, V. B. Verma, S. W. Nam, and G. J. Pryde, Unconditional violation of the shot-noise limit in photonic quantum metrology, *Nat. Photonics* **11**, 700 (2017).
- [34] S. Prabhakar, C. Mabena, T. Konrad, and F. S. Roux, Turbulence and the Hong-Ou-Mandel effect, *Phys. Rev. A* **97**, 013835 (2018).
- [35] M. Hiekkamäki, S. Prabhakar, and R. Fickler, Near-perfect measuring of full-field transverse-spatial modes of light, *Opt. Express* **27**, 31456 (2019).
- [36] M. Hiekkamäki, S. Prabhakar, and R. Fickler, Wavefront matching code for transverse spatial mode conversion, <https://doi.org/10.5281/zenodo.3570622> (2019).
- [37] N. K. Fontaine, R. Ryf, H. Chen, D. T. Neilson, K. Kim, and J. Carpenter, Laguerre-Gaussian mode sorter, *Nat. Commun.* **10**, 1865 (2019).
- [38] M. W. Beijersbergen, L. Allen, H. E. L. O. Van der Veen, and J. P. Woerdman, Astigmatic laser mode converters and transfer of orbital angular momentum, *Opt. Commun.* **96**, 123 (1993).
- [39] J. G. Rarity, P. R. Tapster, and R. Loudon, Non-classical interference between independent sources, *J. Opt. B* **7**, S171 (2005).
- [40] R. Fickler, R. Lapkiewicz, S. Ramelow, and A. Zeilinger, Quantum entanglement of complex photon polarization patterns in vector beams, *Phys. Rev. A* **89**, 060301(R) (2014).
- [41] S. Yu and N.-L. Liu, Entanglement Detection by Local Orthogonal Observables, *Phys. Rev. Lett.* **95**, 150504 (2005).
- [42] O. Gühne and G. Tóth, Entanglement detection, *Phys. Rep.* **474**, 1 (2009).
- [43] K. Mattle, M. Michler, H. Weinfurter, A. Zeilinger, and M. Zukowski, Non-classical statistics at multipoint beam splitters, *Appl. Phys. B* **60**, S111 (1995).
- [44] R. Uppu, T. A. W. Wolterink, T. B. H. Tentrup, and P. W. H. Pinkse, Quantum optics of lossy asymmetric beam splitters, *Opt. Express* **24**, 16440 (2016).
- [45] M. Gräfe, R. Heilmann, M. Lebugle, D. Guzman-Silva, A. Perez-Leija, and A. Szameit, Integrated photonic quantum walks, *J. Opt.* **18**, 103002 (2016).

- [46] M. Erhard, M. Malik, M. Krenn, and A. Zeilinger, Experimental Greenberger–Horne–Zeilinger entanglement beyond qubits, *Nat. Photonics* **12**, 759 (2018).
- [47] A. Peruzzo, J. McClean, P. Shadbolt, M.-H. Yung, X.-Q. Zhou, P. J. Love, A. Aspuru-Guzik, and J. L. O’Brien, A variational eigenvalue solver on a photonic quantum processor, *Nat. Commun.* **5**, 4213 (2014).
- [48] Y.-H. Luo, H.-S. Zhong, M. Erhard, X.-L. Wang, L.-C. Peng, M. Krenn, X. Jiang, L. Li, N.-L. Liu, C.-Y. Lu *et al.*, Quantum Teleportation in High Dimensions, *Phys. Rev. Lett.* **123**, 070505 (2019).
- [49] H. Wang, Y. He, Y.-H. Li, Z.-E. Su, B. Li, H.-L. Huang, X. Ding, M.-C. Chen, C. Liu, J. Qin *et al.*, High-efficiency multiphoton boson sampling, *Nat. Photonics* **11**, 361 (2017).

Correction: The inline equation in the fourth paragraph contained an error and has been fixed. The seventh sentence of the caption to Fig. 2 was misworded (“standard errors” should read “standard deviations”), and similar changes have been made to the captions to Figs. S5 and S8 of the Supplemental Material.

PUBLICATION

II

Photonic Angular Superresolution Using Twisted N00N States

Markus Hiekkamäki, Frédéric Bouchard, and Robert Fickler

Physical Review Letters 127 (2021), p. 263601


Publication reprinted with the permission of the copyright holders.

Photonic Angular Superresolution Using Twisted N00N States

Markus Hiekkamäki^{1,*}, Frédéric Bouchard², and Robert Fickler^{1,†}

¹Tampere University, Photonics Laboratory, Physics Unit, Tampere FI-33720, Finland

²National Research Council of Canada, 100 Sussex Drive, Ottawa, Ontario K1A 0R6, Canada

 (Received 15 June 2021; revised 1 October 2021; accepted 16 November 2021; published 23 December 2021)

The increased phase sensitivity of N00N states has been used in many experiments, often involving photon paths or polarization. Here we experimentally combine the phase sensitivity of N00N states with the orbital angular momentum (OAM) of photons up to $100 \hbar$, to resolve rotations of a light field around its optical axis. The results show that both a higher photon number and larger OAM increase the resolution and achievable sensitivity. The presented method opens a viable path to unconditional angular supersensitivity and accessible generation of N00N states between any transverse light fields.

DOI: 10.1103/PhysRevLett.127.263601

During the past few decades, N00N states have been the focus of several studies where their potential was explored in different metrological applications [1–4]. Specifically, a N00N state refers to an extremal superposition of N quanta between two orthogonal modes, i.e., $(1/\sqrt{2})(|N, 0\rangle + |0, N\rangle)$ [3]. These states owe their usefulness to an increased phase sensitivity that an N -photon Fock state has in comparison to a single photon, or more classical states of light. The increased phase sensitivity means that a phase ϕ affects the Fock state $|N\rangle$ N times, changing the state to $e^{iN\phi}|N\rangle$, whereas classical states of light would only gain the phase ϕ [3]. This increase in phase sensitivity has been utilized in many proof-of-principle experiments, most commonly by preparing two photons in a superposition of two paths [1] or polarizations [2]. One notable example is the demonstration of an unconditional quantum advantage in sensitivity, using two-photon polarization N00N states [5].

Similarly to the phase sensitivity scaling with a photon number, the sensitivity in rotation measurements around the optical axis scales with the amount of helical twistedness in the wavefront of the light used [6]. This sensitivity is related to the rotational symmetry of the helically twisted wavefront of a light beam with nonzero orbital angular momentum (OAM). The amount of wavefront twistedness, or OAM, a photon can have is quantized to integer multiples ℓ of \hbar , and is theoretically unbounded [7], leading to a theoretically unbounded increase in measurement sensitivity. Experimentally, values of up to 10 010 quanta of OAM

were already demonstrated [8]; however, this value is bounded by the finite aperture of the optical system [9].

Theoretical and experimental studies have examined methods of combining the increased phase sensitivity of quantum states and the optimal rotation sensitivity of light beams with large OAM [10–14]. In these studies however, instead of experimentally implemented twisted N00N states, the authors used either squeezed light states, light directly from a spontaneous parametric down conversion (SPDC) source, or multiple paths for the photons with different OAM values to travel. These implementations lack the robustness and simplicity of a single-path operation which can be achieved with the recently introduced method for bunching photons into different OAM N00N states [15].

In this study, we experimentally demonstrate an increased rotation sensitivity of twisted N00N states along a single path. With our method, we are able to show the increased rotation sensitivity using N00N states with photon numbers 1 and 2, and OAM values up to $100 \hbar$. Our results show that twisted two-photon N00N states have the potential for an angular uncertainty scaling $\propto (1/\ell N)$, whereas classical light is limited to a scaling $\propto (1/\ell \sqrt{N})$ [10,13]. Although the amount of OAM is limited by the physical aperture, increasing the number of photons in a twisted N00N state has the potential to surpass any classical angular resolution limit. Due to the simplicity of the presented method, spatial mode N00N states with large OAM values and high efficiencies are achievable even with current technologies. As such, our work opens up novel ways to generate N00N states invoking the transverse spatial degree of freedom and offers a path to unconditional angular supersensitivity.

To create a two-photon twisted N00N state, two photons that have orthogonal transverse-spatial structures but are otherwise indistinguishable need to be brought into the same beam path. A unitary that transforms the modes into a

Published by the American Physical Society under the terms of the Creative Commons Attribution 4.0 International license. Further distribution of this work must maintain attribution to the author(s) and the published article's title, journal citation, and DOI.

mutually unbiased basis (MUB), i.e., a Hadamard operation \hat{H}_2 , then leads to a bunching of the two photons into the original spatial structures [15]. This interference is analogous to the well-known Hong-Ou-Mandel interference realized by a beam splitter transformation [16]. However, since the beam-splitter-like transformation \hat{H}_2 is unitary, the two photons stay orthogonal in a certain basis

$$\hat{H}_2|1, 1\rangle_{\ell, -\ell} = \frac{1}{\sqrt{2}}(|2, 0\rangle_{\ell, -\ell} - |0, 2\rangle_{\ell, -\ell}) = |1, 1\rangle_{M_1, M_2},$$

where M_i refer to the modes of another MUB of the OAM modes $\{\ell, -\ell\}$. Because of this feature, it is possible to include the beam-splitter-like operation into the state generation, before bringing the photons into the same beam path, while still achieving the same two-photon bunching and, thus, the same two-photon twisted N00N state. Interestingly, for larger photon numbers the process generates Holland-Burnett states that are also capable of overcoming the shot-noise limit [17].

To experimentally verify the efficacy of this method, we use an SPDC source to generate photon pairs and the setup shown in Fig. 1 (see Supplemental Material for details [18]). The photon pair is coupled out of single-mode fibers onto two separate regions of a spatial light modulator (SLM), as shown on the left side of Fig. 1, where the photons are structured using holographic phase and amplitude modulation [19,20]. The structured photons are then brought to the same path with a beam splitter to enable bunching into OAM structures. To measure the two-photon state, a second beam splitter probabilistically separates the photons, and a second SLM (SLM2) is used in conjunction with two single-mode fibers to filter the spatial structures of the photons independently [21,22]. Both of the SLMs that were used were wavefront corrected [23]. For single-photon N00N states, only one input and output fiber were used, and the other photon was detected at the two-photon source, to herald a single-photon state [24].

To confirm that the photons bunch into a N00N state, we first prepare a two-photon N00N state with an OAM value of $\ell = \pm 1$, and verify its quantum correlations using an entanglement witness [25,26]. Measuring the state in all three MUBs, we achieve a witness value of $w = 2.92 \pm 0.02$, which is greater than the maximal value of $w = 1$ for separable states and close to the maximum value of $w = 3$ of the witness for maximally entangled states.

After this initial confirmation, we proceed to examine the angular resolution and sensitivity of these OAM N00N states using our measurement scheme. In these measurements, we prepare heralded single photons and two-photon N00N states with OAM values $|\ell| = \{1, 2, 3, 5, 10, 25, 50, 100\}$. For $|\ell| < 10$, we use mode carving [19] and intensity flattening [21] to create and measure the structures, respectively. The amplitude modulation implemented in these procedures is needed to get as close as possible to the MUB states of OAM light fields. The OAM states have a complex field structure $E_\ell(\theta) \propto e^{i\ell\theta}$, where θ is the azimuthal coordinate. Hence, the MUB structures are of the form $E_{M_1/M_2}(\theta) \propto (e^{i\ell\theta} \pm e^{-i\ell\theta})$ and are often called petal beams [27]. Examples of these structures for $\ell = \pm 2$ are shown in the insets of Fig. 1. When generating photons with $|\ell| \geq 10$, no amplitude modulation is required as the spatial structures are sufficiently filtered by the limited aperture of our system. Thus, simple phase imprinting [20] and phase flattening [22] are used to generate and measure the desired modes, respectively.

To demonstrate angular superresolution, we simulate the rotation of our photon structures by rotating the measurement holograms on SLM2. As with the more common two-photon Mach-Zehnder interferometer, a second Hadamard transformation is needed to detect the phase change. In the case of OAM modes, the second Hadamard transformation can be performed in the measurement by simply projecting the photons onto the petal mode basis (see Supplemental Material [18]). Hence, the two-photon state was measured

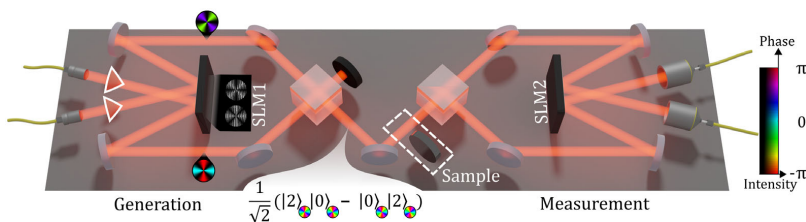


FIG. 1. Conceptual image of the experimental setup. Two holograms are used on the first SLM (SLM1) to imprint the wanted structures onto each photon, independently. The two photons are then overlapped using a beam splitter, to enable photon bunching into the same spatial structure, hence, allowing for a single beam operation when probing a sample. To measure the two-photon state, the photons are separated with a beam splitter and sent to SLM2 where another set of holograms are used to measure the structure of each photon (see main text for details). The insets show an example of the holograms displayed on SLM1 to generate an OAM N00N state with $\ell = \pm 2$, an example of a sample position, and the transverse field structures the photons have at different points of the setup, visualized by a two-dimensional colormap (see color bar on right).

by projecting the photons on orthogonal petal structures, which can only result in an interference curve with perfect visibility in the case of bunching. Interestingly, projecting both photons on identical petal structures can produce a perfect fringe visibility irrespective of bunching, although with an increased amplitude in the case of bunching (see Supplemental Material [18]).

Since rotating the light field by an angle φ induces a phase $e^{i\ell N\varphi}$ on an N -photon Fock state [10], the theoretically expected optimal detection rate is $\langle \hat{M} \rangle = (M/2) [1 - \cos(2N\ell\varphi)]$, where M is the number of repetitions of the measurement and N is the number of photons used in the NOON state. From the detection rate, the theoretical scaling of the angular uncertainty can be expressed as

$$\Delta\varphi = \frac{\langle \Delta \hat{M} \rangle}{|\partial \langle \hat{M} \rangle / \partial \varphi|} = \frac{1}{2\sqrt{MN}\ell}, \quad (1)$$

which saturates the quantum Cramér-Rao bound. For derivations of Eq. (1) and the bound, based on Refs. [10,28–30], see Supplemental Material [18].

The rotation measurements with $\ell = \{\pm 1, \pm 10, \pm 100\}$ are shown in Fig. 2. The figure shows that increasing the amount of OAM increases the achievable resolution, and changing from a single-photon to a two-photon NOON state doubles the resolution.

To further analyze the measured data, we estimate the Fisher information and angular precision for each measurement. Therefore, we first fit a curve to each set of the measured data using a weighted nonlinear least squares fit (each point is weighted by the reciprocal of the measured variance). The fitted curve is

$$\frac{A}{2} \left[1 - \cos \left(2N\ell \frac{\pi}{180^\circ} \varphi - c \right) \right] + D, \quad (2)$$

where A is the amplitude of the cosine curve, D is the offset, and c sets the position of 0° rotation. Hence, $[A/(A+2D)]$ gives an estimate of the visibility of the curve, based on the fit. For the single-photon measurements, we obtain an average visibility of 0.999, whereas for the two-photon measurements the corresponding value is 0.956 averaged over all measurements. The maximum standard error for the visibilities is 0.011, calculated for the two-photon $\ell = \pm 100$ state, from the confidence intervals of the fitting parameters.

From these fits and the estimated system efficiencies (around 0.015 for a single photon with $\ell = 1$ and 0.002 when $\ell = 100$) we are able to derive the expected Fisher information (see Supplemental Material [18]). We also calculate the angular uncertainty using

$$\Delta\varphi = \frac{\Delta M(\varphi)}{AN\ell \frac{\pi}{180^\circ} \sin(2N\ell \frac{\pi}{180^\circ} \varphi - c)}, \quad (3)$$

where $\Delta M(\varphi)$ is the standard deviation for each measurement angle calculated from around 25 repetitions,

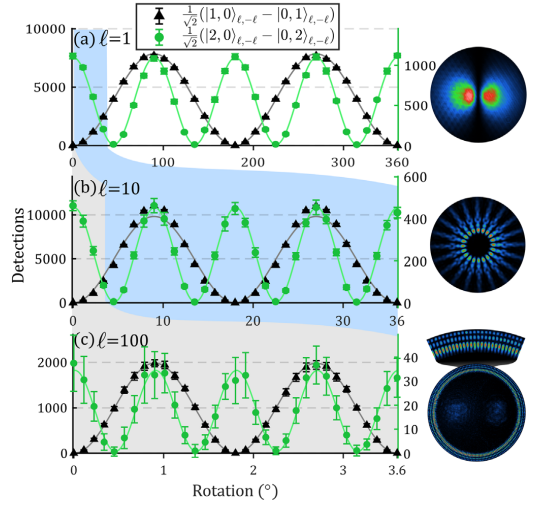


FIG. 2. Detected single photons and two-photon coincidences as a function of rotation angle. The single photons were prepared in the modes shown in the insets (insets show false-color images of structures taken with camera and laser light), and the corresponding two-photon NOON states were created by imprinting the same structure on one photon and its orthogonal pair (same structure rotated by $180^\circ/2\ell$) on the other. The plots in (a)–(c) show single photon (two-photon) counts within integration times of 2 s (3 s), 1 s (3 s), and 2 s (8 s) and OAM values of $\ell = 1, 10$, and 100 , respectively. The error bars have been calculated as standard deviations from at least 19 repetitions of the measurement at each point, and the solid lines are fits of the form shown in Eq. (2). The decreased period between oscillations shows the angular superresolution achieved with the two-photon NOON states [31]. For the two-photon measurements, accidental coincidences have been subtracted.

depending on the photon number and OAM value. The Fisher information and angular precision are shown in Fig. 3 for $\ell = 100$ and in the Supplemental Material [18] for $\ell = 1$.

Plots (a) and (c) in Fig. 3 show that the expected Fisher information curves follow the reciprocal of the rotation angle variance, meaning that the results are close to the Cramér-Rao bound of our specific state measurement [4]. Similarly, the expected angular uncertainties mostly agree with the measured angular uncertainties. This indicates that the achieved precision is close to the maximum precision bounded by Poissonian noise. The differences between the expected curves and measured data stem from the limited number of repetitions used to calculate the standard deviation, the decoupling of the system during long measurements, and differences in system losses due to different bandwidths of our single-photon source and the laser used in characterization. The change in precision

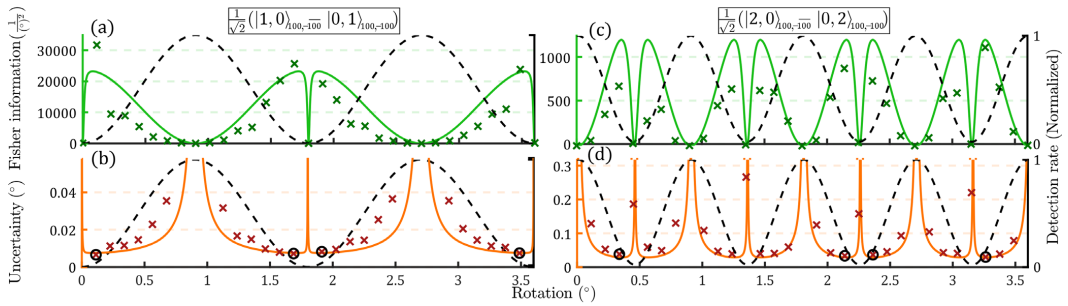


FIG. 3. Fisher information and angular uncertainty for $\ell = 100$ N00N states. On the upper row, the continuous green line is the Fisher information multiplied by the estimate for the total number of heralded single photons (or photon pairs) before losses. The green crosses are the reciprocal of the variance calculated from Eq. (3). On the bottom row, the continuous curves are calculated using Eq. (3) and Poissonian errors calculated from the fit. The red crosses are the experimentally determined uncertainties, calculated using Eq. (3). Plots (a) and (b) display the heralded single-photon data, and (c) and (d) contain two-photon data. In all graphs, the black dashed lines depict the interference curves for reference. On the bottom row, the uncertainty values that have been circled are used for calculating the respective sensitivities in Fig. 4.

caused by errors that were larger than Poissonian is especially apparent with the $\ell = 100$ measurements where a small drift over time has a comparatively large effect on the alignment of the small structures of the transverse field.

Finally, we compare the sensitivities that are achievable with two-photon N00N states to single-photon sensitivities, using different values of OAM. Figures 3(c) and 3(d) show that the best angular precision tends to be found at the same values of φ where the Fisher information is maximized. Therefore, to quantify the achievable sensitivities with different values of N and ℓ , we take the four smallest values of angular uncertainty $\Delta\varphi$ from each measurement, close to the point of maximum Fisher information. We then calculate the reciprocal for each of these values and define it as the sensitivity. To be able to compare sensitivities between different measurements, we normalize them by dividing each value $\Delta\varphi$ by $(\sqrt{A+D}/A)$, which removes the dependence of $\Delta\varphi$ on the varying number of detections in each measurement. These values are plotted in Fig. 4, along with theoretically expected maximum sensitivities for the measurement scheme used.

Fig. 4 shows that the measured two-photon states are more sensitive than their one-photon counterparts, although the theoretical scaling was not reached with two-photon states with large OAM. This discrepancy is caused by the nonperfect visibilities of the measured interference curves, in addition to the increasing complexity of the structures and their decreasing efficiencies, causing the alignment to be more sensitive while requiring longer measuring times. As a result, a slow misalignment over time has a larger effect on the variability of detection rates over the repeated measurements.

In the presented experiment, we created twisted one- and two-photon N00N states and verified the scaling they enable for angular resolution and sensitivity, when

increasing the photon number or OAM. In order to verify these properties, we rotated the measuring hologram on a SLM to simulate a rotation of the light field. Hence, the method could be directly applied to precisely aligning two rotational reference frames, e.g., in a communication channel [13]. However, in order to apply the method for

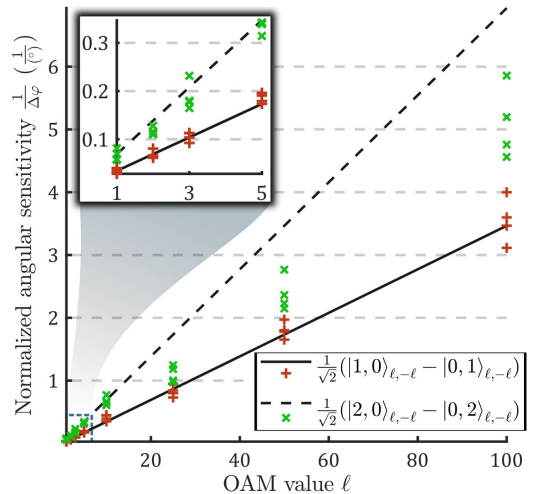


FIG. 4. Measurement sensitivities of single-photon and two-photon N00N states. The theoretical curves are calculated using Poissonian errors and a visibility of 0.9999 for the cosine curve introduced in Eq. (2). The crosses represent the four normalized sensitivities calculated from the uncertainty values chosen from each measurement. The mostly linear dependence of $1/\Delta\varphi$ on OAM follows the scaling of angular uncertainty introduced in Eq. (1).

measuring rotations caused by a separate system, the probed sample needs to be the one providing an OAM-dependent phase onto our two-photon state. This could be achieved by embedding an image rotator (e.g., a Dove prism) into the object whose rotation we want to measure, or by probing samples that interact with the N00N state by inducing an OAM-dependent phase which is contingent upon some property of the sample. Hence, the scheme is not restricted to only measuring rotations of a light field or reference frame, but can be used to measure any OAM-dependent phase changes. Additionally, since adding photons into the N00N state can be done irrespective of the aperture of the system, the increased angular resolution provided by a N00N state might be beneficial in tasks with a limited aperture size. However, in order to push the limits of achievable sensitivity with this measurement scheme, the system losses need to be reduced and a more appropriate estimator for the rotation angle should be devised [5,32].

In summary, we showed that by structuring and overlapping two photons, a high-fidelity two-photon N00N state can be created between any two high-OAM spatial structures. With this method, we are able to bunch two photons into modes with up to OAM $100 \hbar$, with minimal experimental complexity. For future implementations, improving the method's efficiency would be key in pushing the achievable sensitivity. The current losses are caused by the methods used for generation and detection, as well as the probabilistic overlapping and separation of the photon pair. To show a quantum advantage over a lossless classical system with perfect visibility, the condition $\eta^N V^2 N > 1$, introduced in references [5,31], needs to be met. With the average visibility $V = 0.956$ for our two-photon rotation sensing, the single-photon efficiency needs to be $\eta > 0.74$ to overcome the shot-noise limit. However, the efficiency of the system could be increased by using methods that are, in principle, lossless for preparing and measuring the spatial modes [33], and for combining the two photons into the same beam path [34,35].

The authors thank Shashi Prabhakar, Rafael F. Barros, and Lea Kopf for fruitful discussions. M. H. and R. F. acknowledge the support of the Academy of Finland through the Competitive Funding to Strengthen University Research Profiles (Decision 301820) (Grant No. 308596), and the Photonics Research and Innovation Flagship (PREIN—Decision 320165). M. H. also acknowledges support from the Doctoral School of Tampere University and the Magnus Ehrnrooth Foundation through its graduate student scholarship. F. B. acknowledges support from the National Research Council's High Throughput Secure Networks challenge program and the Joint Centre for Extreme Photonics. R. F. also acknowledges support from the Academy of Finland through the Academy Research Fellowship (Decision 332399).

- *markus.hiekkamaki@tuni.fi
 †robert.fickler@tuni.fi
- [1] J. G. Rarity, P. R. Tapster, E. Jakeman, T. Larchuk, R. A. Campos, M. C. Teich, and B. E. A. Saleh, Two-Photon Interference in a Mach-Zehnder Interferometer, *Phys. Rev. Lett.* **65**, 1348 (1990).
 - [2] A. Kuzmich and L. Mandel, Sub-shot-noise interferometric measurements with two-photon states, *Quantum Semiclassical Opt.* **10**, 493 (1998).
 - [3] J. P. Dowling, Quantum optical metrology—the lowdown on high-N00N states, *Contemp. Phys.* **49**, 125 (2008).
 - [4] E. Polino, M. Valeri, N. Spagnolo, and F. Sciarrino, Photonic quantum metrology, *AVS Quantum Sci.* **2**, 024703 (2020).
 - [5] S. Slussarenko, M. M. Weston, H. M. Chrzanowski, L. K. Shalm, V. B. Verma, S. Woo Nam, and G. J. Pryde, Unconditional violation of the shot-noise limit in photonic quantum metrology, *Nat. Photonics* **11**, 700 (2017).
 - [6] S. M. Barnett and R. Zambrini, Resolution in rotation measurements, *J. Mod. Opt.* **53**, 613 (2006).
 - [7] M. Erhard, R. Fickler, M. Krenn, and A. Zeilinger, Twisted photons: New quantum perspectives in high dimensions, *Light Sci. Appl.* **7**, 17146 (2018).
 - [8] R. Fickler, G. Campbell, B. Buchler, P. Koy Lam, and A. Zeilinger, Quantum entanglement of angular momentum states with quantum numbers up to 10,010, *Proc. Natl. Acad. Sci. U.S.A.* **113**, 13642 (2016).
 - [9] M. J. Padgett, F. M. Miatto, M. P. J. Lavery, A. Zeilinger, and R. W. Boyd, Divergence of an orbital-angular-momentum-carrying beam upon propagation, *New J. Phys.* **17**, 023011 (2015).
 - [10] A. Kumar Jha, G. S. Agarwal, and R. W. Boyd, Super-sensitive measurement of angular displacements using entangled photons, *Phys. Rev. A* **83**, 053829 (2011).
 - [11] R. Fickler, R. Lapkiewicz, W. N. Plick, M. Krenn, C. Schaeff, S. Ramelow, and A. Zeilinger, Quantum entanglement of high angular momenta, *Science* **338**, 640 (2012).
 - [12] K. Liu, C. Cai, J. Li, L. Ma, H. Sun, and J. Gao, Squeezing-enhanced rotating-angle measurement beyond the quantum limit, *Appl. Phys. Lett.* **113**, 261103 (2018).
 - [13] V. D'ambrosio, N. Spagnolo, L. Del Re, S. Slussarenko, Y. Li, L. Chuan Kwek, L. Marrucci, S. P. Walborn, L. Aolita, and F. Sciarrino, Photonic polarization gears for ultra-sensitive angular measurements, *Nat. Commun.* **4**, 1 (2013).
 - [14] Y. Ming, J. Tang, Z.-x. Chen, F. Xu, L.-j. Zhang, and Y.-q. Lu, Generation of N00N state with orbital angular momentum in a twisted nonlinear photonic crystal, *IEEE J. Sel. Top. Quantum Electron.* **21**, 225 (2014).
 - [15] M. Hiekkamäki and R. Fickler, High-Dimensional Two-Photon Interference Effects in Spatial Modes, *Phys. Rev. Lett.* **126**, 123601 (2021).
 - [16] C. K. Hong, Z. Y. Ou, and L. Mandel, Measurement of Subpicosecond Time Intervals Between Two Photons by Interference, *Phys. Rev. Lett.* **59**, 2044 (1987).
 - [17] A. Datta, L. Zhang, N. Thomas-Peter, U. Dörner, B. J. Smith, and I. A. Walmsley, Quantum metrology with imperfect states and detectors, *Phys. Rev. A* **83**, 063836 (2011).

- [18] See Supplemental Material at <http://link.aps.org/supplemental/10.1103/PhysRevLett.127.263601> for detailed derivations, additional data, and a detailed description of the experimental setup.
- [19] E. Bolduc, N. Bent, E. Santamato, E. Karimi, and R. W. Boyd, Exact solution to simultaneous intensity and phase encryption with a single phase-only hologram, *Opt. Lett.* **38**, 3546 (2013).
- [20] A. Forbes, A. Dudley, and M. McLaren, Creation and detection of optical modes with spatial light modulators, *Adv. Opt. Photonics* **8**, 200 (2016).
- [21] F. Bouchard, N. Herrera Valencia, F. Brandt, R. Fickler, M. Huber, and M. Malik, Measuring azimuthal and radial modes of photons, *Opt. Express* **26**, 31925 (2018).
- [22] A. Mair, A. Vaziri, G. Weihs, and A. Zeilinger, Entanglement of the orbital angular momentum states of photons, *Nature (London)* **412**, 313 (2001).
- [23] A. Jesacher, A. Schwaighofer, S. Fürhapter, C. Maurer, S. Bernet, and M. Ritsch-Marte, Wavefront correction of spatial light modulators using an optical vortex image, *Opt. Express* **15**, 5801 (2007).
- [24] C. K. Hong and L. Mandel, Experimental Realization of a Localized One-Photon State, *Phys. Rev. Lett.* **56**, 58 (1986).
- [25] O. Gühne and G. Tóth, Entanglement detection, *Phys. Rep.* **474**, 1 (2009).
- [26] R. Fickler, R. Lapkiewicz, S. Ramelow, and A. Zeilinger, Quantum entanglement of complex photon polarization patterns in vector beams, *Phys. Rev. A* **89**, 060301(R) (2014).
- [27] I. A. Litvin, S. Ngcobo, D. Naidoo, K. Ait-Ameur, and A. Forbes, Doughnut laser beam as an incoherent superposition of two petal beams, *Opt. Lett.* **39**, 704 (2014).
- [28] M. O. Scully and J. P. Dowling, Quantum-noise limits to matter-wave interferometry, *Phys. Rev. A* **48**, 3186 (1993).
- [29] R. Demkowicz-Dobrzański, M. Jarzyna, and J. Kołodyński, Quantum limits in optical interferometry, *Prog. Opt.* **60**, 345 (2015).
- [30] G. Grynberg, A. Aspect, and C. Fabre, *Introduction to Quantum Optics: From the Semi-Classical Approach to Quantized Light* (Cambridge University Press, Cambridge, England, 2010), Chap. 4B, pp. 332–333.
- [31] K. J. Resch, K. L. Pregnell, R. Prevedel, A. Gilchrist, G. J. Pryde, J. L. O'Brien, and A. G. White, Time-Reversal and Super-Resolving Phase Measurements, *Phys. Rev. Lett.* **98**, 223601 (2007).
- [32] A. Lyons, G. C. Knee, E. Bolduc, T. Roger, J. Leach, E. M. Gauger, and D. Faccio, Attosecond-resolution Hong-Ou-Mandel interferometry, *Sci. Adv.* **4**, eaap9416 (2018).
- [33] M. Hiekkämäki, S. Prabhakar, and R. Fickler, Near-perfect measuring of full-field transverse-spatial modes of light, *Opt. Express* **27**, 31456 (2019).
- [34] G. Labroille, B. Denolle, P. Jian, P. Genevieux, N. Treps, and J.-F. Morizur, Efficient and mode selective spatial mode multiplexer based on multi-plane light conversion, *Opt. Express* **22**, 15599 (2014).
- [35] N. K. Fontaine, R. Ryf, H. Chen, D. T. Neilson, K. Kim, and J. Carpenter, Laguerre-Gaussian mode sorter, *Nat. Commun.* **10**, 1865 (2019).

PUBLICATION

III

Observation of the quantum Gouy phase

Markus Hiekkamäki, Rafael F. Barros, Marco Ornigotti, and Robert Fickler

Nature Photonics 16 (2022), pp. 828–833

Publication reprinted with the permission of the copyright holders.

Observation of the quantum Gouy phase

Received: 19 May 2022

Accepted: 17 August 2022

Published online: 6 October 2022

 Check for updates

 Markus Hiekkamäki , Rafael F. Barros , Marco Ornigotti  & Robert Fickler 

Controlling the evolution of photonic quantum states is crucial for most quantum information processing and metrology tasks. Due to its importance, many mechanisms of quantum state evolution have been tested in detail and are well understood; however, the fundamental phase anomaly of evolving waves, called the Gouy phase, has had a limited number of studies in the context of elementary quantum states of light, especially in the case of photon number states. Here we outline a simple method for calculating the quantum state evolution upon propagation and demonstrate experimentally how this quantum Gouy phase affects two-photon quantum states. Our results show that the increased phase sensitivity of multi-photon states also extends to this fundamental phase anomaly and has to be taken into account to fully understand the state evolution. We further demonstrate how the Gouy phase can be used as a tool for manipulating quantum states of any bosonic system in future quantum technologies, outline a possible application in quantum-enhanced sensing, and dispel a common misconception attributing the increased phase sensitivity of multi-photon quantum states solely to an effective de Broglie wavelength.

The wave dynamics dictating the evolution of quantum states is of utmost importance in both fundamental studies of quantum systems and quantum technological applications. For photons, the evolution of their spatial structure has been the key in a plethora of promising techniques for quantum communication^{1,2}, information processing^{3,4}, simulation⁵ and metrology⁶. One particular feature of a converging wave travelling through its focus is the acquisition of an additional phase shift when compared with a collimated beam or a plane wave travelling the same distance. This effect, which is known as the Gouy phase, was first observed and described by Gouy more than a century ago^{7,8}. Although the phenomenon is well established and can be described through methods in physical optics^{9,10}, the Gouy phase continues to be the topic of studies discussing its underlying physical origin by linking it to properties such as the geometry of the focus, geometric phases and the uncertainty principle^{9,11–18}. In addition to the continued interest aiming at providing an intuition for the phenomenon, this phase anomaly is often harnessed to realize tools in optics^{19–22}.

Despite the Gouy phase being a general wave phenomenon, studies investigating its role in quantum state evolution have been limited to a few matter wave studies^{23–27} and spatially separated photon pairs^{28,29}. Although these demonstrations use (locally) single quantum systems

and thus observe the effect known for classical light waves, more complex quantum states consisting of multiple identical quantum systems (that is, bosonic systems with multiple excitations) have not been studied before. We term the specific phase acquired by such quantum states the quantum Gouy phase.

In general, any phase accrued by a mode of a photonic quantum system leads to a photon-number dependent phase for the quantum state. This means that whereas a single photon or a classical field would acquire a phase ϕ upon propagation, when N -photons occupy the same mode ($|N\rangle$), the quantum state is left with N times the same phase, that is, $\exp(iN\phi)|N\rangle$ ³⁰. This increased phase sensitivity of photon number states is utilized in so-called NOON states, which have garnered popularity due to their potential to push the sensitivity of measurements to what is considered the absolute physical limit³¹. NOON states can be compactly expressed for two orthogonal modes p and p' as

$$|\Psi\rangle = \frac{1}{\sqrt{2}} (|N\rangle_p |0\rangle_{p'} - |0\rangle_p |N\rangle_{p'}). \quad (1)$$

Hence, the enhancement in measurement sensitivity is enabled by the phase difference between the two components being N times the phase

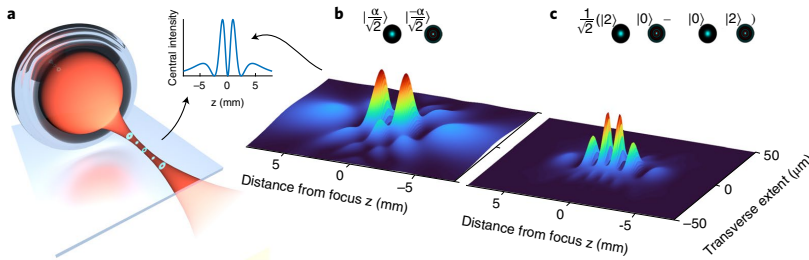


Fig. 1 | Observing the quantum Gouy phase through a changing on-axis interference along the propagation direction. **a**, Conceptual image of the observation scheme. The image displays the intensity structure of a superposition of a radial mode with $p' = 4$ and a Gaussian reference ($p = 0$) at different distances from the focus. The inset shows the intensity of the field on the optical axis. **b**, Intensity of a classical light beam prepared in the same

superposition as in **a**, with a Gaussian waist $w_0 = 25 \mu\text{m}$ and $z_0 = 0$. **c**, Spatially varying two-photon probability for a two-photon NOON state prepared in the same radial modes as in **a** and **b**. To make this structure visible, we post-select for cases in which the two photons exist in the same position using the projection $P(x, y, z) = |(\Psi(z))_{2,xy}|^2$. For **b** and **c**, the intensities/probabilities are calculated on a plane cutting through the optical axis (see **a** for reference).

difference between the underlying modes. More importantly, using such a NOON state configuration allows for the study of the speed-up of the quantum Gouy phase compared with the classical case.

In the present work we describe theoretically how an N -photon number state evolves upon propagation and verify experimentally the speed-up of the quantum Gouy phase with two-photon NOON states through interference in the transverse structure of a bi-photon. We further show that the quantum Gouy phase speed-up can be applied to super-resolving longitudinal displacement measurements using the quantum Fisher information (QFI) formalism and solidifying its link to the uncertainty interpretation of the Gouy phase¹². Finally, we show that our results for N -photon states cannot be simulated by classical light with a λ/N wavelength, demonstrating that the often-used effective de Broglie wavelength approach for multi-photon states, although useful in specific cases^{32–34}, is not always accurate. As such, our work brings the fundamental wave feature of the Gouy phase to the quantum domain, thereby opening the path to its utilization in quantum technological applications through its unique quantum state manipulation properties.

Probing the quantum Gouy phase

An interferometric measurement scheme can be used to observe the quantum Gouy phase of N -photons. We chose to use the transverse-spatial modes of paraxial light beams as the different arms of the interferometric scheme, where one mode acts as the required reference arm. More specifically, we used Laguerre–Gaussian (LG) modes, which are a family of orthogonal solutions to the paraxial wave equation in cylindrical coordinates³⁵. In the case of a classical monochromatic field, the Gouy phase of these modes evolves as³⁵

$$\Phi_G(z) = -(2p + |\ell| + 1) \arctan\left(\frac{2(z - z_0)}{kw_0^2}\right), \quad (2)$$

where z is the propagation distance, k is the wavenumber, ℓ is an integer giving the number of orbital angular momentum quanta per photon, p is a positive integer defining the radial transverse structure of the field, w_0 is the beam waist defining the transverse extent of the beam at its focus, and z_0 gives the position of the beam focus along the optical axis. As the Gouy phase depends on the mode order $S = 2p + |\ell| + 1$, its anomalous phase behaviour can be observed through the change of the transverse structure during propagation when the light is in a superposition of spatial modes of different mode orders³⁶. For radial modes, which are LG modes with $\ell = 0$, this change results in a varying intensity along the optical axis (as can be seen in Fig. 1a); thus, to probe the quantum Gouy phase and distinguish it from its classical counterpart, we study the superposition of a Gaussian reference mode

($p = 0$) and different higher-order radial modes in both the classical domain and the aforementioned quantum setting, that is, a NOON state superposition. By measuring the change in intensity and two-photon detection rate, respectively, observed in a single-mode fibre (SMF) scanned through the focus, we are able to directly observe the speed-up of the quantum Gouy phase.

Theoretical evolution upon propagation

In our measurement scheme, we expect the propagation to result in a photon number-dependent Gouy phase when the state $|N\rangle_p$ is translated through a focus. To verify these expectations theoretically, we start with N photons occupying a monochromatic paraxial mode at a position $z = 0$, with a complex field structure $u_{\ell p}(\boldsymbol{\rho}, 0)$. To translate the mode along the optical axis, we apply the translation operator $e^{ip_z z/\hbar}$ to the mode in the angular spectrum representation, in which the quantized mode of light can be expressed as

$$\hat{a}_{\ell p}^\dagger(0) = \int \int F_{\ell p}(\boldsymbol{\kappa}, 0) \hat{a}^\dagger(\boldsymbol{\kappa}) d^2\boldsymbol{\kappa}, \quad (3)$$

where $F_{\ell p}(\boldsymbol{\kappa}, 0)$ represents the normalized complex amplitude of the plane wave mode with transverse wave vector $\boldsymbol{\kappa}$, and $\hat{a}^\dagger(\boldsymbol{\kappa})$ is the corresponding operator density^{37,38}. After applying the translation operator, the mode takes the form

$$\hat{a}_{\ell p}^\dagger(z) = \int \int F_{\ell p}(\boldsymbol{\kappa}, 0) e^{-ik_z(z)} \hat{a}^\dagger(\boldsymbol{\kappa}) d^2\boldsymbol{\kappa}, \quad (4)$$

which is identical to the initial mode being propagated by z using the angular spectrum method (ASM)³⁹. We thus see that the quantized mode evolves identically to a classical light field, that is, the propagated LG mode has an identical spatial structure $u_{\ell p}(\boldsymbol{\rho}, z)$ that only differs by the propagation-related changes to the wavefront curvature and beam radius. Due to the beam evolving according to the ASM, we can extract the Gouy phase evolution by defining a new mode $\hat{b}_{\ell p}(z)$ —which has the structure of the field after translation—without the accumulated Gouy phase, that is, $u_{\ell p}(\boldsymbol{\rho}, z) e^{-ik_z z} e^{i\Phi_G(z)}$. Using this new mode, we can express the mode after propagation as a single mode with a phase

$$\hat{a}_{\ell p}^\dagger(z) = \hat{b}_{\ell p}^\dagger(z) e^{-i\Phi_G(z)}. \quad (5)$$

We can then simply state the Gouy phase evolution of an N -photon Fock state as

$$|N\rangle_{\ell p; 0} \rightarrow e^{-iNkz - iN\Phi_G(z)} |N\rangle_{\ell p; z}, \quad (6)$$

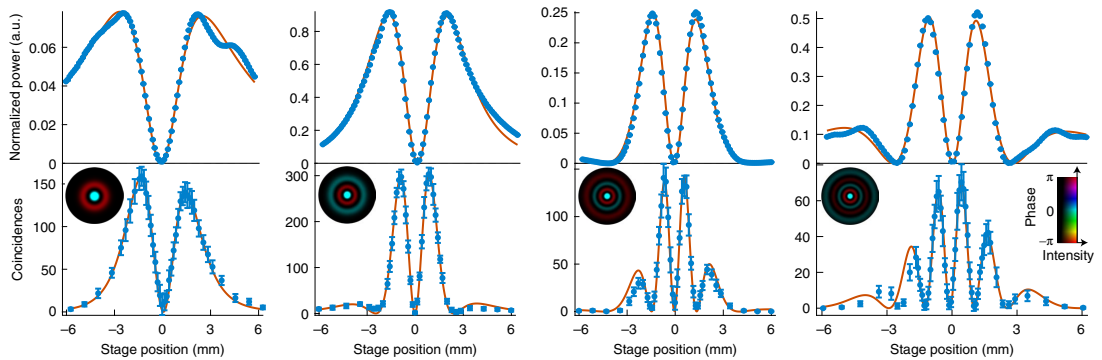


Fig. 2 | Comparison of on-axis interference along the propagation direction for classical light and two-photon NOON states. The error bars show the mean value \pm s.d., solid lines are fits, and the insets show images of the corresponding radial modes with index p' . The upper row contains laser data with 100 repetitions per measurement point, whereas the lower row shows two-photon coincidence measurements. Each two-photon data point was corrected for accidental coincidence detection and measured 25 times with an integration

time of 28 s for $p' = \{1, 2, 4\}$ and 24 s for $p' = 3$. The fits are nonlinear least-squares fits of the form described in the main text. We aimed to keep the beam waist radius at $25 \mu\text{m}$ in all measurements to keep the data comparable; however, the fits show that the beam waist was slightly larger for higher-order modes, varying between $24.95 \mu\text{m}$ and $26.81 \mu\text{m}$. A negative stage position labels that the SMF collecting the light was between the focus and the lens.

which explicitly contains the photon number dependent Gouy phase evolution. See Supplementary Section 1 for a detailed derivation.

Experiment

We first prepared laser light in a superposition of the Gaussian reference mode and one of the higher-order radial modes. The structuring of the laser beam was performed with a single hologram on a spatial light modulator (SLM) by using a holographic method commonly known as mode carving⁴⁰. After structuring, the beam was imaged one focal distance away from a 75 mm lens, which performs an optical Fourier transform on the transverse structure while focusing³⁹. As the transverse structure and its Fourier transform are identical for LG modes, the beam structure at the focus was identical to the structure carved at the SLM, up to a phase factor of π between the superposed LG modes, which needed to be accounted for with odd values of the radial index^{19,20}. To measure the Gouy phase-induced change in the interference along the optical axis, we placed an SMF at the focus and moved it longitudinally using a stage with a computer controlled piezo actuator. The laser source was a continuous-wave diode laser operating at 810 nm and the SLM used for structuring the light was wavefront corrected using the method described in ref. 41. Furthermore, to get the generated modes as close as possible to the correct transverse structure at the desired beam radius, we employed an additional Gaussian correction in the mode carving that minimized any effect of the initial Gaussian beam structure in the carved mode (see Supplementary Section 5).

For a classical field, we can extract the theoretically expected measurement results simply by calculating the overlap of the Gaussian eigenmode of the SMF and the normalized transverse structure of the scalar field $u_{\text{total}}(\rho, z) = \frac{1}{\sqrt{2}}(u_{0p}(\rho, z) - e^{i\theta}u_{0p'}(\rho, z))$. Thus, for laser light, the amount of laser power coupled into the fibre is proportional to

$$P_L \propto |A_p(z) - e^{-i\theta}A_{p'}(z)|^2, \tag{7}$$

where $A_j(z)$ refer to the overlap between the normalized radial mode j , at a distance z from its focus, and the normalized Gaussian eigenmode of the fibre. To see the Gouy phase dependence of the detection probability, the above equation can then be stated as

$$P_L \propto [|A_p|^2 + |A_{p'}|^2 - 2|A_p||A_{p'}| \cos(\Delta\Phi_G(z) - \theta + \phi(z))],$$

where the term $\phi(z)$ is an extra phase contribution from the curvature of the wavefront acquired upon propagation. However, as the wavefront curvature is very small near the optical axis, the only substantial contribution to the phase of the overlaps $A_j(z)$ comes from the Gouy phase difference $\Delta\Phi_G(z)$. Thus, scanning the fibre through the focus results in a signal that oscillates as $\cos\left(2(p' - p) \arctan\left(\frac{2(z-z_0)}{kw_0^2}\right)\right)$ underneath some envelope function defined by the z -dependence of the overlap functions.

For the measurements, we kept the reference mode (that is, a Gaussian mode with radial index $p = 0$) fixed and varied the index p' of the probe mode between 1 and 4, which lead to four unique measurement scenarios with differing Gouy-phase contributions. The measured data can be found on the top row of Fig. 2. The measurements follow the probability introduced above very well, which we verified by fitting curves that match equation (7) to the data. In each fit, we fixed the mode field diameter of our fibre to the $5 \mu\text{m}$ specified by the manufacturer and only had four fitting parameters: an overall scaling factor of the function, the beam waist w_0 , focal position z_0 and the z -independent phase offset θ . The average adjusted R^2 value of the fits was 0.986, meaning that the data correspond well with the theoretical model.

After first verifying the method's viability using a laser and showing the effect of the Gouy phase on a classical interference pattern along the optical axis, we extended the measurement scheme to observe the quantum Gouy phase. Following the same general idea, we now generated different two-photon NOON states between a reference Gaussian mode ($p = 0$) and higher-order radial modes, and studied the two-photon interference pattern along the optical axis. To prepare such a NOON state, we first generated photon pairs through spontaneous parametric down-conversion (see Supplementary Section 5 for more information) and then shaped each of the two photons individually into a well-defined superposition of the wanted radial modes using two holograms performing two different mode carvings. Once each of the photons was structured, we directed the photons into the same beam path using a beamsplitter. As demonstrated in ref. 6, once in the same beam path, indistinguishable photons bunch into the desired spatial mode NOON state given in equation (1). A simplified sketch of the two-photon experimental set-up can be seen in Fig. 3.

To calculate the N -photon coincidence probability, we project the radial mode NOON state $|\Psi_N(z)\rangle$ onto the state where all of the photons

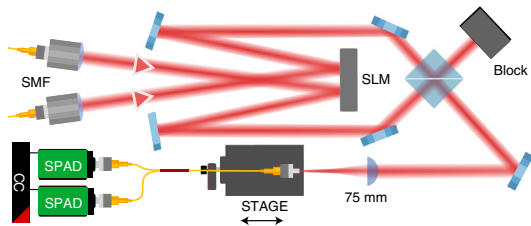


Fig. 3 | Simplified drawing of the experimental set-up. Two photons with Gaussian beam profiles were sent to separate sections of an SLM where they were independently structured into orthogonal superpositions of radial modes. These photons were then probabilistically overlapped using a beamsplitter, after which they bunched into a radial mode NOON state⁶. Finally, this two-photon NOON state was focused down to a 25 μm Gaussian beam waist radius and coupled into a SMF (with a mode field diameter of 5 μm) that was scanned through the focus (from behind the focus towards the lens). The two-photons were then probabilistically split into two single-photon avalanche diodes (SPAD), and we post-selected on both of the detectors detecting a photon at the same time using a coincidence counter (CC). See the main text and Supplementary Section 5 for more details.

have been coupled successfully into the SMF $P = |\langle \Psi(z) | N \rangle_{SMF}|^2$. Assuming that we produce perfectly balanced NOON states of radial modes with a phase offset θ , the N -photon detection probability can be reduced to the form

$$P = \frac{1}{2} |A_p^N(z) - e^{-i\theta} A_{p'}^N(z)|^2. \tag{8}$$

As before, we can express this coincidence probability as

$$P = \frac{1}{2} [|A_p|^{2N} + |A_{p'}|^{2N} - 2|A_p|^N |A_{p'}|^N \cos(\Delta\Phi_0 - \theta + N\phi(z))],$$

which is similar to the detection probability of the classical field, leading to an oscillating interference underneath some envelope function. However, in the above equation we see the photon number-dependent scaling for both the frequency of the oscillation as well as the envelope term. Note that a probability curve with half the amplitude but the same shape can also be observed for photon pairs prepared similarly without bunching. Thus, to verify that we generate radial mode NOON states in our experiment, we prepared the two photons in the corresponding radial mode superpositions and showed that the probability of coupling both of the photons into the SMF roughly doubles when the photons are made indistinguishable in time, which is a clear signature of bunching (see Supplementary Fig. 2 for the measured data). See Supplementary Sections 2 and 3 for detailed derivations of the detection probabilities.

For the NOON state measurements, we used the same set of radial modes in superposition with the reference Gaussian mode leading to the data shown on the bottom row of Fig. 2. As before, the data follow very well the theoretically expected curves, verifying the above-presented equations and their described behaviours. Fits of equation (8) to the data—with the same parameters as in the classical case—resulted in an average adjusted R^2 value of 0.951. The slight imperfections in the data can all be accounted for by imperfections in the alignment, imaging, the SMF eigenmode, spatial mode generation and errors in the stage position. Aside from the errors in the stage positions, all of these can be effectively categorized as contaminations of our state space by modes not included in the theoretical analysis. Hence, our results demonstrate that the quantum Gouy phase leads to a speed up in the accumulated phase upon propagation and also modulates the underlying envelope function. As we will discuss next, both

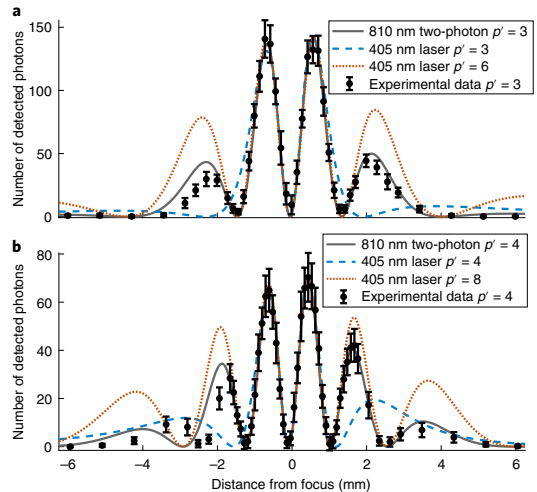


Fig. 4 | Comparing measured two-photon count rates with simulations of classical fields of different wavelength and mode order. **a, b**, The data shown (black dots) and their fits (grey solid lines) correspond to the two-photon NOON state measurements with probe modes $p' = 3$ (**a**) and $p' = 4$ (**b**). The error bars are calculated from 25 repetitions and present the mean value \pm s.d. The dashed and dotted lines show simulated values for a 405 nm laser with two different mode orders and beam waists. For the blue dashed curves, the beam radius of the 405 nm field is matched to the 810 nm mode of the photons at the focusing lens. For the red dotted curves, the Rayleigh length is matched to the 810 nm mode while doubling the radial mode order $p' = \{6, 8\}$. Equation (7) with a scaling factor was used to calculate the curves for the classical 405 nm beam and the SMF mode field diameters were scaled to match the change in mode radius (that is,

$w_{\text{fibre}}^{405} = \frac{w_0^{405}}{w_0^{810}} w_{\text{fibre}}^{810}$). The curves match well near the focus; however, the blue dashed curve does not exhibit the same fringe pattern and the red dotted curve has a larger relative amplitude outside the focal region. Hence, the quantum Gouy phase behaviour cannot be exactly reproduced by simply changing the wavelength and mode order.

features shed new light on the fundamental understanding of the Gouy phase, as well as hint at quantum enhanced metrology applications.

Quantum Fisher information

As the quantum Gouy phase evolves faster with a larger number of photons, one application could be super-sensitive measurements of longitudinal displacement. This prospect can be investigated by calculating the QFI achieved through translation, which is of the form^{31,42–44}

$$F_Q(|\Psi(z)\rangle) = \frac{4}{\hbar^2} \Delta^2 P_z |_{\Psi}. \tag{9}$$

When calculating this variance for the radial mode NOON state $|\Psi(z)\rangle$, we get the QFI

$$F_Q(|\Psi(z)\rangle) = 2N (\Delta^2 k_{z|p} + \Delta^2 k_{z|p'}) + N^2 (\langle k_z \rangle_p - \langle k_z \rangle_{p'})^2, \tag{10}$$

where $\Delta^2 k_{z|i}$ and $\langle k_z \rangle_i$ are the variance and average of k_z for mode i , respectively, calculated using the angular spectrum of the corresponding mode. It is worth noting that the QFI does not depend on z , as the angular spectrum of a mode only acquires a phase structure upon translation. From equation (10), we can see that the second term of the

QFI has Heisenberg scaling. As we show in Supplementary Section 4, this term relates to the Gouy phase difference between modes p and p' . Hence, radial mode NOON states along with their quantum Gouy phase properties should be able to enhance the sensitivity of longitudinal displacement measurements. However, although these states provide benefits such as intrinsic interferometric stability when translating the mode along z , the spatial extent of the modes change, making it challenging to devise a real measurement capable of saturating the QFI at any z . The form of equation (10) also shows that it could be possible to engineer different spatially structured quantum states to measure different physical parameters. Due to the form of the QFI, the key feature that needs to be optimized in such state engineering should be maximizing variance of a specific momentum of the quantum state. For example, this would mean maximizing the variance in orbital angular momentum for rotation sensing⁶ or linear momentum for sensing the longitudinal position (see equation (9)). See Supplementary Section 4 for derivations of the QFI and the Fisher information calculated for the projection used in our experiment.

Momentum uncertainty

In addition to showing the potential for Heisenberg scaling, there is an interesting connection between the QFI and the uncertainty interpretation of the Gouy phase that fundamentally links the potential change in the spread of the transverse momentum to the evolution of the Gouy phase¹². Feng and Winful also noted that a larger momentum spread of higher-order modes results in a bigger Gouy phase shift¹². As the Gouy phase is increased by the photon number N , which is accompanied by a photon number-dependent momentum spread, as can be seen in equation (10), our results make a further connection between the quantum Gouy phase and its uncertainty interpretation. Similarly to ref.¹², one can further link this behaviour to a tighter spatial confinement of the photons which can be made visible, for example by measuring the spatial extent of the N -photon state as shown in Fig. 1c).

The de Broglie wavelength of light

Finally, our results show that the behaviour of a two-photon NOON state cannot be replicated simply by switching to a classical field with half the wavelength. The difference is clear if we note that the Gouy phase has a nonlinear dependence on the wavenumber, which means that simply ascribing an effective de Broglie wavelength λ/N to the N -photon state does not produce the correct quantum Gouy phase. This is in contrast to the phase accrued by a non-converging field upon propagation as well as arguments discussed in such a context^{32–34}. To investigate this fundamental difference in more detail, in Fig. 4 we plotted the measured data for two radial mode NOON states, along with overlap curves calculated for classical 405 nm modes with two different mode orders and waists. From these comparisons we see that the effect is not reproduced by a simple switching of the wavelength or doubling of the mode order.

Based on the comparison in Fig. 4 and equation (6) the only exact description of the N -photon Fock state evolution seems to be that it evolves as the underlying mode, taken to the power of N . Although doubling the mode order and halving the wavelength seems to replicate quite well the shown two-photon behaviour. As the state evolves as the mode taken to power N , this evolution of the N -photon quantum state results in a more rapid phase change and tighter confinement of the N -photon. Both of these features have been taken advantage of in different studies and experiments. Either in the form of NOON-state super-resolution measurements^{30,45} or in increasing the confinement⁴⁶.

Conclusion

In summary, we have verified theoretically and experimentally that the increased phase sensitivity of multi-photon quantum states also extends to the fundamental phase anomaly of converging waves called the Gouy phase. We have shown through single-path interferometric

measurements along the optical axis that two-photon NOON states experience twice the Gouy phase when travelling through a focus. As the Gouy phase is a fundamental feature of converging waves, our results should apply broadly to quantum states of any bosonic system. Moreover, as the Gouy phase is an important factor in systems such as optical cavities^{46,47}, and a powerful tool in various applications such as mode sorters and mode converters^{19–21}, our results can be widely utilized in applications in quantum optics and quantum information science. In addition to providing a tool for quantum state manipulation, we showed that our results allow Heisenberg-limited scaling in measurements of the longitudinal displacement and, as such, might inspire new superresolution measurement schemes.

Aside from these possible technological applications, we have linked the speed-up of the Gouy phase in the quantum domain to an increased spread in the momentum of an N -photon state. Hence, our results show that the uncertainty interpretation of the phase anomaly¹² holds true in the quantum domain. Finally, due to the nonlinear relation between the Gouy phase and the wavenumber, our results unambiguously demonstrate that an N -photon state cannot be rigorously modelled by using a classical field with a wavelength λ/N . However, our results suggest that an additional N -fold increase in the mode order can approximate the effect of the quantum Gouy phase when the beam Rayleigh lengths are matched. This hints at a possible link between an N -photon state and the N th harmonic of a classical field, which introduces an increase of the mode order and decrease of the beam waist, in addition to doubling the frequency. Thus, our study not only outlines possible applications using the quantum features of spatially structured photons, it also sheds new light on the fundamental understanding of the Gouy phase, a property intrinsic to all systems described by converging or diverging waves.

Online content

Any methods, additional references, Nature Research reporting summaries, source data, extended data, supplementary information, acknowledgements, peer review information; details of author contributions and competing interests; and statements of data and code availability are available at <https://doi.org/10.1038/s41566-022-01077-w>.

References

1. Sit, A. et al. High-dimensional intracity quantum cryptography with structured photons. *Optica* **4**, 1006–1010 (2017).
2. Cozzolino, D. et al. Orbital angular momentum states enabling fiber-based high-dimensional quantum communication. *Phys. Rev. Appl.* **11**, 064058 (2019).
3. Babazadeh, A. et al. High-dimensional single-photon quantum gates: concepts and experiments. *Phys. Rev. Lett.* **119**, 180510 (2017).
4. Erhard, M., Fickler, R., Krenn, M. & Zeilinger, A. Twisted photons: new quantum perspectives in high dimensions. *Light Sci. Appl.* **7**, 17146–17146 (2018).
5. Cardano, F. et al. Detection of Zak phases and topological invariants in a chiral quantum walk of twisted photons. *Nat. Commun.* **8**, 1–7 (2017).
6. Hiekkamäki, M., Bouchard, F. & Fickler, R. Photonic angular superresolution using twisted NOON states. *Phys. Rev. Lett.* **127**, 263601 (2021).
7. Gouy, L.G. *Sur Une Propriété Nouvelle des Ondes Lumineuses* (Gauthier-Villars, 1890).
8. Gouy, L. G. Sur la propagation anormale des ondes. *Compt. Rendue Acad. Sci. Paris* **111**, 33 (1890).
9. Baladron-Zorita, O., Wang, Z., Hellmann, C. & Wyrowski, F. Isolating the Gouy phase shift in a full physical-optics solution to the propagation problem. *JOSA A* **36**, 1551–1558 (2019).
10. Linfoot, E. H. & Wolf, E. Phase distribution near focus in an aberration-free diffraction image. *Proc. Phys. Soc. B* **69**, 823 (1956).

11. Boyd, R. W. Intuitive explanation of the phase anomaly of focused light beams. *JOSA* **70**, 877–880 (1980).
12. Feng, S. & Winful, H. G. Physical origin of the Gouy phase shift. *Optics Lett.* **26**, 485–487 (2001).
13. Hariharan, P. & Robinson, P. The Gouy phase shift as a geometrical quantum effect. *J. Modern Optics* **43**, 219–221 (1996).
14. Visser, T. D. & Wolf, E. The origin of the Gouy phase anomaly and its generalization to astigmatic wavefields. *Optics Commun.* **283**, 3371–3375 (2010).
15. Simon, R. & Mukunda, N. Bargmann invariant and the geometry of the Goy effect. *Phys. Rev. Lett.* **70**, 880 (1993).
16. Lee, T., Cheong, Y., Baac, H. W. & Guo, L. J. Origin of Gouy phase shift identified by laser-generated focused ultrasound. *ACS Photon.* **7**, 3236–3245 (2020).
17. Subbarao, D. Topological phase in Gaussian beam optics. *Optics Lett.* **20**, 2162–2164 (1995).
18. Yang, J. & Winful, H. G. Generalized eikonal treatment of the Gouy phase shift. *Optics Lett.* **31**, 104–106 (2006).
19. Zhou, Y. et al. Sorting photons by radial quantum number. *Phys. Rev. Lett.* **119**, 263602 (2017).
20. Gu, X., Krenn, M., Erhard, M. & Zeilinger, A. Gouy phase radial mode sorter for light: concepts and experiments. *Phys. Rev. Lett.* **120**, 103601 (2018).
21. Beijersbergen, M. W., Allen, L., Van der Veen, H. E. L. O. & Woerdman, J. Astigmatic laser mode converters and transfer of orbital angular momentum. *Optics Commun.* **96**, 123–132 (1993).
22. Whiting, A. I., Abouraddy, A. F., Saleh, B. E. A., Teich, M. C. & Fourkas, J. T. Polarization-assisted transverse and axial optical superresolution. *Optics Express* **11**, 1714–1723 (2003).
23. Da Paz, I. G., Nemes, M. C., Pdua, S., Monken, C. H. & Peixoto de Faria, J. G. Indirect evidence for the Gouy phase for matter waves. *Phys. Lett. A* **374**, 1660–1662 (2010).
24. Da Paz, I. G., Saldanha, P. L., Nemes, M. C. & Peixoto De Faria, J. G. Experimental proposal for measuring the Gouy phase of matter waves. *New J. Phys.* **13**, 125005 (2011).
25. Petersen, T. C. et al. Measurement of the Gouy phase anomaly for electron waves. *Phys. Rev. A* **88**, 043803 (2013).
26. Ducharme, R. & da Paz, I. G. Gouy phase for relativistic quantum particles. *Phys. Rev. A* **92**, 023853 (2015).
27. Guzzinati, G., Schattschneider, P., Bliokh, K. Y., Nori, F. & Verbeeck, J. Observation of the Larmor and Gouy rotations with electron vortex beams. *Phys. Rev. Lett.* **110**, 093601 (2013).
28. Kawase, D., Miyamoto, Y., Takeda, M., Sasaki, K. & Takeuchi, S. Observing quantum correlation of photons in Laguerre–Gauss modes using the Gouy phase. *Phys. Rev. Lett.* **101**, 050501 (2008).
29. de Brito, F. C. V., da Paz, I. G., Hiller, B., Araujo, J. B. & Sampaio, M. Gouy phase of type-I SPDC-generated biphotons. *Phys. Lett. A* **386**, 126989 (2021).
30. Dowling, J. P. Quantum optical metrology—the lowdown on high-NOON states. *Contemporary Phys.* **49**, 125–143 (2008).
31. Giovannetti, V., Lloyd, S. & Maccone, L. Advances in quantum metrology. *Nat. Photon.* **5**, 222–229 (2011).
32. Jacobson, J., Bjrk, G., Chuang, I. & Yamamoto, Y. Photonic de Broglie waves. *Phys. Rev. Lett.* **74**, 4835 (1995).
33. Edamatsu, K., Shimizu, R. & Itoh, T. Measurement of the photonic de Broglie wavelength of entangled photon pairs generated by spontaneous parametric down-conversion. *Phys. Rev. Lett.* **89**, 213601 (2002).
34. Walther, P. et al. De Broglie wavelength of a non-local four-photon state. *Nature* **429**, 158–161 (2004).
35. Andrews, D. L. & Babiker, M. *The Angular Momentum of Light* (Cambridge University Press, 2012).
36. Pinheiro da Silva, B., Pinillos, V. A., Tasca, D. S., Oxman, L. E. & Khoury, A. Z. Pattern revivals from fractional Gouy phases in structured light. *Phys. Rev. Lett.* **124**, 033902 (2020).
37. Torres, J. P., Deyanova, Y., Torner, L. & Molina-Terriza, G. Preparation of engineered two-photon entangled states for multidimensional quantum information. *Phys. Rev. A* **67**, 052313 (2003).
38. Wnsche, A. Quantization of Gauss–Hermite and Gauss–Laguerre beams in free space. *J. Optics B* **6**, 47 (2004).
39. Saleh, B. E. A. & Teich, M. C. *Fundamentals of Photonics* Ch. 4.1–4.2 (John Wiley & Sons, 1991).
40. Bolduc, E., Bent, N., Santamato, E., Karimi, E. & Boyd, R. W. Exact solution to simultaneous intensity and phase encryption with a single phase-only hologram. *Optics Lett.* **38**, 3546–3549 (2013).
41. Jesacher, A. et al. Wavefront correction of spatial light modulators using an optical vortex image. *Optics Express* **15**, 5801–5808 (2007).
42. Demkowicz-Dobrzański, R., Jarzyna, M. & Kotodyński, J. Quantum limits in optical interferometry. *Prog. Optics* **60**, 345–435 (2015).
43. Barbieri, M. Optical quantum metrology. *PRX Quantum* **3**, 010202 (2022).
44. Polino, E., Valeri, M., Spagnolo, N. & Sciarrino, F. Photonic quantum metrology. *AVS Quantum Sci.* **2**, 024703 (2020).
45. Slussarenko, S. et al. Unconditional violation of the shot-noise limit in photonic quantum metrology. *Nat. Photon.* **11**, 700–703 (2017).
46. Wildfeuer, C. F. Resolution and sensitivity of a Fabry–Perot interferometer with a photon-number-resolving detector. *Phys. Rev. A* **80**, 043822 (2009).
47. Ackemann, T., Grosse-Nobis, W. & Lippi, G. L. The Gouy phase shift, the average phase lag of Fourier components of Hermite–Gaussian modes and their application to resonance conditions in optical cavities. *Optics Commun.* **189**, 5–14 (2001).

Publisher’s note Springer Nature remains neutral with regard to jurisdictional claims in published maps and institutional affiliations.

Open Access This article is licensed under a Creative Commons Attribution 4.0 International License, which permits use, sharing, adaptation, distribution and reproduction in any medium or format, as long as you give appropriate credit to the original author(s) and the source, provide a link to the Creative Commons license, and indicate if changes were made. The images or other third party material in this article are included in the article’s Creative Commons license, unless indicated otherwise in a credit line to the material. If material is not included in the article’s Creative Commons license and your intended use is not permitted by statutory regulation or exceeds the permitted use, you will need to obtain permission directly from the copyright holder. To view a copy of this license, visit <http://creativecommons.org/licenses/by/4.0/>.

© The Author(s) 2022

Methods

Source

The photon pair source uses a 12-mm-long, type-0 periodically poled potassium titanyl phosphate nonlinear crystal that is pumped by a 133.5 mW continuous-wave 405 nm free-space laser. The down-converted photons are filtered through a 3-nm-wide bandpass filter centred around 810 nm, and coupled into separate single-mode fibres. Before the single-mode fibres, one photon is sent through an adjustable delay line. The rate of photon pairs after the single-mode fibres is roughly 3 MHz (correcting for accidentals, efficiency and nonlinearity of detectors).

Spatial mode manipulation

The spatial structures of the photons were modulated with a Holoeye Pluto-2 SLM. To independently shape each photon, a pair of amplitude and phase modulating holograms were displayed on the phase-only SLM. The amplitude modulation was implemented using a method that spatially changes the efficiency of the holograms grating. The NOON states were created by structuring the photons in equal and orthogonal superpositions of the two modes in the NOON state. A detailed figure of the experimental system is shown in the Supplementary Fig. 2 and more experimental details are given in Supplementary Section 5. The Gaussian beam waist of the photon spatial modes was roughly 774 μm before they were focused down to the final SMF (Thorlabs 780HP FC/PC).

Detection

The single-mode fibre to which the final state of light was projected on was scanned around the focus using a translation stage with a computer controlled piezo actuator (Thorlabs PIA13). A coupling stage (xyz-control) and a mount with tip/tilt controls was placed on top of the translation stage to allow maximum control of the alignment of the fibre. As the manufacturer of the piezo actuator stated that the step size of the actuator might differ depending on the direction, the actuator was scanned in the same direction in all measurements. The typical step size provided by the manufacturer (20 nm per piezo step) was used in the data processing. To detect the photon pair, a fibre beamsplitter was used to probabilistically split the photons. Subsequently, two single-photon avalanche photodiodes (Laser Components Count-T) were used in combination with a coincidence counter (IDQ ID900) to post-select for two-photon detections occurring between the two detectors. The coincidence window used to determine coinciding detections was $\tau = 1$ ns and the accidental coincident detections were calculated using the approximate formula $R_1 R_2 \tau$, where R_i refer to single photon detection rates in the two detectors. For measuring the coupling efficiency of laser light, two power meters were used. The first one was placed in one output of a fibre beamsplitter, which split the light coming out of the laser into two outputs. The power recorded with

this power meter was used to monitor the output power of the laser as a reference signal. The second output of the fibre beamsplitter was fed to the spatial mode manipulation set-up. To record the classical signal, the second power meter was placed directly after the final SMF. The final data is calculated as the power in the second power meter divided by the power in the first one to eliminate the effects of possible laser power fluctuations from the data.

Data availability

Source Data are provided with this paper.

Acknowledgements

We thank F. Bouchard and S. Prabhakar for fruitful discussions. We acknowledge the support of the Academy of Finland through the Competitive Funding to Strengthen University Research Profiles (decision no. 301820; grant no. 308596), and the Photonics Research and Innovation Flagship (PREIN—decision no. 320165). M.H. acknowledges support from the Doctoral School of Tampere University and the Magnus Ehrnrooth foundation through its graduate student scholarship. R.F. acknowledges support from the Academy of Finland through the Academy Research Fellowship (decision no. 332399).

Author contributions

M.H. and R.F. conceived and designed the experiment. M.H. constructed and performed the experiment, and processed the data. R.F.B. and R.F. supervised and assisted at every stage of the study. M.H., R.F.B. and M.O. derived the theoretical framework. M.H., R.F.B. and R.F. wrote the manuscript. All of the authors edited and proofed the manuscript.

Competing interests

The authors declare no competing interests.

Additional information

Supplementary information The online version contains supplementary material available at <https://doi.org/10.1038/s41566-022-01077-w>.

Correspondence and requests for materials should be addressed to Markus Hiekkamäki.

Peer review information *Nature Photonics* thanks Xuemei Gu and the other, anonymous, reviewer(s) for their contribution to the peer review of this work.

Reprints and permissions information is available at www.nature.com/reprints.

